Structure and Ionisation in Dense Plasmas: A Molecular Dynamics Approach

Daniel Plummer

Exeter College

University of Oxford

Work submitted for the degree of

Doctor of Philosophy in Atomic and Laser Physics

Hilary, 2026

Abstract

This thesis investigates the structural and thermodynamic behaviour of partially-ionised dense plasma using advanced molecular dynamics frameworks formulated within a chemical picture. Emphasis is placed on the explicit treatment of bound electronic states and the self-consistent determination of ionisation equilibria in strongly interacting systems relevant to warm dense matter. First, a general methodology is developed to compute model-dependent ionisation states through free energy minimisation and thermodynamic integration. To demonstrate the approach, two representative models for hydrogen plasma are constructed in which electrons are either bound in the hydrogen ground state or represented as a uniform charge-neutralising background. These models are used to study the transition from atomic gas to ionised plasma, highlighting the role of neutral interactions beyond commonly employed chemical models. Concepts such as ionisation potential depression and pressure ionisation are also examined. Subsequently, a wavepacket molecular dynamics formalism is developed to model the structural properties of dense plasmas with a modified wavefunction that directly incorporates bound states. Using hydrogen as a prototypical system, self-consistent charge state distributions and radial distribution functions are calculated, and shown to depend on the confining potential, an empirical parameter in the model. These results are compared directly with path integral Monte Carlo data, enabling a critical assessment of the underlying approximations. Finally, a statistical theory for the dynamical degrees of freedom in wavepacket molecular dynamics is derived. Statistical distributions for the variables that parameterise the Gaussian wavepacket widths are obtained for both isotropic and anisotropic formulations. These are shown to agree with simulation data under warm dense matter conditions. The results provide a practical means of assessing the effect of the confining potential. Together, the developments presented in this thesis provide, and critically assess, a set of computational tools for investigating partially-ionised dense plasma.

Acknowledgments

First of all, I would like to thank my supervisor, Gianluca Gregori, for his support and guidance throughout my DPhil. I am also grateful to Sam Vinko, Pontus Svensson, and Patrick Hollebon for their supervision and advice during my time at Oxford.

In the Simon Room, I was fortunate to share many conversations that were both intellectually stimulating and personally supportive. While I cannot name everyone individually, I am particularly grateful to Pontus Svensson and Charles Heaton. Thank you both.

I am deeply thankful to my parents, Andrew and Amanda Plummer, for their constant love and encouragement, and for providing welcome distractions through visits and trips over the years. Finally, and most importantly, I am forever grateful to my wife, Caroline Vitzthum.

Daniel Plummer, Oxford, February 2026

Table of Contents

List of Figures

List of Tables

List of Symbols

k_B	Boltzmann's constant
ε_0	Vacuum permittivity
m_e	Electron mass
e	Elementary charge
a_0	Bohr radius
$\hbar$	Reduced Planck's constant
E_F	Fermi energy
θ	Degeneracy parameter
Γ	Coulomb coupling parameter
d_a	Wigner-Seitz radius
r_s	Density parameter (Wigner-Seitz radius in units of Bohr radius)
E_B^H	Hydrogen binding energy (approximately the Rydberg energy)
$\mathcal{H}$	Hamiltonian function
$\mathcal{L}$	Lagrangian function
Z	Partition function
F	Free energy
μ	Chemical potential
Λ	Thermal de Broglie wavelength
$\hat{H}_e$	Electronic Hamiltonian operator
λ	Thermodynamic integration coupling parameter
α	Ewald parameter
ξ	Madelung constant
u_{ij}	Pair potential between particles i and j
$\bar{z}$	Ionisation state
ΔI	Ionisation potential depression
M_p	Proton mass
$\lvert\Psi_e\rangle$	Many-body electron wavefunction
$\lvert Q\rangle$	Restricted many-body wavefunction
Σ	Shape (covariance) matrix
Π	Shape-momentum matrix
$\boldsymbol{\xi}$	Deviation from expected position vector
$\hat{K}_e$	Electronic kinetic energy operator
A	Confinement strength
σ_0	Confinement parameter
g_{ab}	Species-resolved radial distribution function
ℓ	Extent of anisotropic wavepacket (eigenvalue of Σ)
a	Extent of isotropic wavepacket
σ_i	Width variable of anisotropic wavepacket
$\bar{\sigma}$	Root-mean-squared anisotropic width
σ	Width variable of isotropic wavepacket

Chapter 1

Introduction

Plasma, often described as the fourth naturally occurring state of matter, is thought to constitute approximately 99% of the baryonic matter in the observable universe. The plasma state consists of free charges interacting through electromagnetic forces, and the principles of plasma physics therefore apply to a diverse range of systems. For example, although the concept originates from ionised low-density gases [1], it is also used to describe the behaviour of electrons in metals, where they delocalise to form a quantum plasma while the ions remain arranged in a solid lattice. A particularly challenging plasma-like regime to understand occurs when matter exhibits solid-state densities and elevated temperatures ($T \gtrsim 10^4\,\mathrm{K}$), manifesting at the junction between condensed matter physics, plasma physics and dense liquids. This regime is known as *warm dense matter* (WDM).

Recently, the understanding of WDM has seen significant progress [2], partly because of its importance in inertial confinement fusion (ICF) [3, 4], a promising future technology for energy production. In fact, throughout much of the compression phase in ICF experiments, the central hotspot experiences thermodynamic conditions characteristic of WDM, making a quantitative understanding of this regime essential for efficient energy production [5]. For example, accurate knowledge of the equation of state, which relates pressure, temperature and density, is important for the hydrodynamic modelling of fusion experiments [6, 7]. Many additional quantities are required to ensure high-fidelity predictions, including electronic and ionic transport coefficients, and stopping power [8, 9]. The properties of WDM are also critical for the understanding of a variety of compact astrophysical objects. Gas giants such as Jupiter and Saturn consist primarily of hydrogen–helium mixtures in a high-pressure WDM state [10, 11], with interior structure models relying heavily on theoretical predictions and experimental benchmarks. Furthermore, realisations of warm dense states may be found in brown and white dwarf stars [12], the outer crust of neutron stars [11, 13], the interior of the Earth, at the centre of the Sun, and in numerous exoplanet types [2, 14].

In this thesis, several models are extended to capture the behaviour of partially-ionised matter in the warm dense regime. These models are explored through molecular dynamics (MD), a general simulation framework where individual particle motion is resolved. Performing these simulations enables the investigation of ionisation effects, which are generally important for spectroscopic and hydrodynamic modelling of plasmas [15–17], as well as the structural properties of the models.

1.1 Characterisation of warm dense matter

The properties of WDM are dependent on a complex interplay of factors, including an array of different quantum effects, inter-particle Coulomb correlations, and the possibility of chemical bond formation. To rationalise these competing factors, dimensionless parameters are typically introduced [2, 18–21], the most relevant of which are introduced in this section.

To quantify the prevalence of quantum mechanical effects, the thermal energy is compared with the Fermi energy E_F. This results in the *degeneracy parameter*,

$$\theta = \frac{k_B T}{E_F}, \tag{1.1.1}$$

where the Fermi energy depends on the electron number density n_e and electron mass m_e:

$$E_F = \frac{\hbar^2}{2m_e}(3\pi^2 n_e)^{2/3}. \tag{1.1.2}$$

Under degenerate conditions ($\theta < 1$) the population of electronic energy states follows the underlying Fermi–Dirac statistics and the Fermi energy becomes the relevant energy scale. At high temperatures, the electrons are nondegenerate ($\theta \gg 1$) and follow Maxwell–Boltzmann statistics. In WDM the electrons are between these two limits and are typically described as *partially degenerate* ($\theta \sim 1$). Therefore, both quantum-statistical effects and thermal effects are important, complicating both analytical treatments and numerical modelling.

WDM is an example of a non-ideal plasma, in which inter-particle interactions alter the

system's properties to the extent that ideal-gas approximations are no longer valid. The prominence of interactions in a given particle species a and b may be estimated with the *coupling parameter* [2],

$$\Gamma_{ab} = \frac{|\langle V_{ab}\rangle|}{\langle K_a\rangle}, \tag{1.1.3}$$

which compares the mean potential energy per particle $\langle V_{ab}\rangle$ and the mean kinetic energy per particle $\langle K_a\rangle$. For a weakly coupled plasma ($\Gamma \ll 1$), the properties are determined by thermal and collective motion. In a non-ideal plasma, the coupling parameter is greater than or of order unity ($\Gamma \gtrsim 1$), such that liquid-like short-range order is present and therefore interactions can neither be neglected nor treated perturbatively. Meanwhile, at high coupling ($\Gamma \gg 1$), matter will crystallise into a lattice [22], and hence form a solid phase. In the case of charged Coulomb systems, the following estimate for their interaction energy is typically used,

$$\langle V_{aa}\rangle = \frac{Z_a^2 e^2}{4\pi\varepsilon_0 d_a}, \tag{1.1.4}$$

where Z_a is the charge state of the ion species and d_a is the average inter-particle separation and is conventionally taken to be the *Wigner–Seitz radius*

$$d_a = \left(\frac{3}{4\pi n_a}\right)^{1/3}, \tag{1.1.5}$$

which is defined in terms of the particle number density n_a. Using the kinetic energy of point particles, $\frac{3}{2}k_B T$, yields the classical coupling parameter[1],

$$\Gamma_{aa} = \frac{Z_a^2 e^2}{4\pi\varepsilon_0 d_a}\frac{1}{k_B T}. \tag{1.1.6}$$

Electrons are partially degenerate in WDM, and therefore their kinetic energy deviates from classical results due to quantum statistical effects. To estimate their kinetic energy, an ideal Fermi gas in thermal equilibrium is usually considered. For the case of spin-$\frac{1}{2}$ particles, the

1. The 3/2 factor is typically not included, given that only an order of magnitude estimate is required.

kinetic energy per particle is [23]

$$\langle K_e \rangle = \frac{3}{2} k_B T \frac{\mathcal{F}_{5/2}(z)}{\mathcal{F}_{3/2}(z)}, \tag{1.1.7}$$

where $z = \exp(\beta\mu_e)$ and μ_e is the chemical potential of the electrons, set by the electron density n_e [23]. Here $\mathcal{F}_\nu(z)$ is the Fermi–Dirac function of order ν:

$$\mathcal{F}_\nu(z) = \frac{1}{\Gamma(\nu)} \int_0^\infty \frac{x^{\nu-1}}{z^{-1}\exp(x) + 1} x. \tag{1.1.8}$$

The electron–electron coupling parameter may now be defined as

$$\Gamma_{ee} = \frac{e^2}{4\pi\varepsilon_0 d_e} \frac{1}{k_B T} \frac{\mathcal{F}_{3/2}(z)}{\mathcal{F}_{5/2}(z)}. \tag{1.1.9}$$

An alternative method to characterise the electron coupling is through the following density parameter, which is simply the electron Wigner–Seitz radius divided by the Bohr radius:

$$r_s = \frac{d_e}{a_0}. \tag{1.1.10}$$

In the following chapters, this parameter will be referred to as the density parameter or Wigner-Seitz radius, although it is sometimes referred to as the Brückner parameter. This parameter determines the electron coupling at low temperatures. Specifically, for small r_s, quantum statistical effects are dominant and the electrons behave as an ideal Fermi gas, while for large r_s, Coulomb interactions determine the properties of the system in the ground state ($T = 0$) limit [20].

In WDM, the particles are moderately to strongly coupled, i.e. $\Gamma_{aa} \gtrsim 1$ for the ions. Similarly, $r_s \sim 1$ and $\Gamma_{ee} \sim 1$ for the electrons. Figure 1.1 schematically illustrates the WDM parameter space in terms of temperature and total electron density. The region corresponds to the intersection of the isocurves where the coupling, degeneracy, and density parameters are all unity, shown here for hydrogen as a representative example. The electron–electron

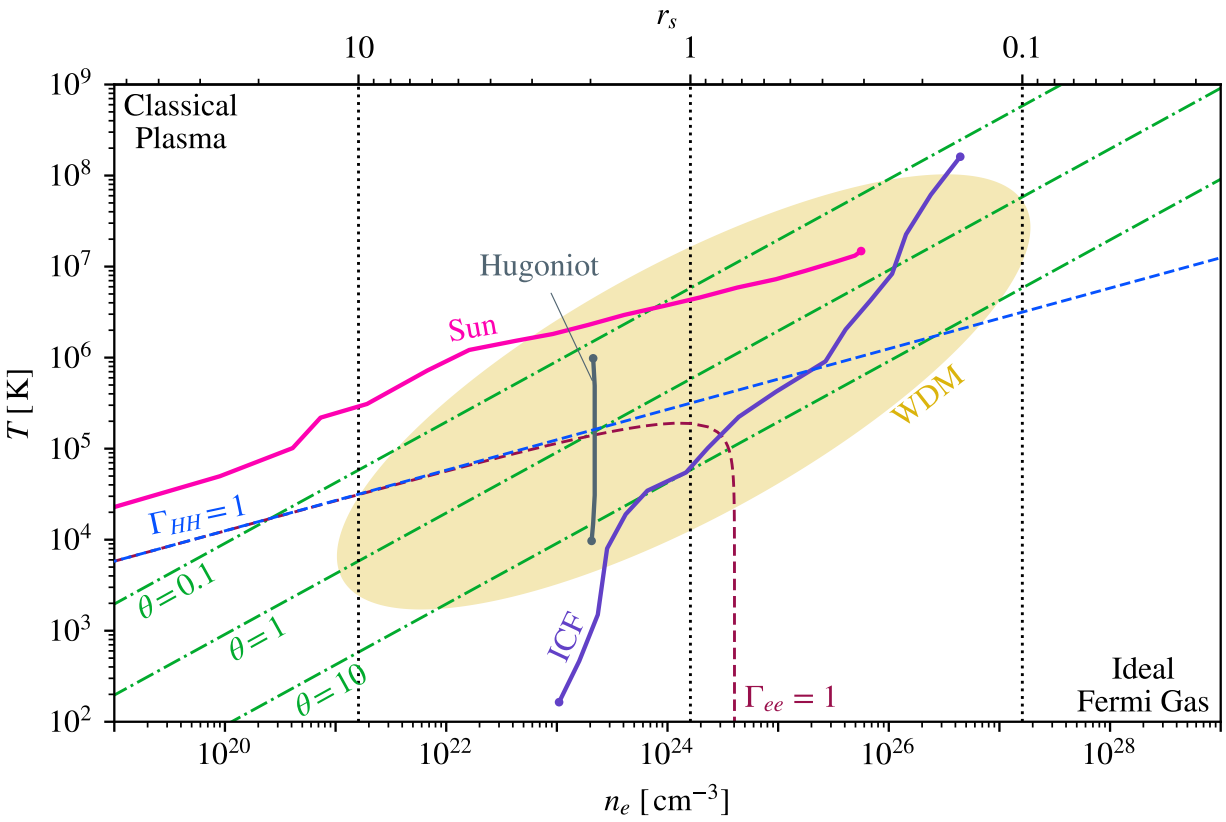

Figure 1.1: A schematic depiction of the warm dense matter regime, given by the central orange region, within the broader density-temperature plane and relevant dimensionless parameters. The horizontal axis takes values of electron density n_e. Isocurves are plotted for the classical coupling parameter of hydrogen Γ_{HH}, quantum coupling parameter of the electrons Γ_{ee}, electronic degeneracy parameter θ and electronic density parameter r_s. Three physical examples of WDM are also plotted: (1) A representative ICF central hotspot trajectory given by the purple curve [9]. (2) The expected thermodynamic conditions of the Sun at different radial coordinates, given by the solid pink curve, from WDM figure in Ref. [24]. (3) A section of the hydrogen Hugoniot, given by the solid grey curve [25].

coupling parameter shows a nonlinear dependence at high densities due to Pauli blocking, which increases the kinetic energy relative to the classical prediction and thus reduces the effective coupling strength. While it is also possible to define electron–ion coupling parameters, the strength of interactions between electrons and ions is closely related to the ionisation of the plasma. Under sufficiently strong electron–ion coupling, electrons and ions form bound states, a topic examined in more detail for hydrogen plasma in the following section.

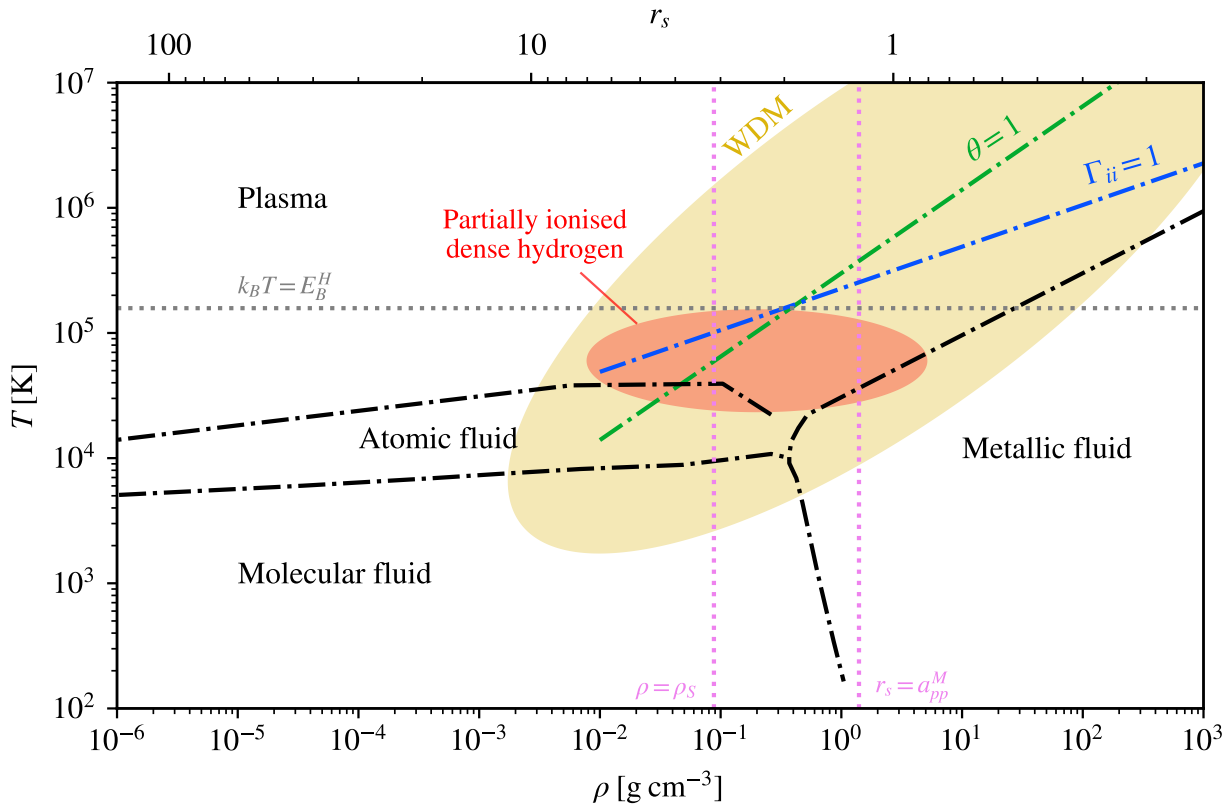

Figure 1.2: High-temperature phase diagram of hydrogen. Approximate phase boundary lines are taken from Ref. [26]. Molecular, atomic, plasma and metallic phases are distinguished, all of which exhibit fluid-like properties. In this thesis, the properties of partially-ionised dense hydrogen plasma, a region loosely marked in red, are studied through molecular dynamics simulations. In the figure ρ_s is the solid density of hydrogen (at ambient pressure).

1.2 Partially-ionised dense hydrogen

The methods developed in this thesis are, in principle, applicable to a wide range of elements and mixtures; however, hydrogen is chosen as a test case to benchmark the models under warm dense, partially-ionised conditions. Beyond serving as a benchmark, hydrogen in this regime is central to numerous applications and open questions in high-energy-density physics [21]. The high-temperature phase diagram of hydrogen is examined in the context of the WDM regime in Figure 1.2. At low densities ($\rho \lesssim 0.1\,\mathrm{g/cm^3}$) and low temperatures ($10^2\,\mathrm{K} \lesssim T \lesssim 5\times10^4\,\mathrm{K}$) hydrogen manifests as a molecular fluid, which includes the molecular gas encountered at ambient conditions.

As the temperature of the molecular fluid is increased, it will start to dissociate into an

atomic fluid at approximately $T \sim 4 \times 10^4\,\mathrm{K}$. At the same time, electrons bound in molecular and atomic orbitals may gain enough kinetic energy to escape their local ionic potential and become ionised. As the temperature is further increased, the majority of the electrons become unbound and the plasma state is reached. The relevant energy scale is the binding energy of a hydrogen atom,

$$E_B^H \approx 13.6\,\mathrm{eV}, \tag{1.2.1}$$

which is approximately equivalent to the Rydberg energy[2], with a characteristic temperature shown in Figure 1.2. This threshold provides an estimate of when the plasma becomes fully ionised, given that statistical effects encourage ionisation processes at considerably lower temperatures. The effect of ionisation processes occurring at temperatures lower than this threshold will be further discussed in the context of *the chemical picture* in Chapter 3.

Compressing hydrogen in its molecular fluid phase will eventually lead to the infamous insulator-to-metal transition, which is possibly a first-order phase transition and remains under intense study [21]. The resulting phase is a metallic fluid, similar to conventional liquid metals, where the electrons are highly degenerate and the ions are strongly coupled. At higher temperatures a similar effect occurs at the boundary between the metallic fluid and the partially-ionised plasma phase. This is known as *pressure ionisation*, and is characterised by a rapid but continuous transition in the number of ionised electrons as density is increased. The ability of molecular dynamics models with effective atomic potentials to capture this transition is studied in Chapter 3. Generally, the region of study in this thesis is marked in red. This is a subset of the WDM parameter space where partial ionisation is present and both pressure ionisation and temperature ionisation effects are relevant. Extending models for fully ionised plasmas into this regime is of general importance for experimental realisations of many different warm dense materials, given that ions with higher charge states will have bound electrons over a broad range of conditions.

2. The difference is because the Rydberg energy is defined as the binding energy of an electron–proton system under the approximation that the mass ratio is negligible, i.e. the proton has infinite mass.

1.3 Multiscale modelling

The modelling of high-energy-density fluids requires a multiscale approach. To predict the evolution of matter over large time and length scales, *hydrodynamic* modelling may be used to provide predictions for laser-driven compression experiments, such as ICF experiments [7]. Under these extreme conditions, radiative transport effects are also present and must therefore be included within the hydrodynamic framework for a sufficiently accurate description. Radiation-hydrodynamics codes such as FLASH [27] and Hydra [28] are therefore used extensively in experimental design and diagnosis. However, these modelling techniques require lower-level input of the properties of matter. For example, the equation of state, which relates pressure, density and temperature, is required [6, 29]. Additionally, information on how a material (or mixture) responds to gradients in thermodynamic variables is essential for an accurate simulation [8]. This information is encoded, for systems close to equilibrium, within the transport coefficients of a material [30]. Furthermore, given that experiments often produce transient nonequilibrium conditions, quantities such as energy exchange rates [31, 32] and charge state distributions [17] are often required for spectral and nonequilibrium modelling. In principle, it is possible to compute these properties using lower-level theory and simulation. For example, in classical ($\theta \gg 1$) systems that are sufficiently weakly coupled ($\Gamma \ll 1$), *kinetic* approximations may be used to derive closed-form expressions for transport coefficients such as thermal conductivity and viscosity. Additionally, kinetic simulations may be used to study transport behaviour in various scenarios, for example Ref. [33]. However, for strongly coupled systems—where perturbative expansions based on weak coupling approximations are invalid—direct simulation at the particle level is typically required for a robust description. These simulations are collectively referred to as *atomistic* simulation techniques. A diverse range of atomistic simulation techniques exist, distinguished primarily by how they incorporate quantum mechanics and by the sampling methods they use to generate statistically representative configurations of the system. Quantum mechanics introduces substantial complexity into first-principles atomistic modelling, and therefore a diverse range

of approaches have been developed, each based on different types of approximation for the electron subsystem. In this thesis, the atomistic simulation framework of molecular dynamics (MD), which evolves a set of classical particles (atoms or ions) in time, is employed. More specifically, two models suitable for MD simulation of partially-ionised plasma are developed. The MD methodology is contextualised in the following section within a brief overview of different atomistic simulation techniques applicable to WDM.

1.4 Atomistic simulation

The goal of atomistic simulation is to extract physical properties of the target system. For WDM applications, there are two prominent approaches for performing these calculations. The first method, known generally as a Monte Carlo method, is to sample representative configurations of the system from a distribution known from statistical mechanics. The most prominent example of this technique in the field of WDM is the path integral Monte Carlo (PIMC) method [26], which performs a numerical sampling of a system's finite-temperature partition function. This method has been applied extensively to the homogeneous electron gas [20] and warm dense hydrogen [21, 26]. Approximate formulations have also been used to compute the high-temperature equation of state for many warm dense materials [6].

In the second method, of which MD is a prominent example, one performs a time-resolved simulation based on a chosen set of dynamical evolution equations. Access to the time-resolved state of the system allows a diverse set of properties to be directly calculated that are not immediately available from statistical Monte Carlo methods. Perhaps most importantly, it grants access to *time correlation functions*, which track the correlations between observables at different times. Time correlation functions may be used to compute both the transport properties and the dynamic structure factor [34] of a material, the latter of which may be directly related to how X-rays inelastically scatter from a sample of WDM [35, 36]. Therefore, as both input for hydrodynamic modelling and for experimental diagnosis, a variety of time-resolved atomistic models have been developed [21]. These models may be categorised based

on (1) their treatment of the partially degenerate electrons present in WDM, and (2) whether they employ the Born–Oppenheimer approximation. For example, many methods are based on a density functional theory (DFT) treatment of the electrons, which involves a variational calculation with an approximation for the exchange-correlation energy [37], while the ions are treated classically within an MD framework. In the standard DFT-MD approach, electrons are assumed to adiabatically adjust to the ionic motion in time [37], and therefore, for WDM, a finite-temperature DFT calculation is performed at each timestep in the external potential of the ions [37, 38]. Alternatively, the electrons may be propagated in real time using the time-dependent formulation of DFT [37, 39]. While promising results have been demonstrated using DFT-based methods, including the dynamic structure factor [40] and transport coefficients [41], there remain some unresolved theoretical uncertainties. These include the choice of exchange-correlation functional, especially in time-dependent formulations [37]. In DFT-MD, some authors argue that electron–electron collisions are not included in dynamic properties such as electrical conductivity [42]. Furthermore, under the Born–Oppenheimer approximation, the ions and electrons cannot exchange energy, limiting extensions to electron–ion relaxation and more general nonthermal velocity distribution problems. Some works have also suggested that this limitation could complicate predictions of ionic transport properties [43].

A fundamental limitation of direct simulation with the PIMC and DFT methods is that they are unfeasibly computationally expensive for large numbers of particles. One of the motivations of the work presented in this thesis is therefore the development of *scalable* models, meaning that, as particle number is increased, simulation cost does not increase too quickly. For example, in its most efficient implementation, the computational cost of classical MD with short-range pair potentials is proportional to the number of particles N, allowing large systems to be modelled. Scalable models are particularly useful in making contact with the hydrodynamic (large-lengthscale) limit [34, 44]. These models are suitable for direct molecular dynamics simulation and therefore incorporate the electrons through effective interatomic potentials or treat them explicitly as localised particles. Explicit examples are given in Chapter 2. An additional motivation for developing dynamic electron MD techniques

is their ability to probe coupled electron–ion dynamics over long timescales that are currently out of reach for time-dependent DFT simulation. Furthermore, this thesis is concerned with developing MD models in the *chemical picture*, which provides an unambiguous interpretation of the charge state distribution and mean ionisation state of warm dense materials.

1.5 Thesis Structure and author contributions

In this section, a brief overview of the structure of this thesis is provided. While all presented results were obtained by the author, specific support was given for various parts of the work, as highlighted below. Throughout this work, general supervision was provided by the author's primary supervisor, Professor Gianluca Gregori. Additionally, this work was synthesised in close collaboration with former DPhil student (now postdoctoral researcher) Dr Pontus Svensson.

Chapter 2 provides an overview of existing theoretical background required to understand the remainder of the thesis. This includes an introduction to the basic principles of MD and associated numerical techniques. An introduction to common models for non-ideal plasma is also given. This chapter does not provide any new results, but does offer pedagogical novelty in its presentation of the Ewald summation and gauge fixing for Coulomb systems.

In Chapter 3, the Coulomb one-component plasma model is extended to include bound electrons. First, the concept of the *chemical picture* is introduced, which is used throughout this thesis to extend fully ionised models into the partially-ionised regime. To compute the self-consistent ionisation state of the model, a free energy minimisation framework is developed. This allows concepts such as ionisation potential depression (IPD) and pressure ionisation to be explored and compared against simpler analytical models. This chapter is based on material published in Ref. [45].

The extension of an existing wave packet molecular dynamics (WPMD) model developed in Ref. [46] to partially-ionised conditions is presented in Chapter 4. This involves an explicit bound-state wavefunction model with appropriate interactions. Additional theoretical

background and motivation for the WPMD method are also provided. Dr Pontus Svensson provided the existing MD implementation and analysis code, which the author extended accordingly. Combining this development with the free energy minimisation framework established in Chapter 3 allows the model-dependent ionisation state to be calculated, and the resulting structural properties to be compared with available path integral Monte Carlo data [47]. The material in this chapter is based on Ref. [48].

While the bulk of this thesis is concerned with extending models to the partially-ionised regime, Chapter 5 investigates general properties of the WPMD method. Specifically, a non-interacting, classical statistical theory is developed to predict the distribution of quantum degrees of freedom in the model. Good agreement is found between the theory and data from interacting molecular dynamics. The material in this chapter is based on Ref. [49].

This thesis concludes in Chapter 6, where an overall summary of the work is provided along with suggestions for future research directions.

1.6 Author publications

The following publications were produced during the course of this DPhil and are presented in chronological order, together with a summary of the author's contributions to each.

1. **D. Plummer** *et al.*, Ionization calculations using classical molecular dynamics, Phys. Rev. E **111**, 015204 (2025).

   Contribution: Developed the models and associated molecular dynamics code, performed the simulations, and wrote the original draft.

2. P. Svensson *et al.*, Modeling of warm dense hydrogen via explicit real-time electron dynamics: Electron transport properties, Phys. Rev. E **111**, 045208 (2025).

   Contribution: Assisted with theoretical developments and manuscript revision.

3. T. Campbell *et al.*, Molecular dynamics framework coupled with smoothed particle hydrodynamics for quantum plasma simulations, Phys. Rev. Research **7**, 023286 (2025).

Contribution: Performed initial numerical tests of the smoothed particle hydrodynamics scheme and contributed to manuscript revision.

4. M. Luo *et al.*, Learning heat transport kernels using a nonlocal heat transport theory-informed neural network, Phys. Rev. Research **7**, L042017 (2025).
   Contribution: Assisted with interpretation of results and manuscript revision.

5. M. Luo *et al.*, Time-embedded convolutional neural networks for modeling plasma heat transport, Phys. Rev. E **113**, 035303 (2026).
   Contribution: Assisted with interpretation of results and manuscript revision.

6. **D. Plummer** *et al.*, Modeling partially ionized dense plasma using wavepacket molecular dynamics, Phys. Rev. E **113**, 045206 (2026).
   Contribution: Developed and implemented the numerical scheme in an existing in-house code, performed the simulations, and wrote the original manuscript.

7. **D. Plummer** *et al.*, Statistical theory of electronic degrees of freedom in wave packet molecular dynamics, Phys. Rev. E **114**, 015219 (2026).
   Contribution: Developed the theory and sampling code, performed the simulations, and wrote the original manuscript.

Chapter 2

Molecular dynamics for non-ideal plasmas

This thesis focuses on the development of molecular dynamics (MD) models for the simulation of partially-ionised dense plasma. MD is a versatile simulation framework for resolving the time-dependent trajectories of the constituent particles of matter. In its most common formulation, the dynamical evolution of atoms or ions is computed explicitly, while the effects of the quantum-mechanical electrons are incorporated implicitly through an effective interatomic force field. Alternatively, there are MD-based approaches in which the electronic degrees of freedom are treated explicitly and evolved alongside the ions. In the plasma-physics context of this thesis, these approaches are classified as either one-component plasma (OCP) models—where only the ionic species are treated explicitly—or two-component plasma (TCP) models, in which both ions and electrons are modelled dynamically. Both classes of models are investigated here. In Chapter 3, the properties of partially-ionised dense plasma are examined using a set of OCP-inspired models. Chapter 4 extends wave packet molecular dynamics (WPMD), a TCP approach, to the partially-ionised regime. Finally, Chapter 5 explores the statistical properties of WPMD. Accordingly, after introducing the basic principles of molecular dynamics in the following section, a general overview of these two classes of models is presented.

2.1 Basic principles

The numerical framework of MD and its statistical-mechanical foundations are well established and have been extensively discussed in standard texts (e.g., books [50–53]). The following subsections summarise the concepts most relevant to this work.

2.1.1 Equations of motion

For the sake of simplicity, in this section, a set of N classical particles enclosed in a three-dimensional region with fixed volume V is considered. Each particle is labelled by $i = 1, \ldots, N$,

and the total system evolves in a phase space parameterised by the set of all positions and momenta $\{\boldsymbol{r}_i, \boldsymbol{p}_i\}$, which is a shorthand notation for $\{\boldsymbol{r}_i, \boldsymbol{p}_i\}_{i=1}^{N}$. For particles interacting through the potential energy function $\mathcal{V}(\{\boldsymbol{r}_i\})$, the Newtonian equations of motion for the i-th particle with mass m_i are

$$\frac{d\boldsymbol{r}_i}{dt} = \frac{\boldsymbol{p}_i}{m_i} \tag{2.1.1a}$$

$$\frac{d\boldsymbol{p}_i}{dt} = -\frac{\partial \mathcal{V}}{\partial \boldsymbol{r}_i}. \tag{2.1.1b}$$

The central idea of MD is to integrate these equations in time for a many-particle system in a computationally efficient way. It is well known that direct integration of these equations conserves the total energy of the system,

$$E = \mathcal{H}(\{\boldsymbol{r}_i, \boldsymbol{p}_i\}) = \sum_i \frac{\boldsymbol{p}_i^2}{2m_i} + \mathcal{V}(\{\boldsymbol{r}_i\}) = \mathcal{T} + \mathcal{V}, \tag{2.1.2}$$

where $\mathcal{H}$ is the classical Hamiltonian of the system. The conservation of particle number N, volume V, and energy E means that, under the assumption of ergodicity [50], the microcanonical ensemble is sampled. This is often referred to as the NVE ensemble in the context of MD. The equations of motion in Eq. (2.1.1) can be modified to sample different statistical ensembles, such as the NVT (canonical) ensemble via thermostatting schemes [54, 55]. Furthermore, by introducing the simulation volume as a dynamical variable, one can formulate evolution equations that sample constant-pressure ensembles [56, 57].

All data collection simulations in this work are performed in the NVE ensemble. However, using the fact that ensemble averages of equilibrium observables in different ensembles are equivalent in the thermodynamic limit allows quantities of interest to be formulated using the canonical ensemble in the following explanations, despite the underlying molecular dynamics being microcanonical. For example, temperature is still used to characterise the thermodynamic state of the system. This is appropriate because, for a sufficiently large

many-body system in the microcanonical ensemble, the instantaneous kinetic temperature

$$T(t) = \frac{2}{3k_B N} \sum_{i=1}^{N} \frac{\boldsymbol{p}_i^2(t)}{2m_i}, \tag{2.1.3}$$

shows only small fluctuations about a well-defined mean value corresponding to the thermodynamic temperature [51].

It is important to note, however, that while thermostatting schemes modify the equations of motion in order to sample a desired equilibrium probability distribution, they generally alter the real-time dynamics of the system. As a result, time-correlation functions—and hence dynamical properties such as transport coefficients—may be distorted when computed directly from thermostatted trajectories.

2.1.2 Ensemble averages

Consider an observable $A(\{\boldsymbol{r}_i, \boldsymbol{p}_i\})$ that depends on the microscopic state of the system. In equilibrium statistical mechanics, the canonical ensemble average may be written [52]

$$\langle A \rangle = \frac{1}{h^{3N} N!} \frac{1}{Z} \int \prod_{i=1}^{N} \mathrm{d}^3\boldsymbol{r}_i \mathrm{d}^3\boldsymbol{p}_i \, A(\{\boldsymbol{r}_i, \boldsymbol{p}_i\}) \exp\left(-\beta \mathcal{H}(\{\boldsymbol{r}_i, \boldsymbol{p}_i\})\right), \tag{2.1.4}$$

where the product over $d^3\boldsymbol{r}_i d^3\boldsymbol{p}_i$ denotes a phase-space volume element, $\beta = 1/(k_B T)$ is the inverse temperature in energy units, and the canonical partition function is

$$Z = \frac{1}{h^{3N} N!} \int \prod_{i=1}^{N} \mathrm{d}^3\boldsymbol{r}_i \mathrm{d}^3\boldsymbol{p}_i \exp\left(-\beta \mathcal{H}(\{\boldsymbol{r}_i, \boldsymbol{p}_i\})\right). \tag{2.1.5}$$

The prefactor $1/(h^{3N} N!)$, where h is Planck's constant, arises from quantum statistical considerations [23].

In molecular dynamics simulations, ensemble averages are obtained by computing time

averages along a trajectory generated by integrating the equations of motion,

$$\bar{A} = \lim_{T\to\infty} \frac{1}{T} \int_0^T A(\{\boldsymbol{r}_i(t), \boldsymbol{p}_i(t)\})\mathrm{d}t. \tag{2.1.6}$$

Under the assumption of ergodicity, time averages obtained from the NVE dynamics are equivalent to NVE ensemble averages, i.e. $\bar{A} = \langle A \rangle$ [52]. Furthermore, in the thermodynamic limit, ensemble equivalence ensures that NVE and NVT ensemble averages are the same. The implication of these results is that statistical observables can be extracted from a single, sufficiently long MD trajectory. Of course, in a numerical simulation, the trajectory $\{\boldsymbol{r}_i(t), \boldsymbol{p}_i(t)\}$ is only available at discrete timesteps. Therefore, the integral, Equation (2.1.6), is approximated by a discrete average over configurations sampled at finite time intervals after the system has reached equilibrium.

2.1.3 Thermodynamic integration

As discussed in the previous section, physical observables may be calculated by sampling them in time. However, there is a class of properties that are not directly available in atomistic simulation (or experiment) because they depend on the extent of the underlying phase space itself and cannot be written as an ensemble average. For example, the Helmholtz free energy

$$F = -k_B T \ln Z, \tag{2.1.7}$$

depends directly on the partition function and is therefore unavailable. This is particularly relevant for the work presented in this thesis, which relies on the premise that a system will adjust its ionisation state to minimise the Helmholtz free energy in equilibrium (see Section 3.1). Therefore, a method to compute the free energy is required. While many methods are available [50], perhaps the most successful is the method of thermodynamic integration (TI), which refers to two closely related, but theoretically distinct, methods to compute the free energy. In the statistical route, a coupling parameter λ is introduced in the

Hamiltonian. For example, consider a redefined Hamiltonian $\mathcal{H}(\lambda)$ which now depends on a coupling parameter λ, where $\mathcal{H}(\lambda = 0)$ represents the Hamiltonian of a reference system and $\mathcal{H}(\lambda = 1)$ represents the Hamiltonian of a target system. The free energy of a system is, in general, a functional of the Hamiltonian, and is therefore λ dependent, i.e. $F = F(\lambda)$. Taking the derivative of the free energy with respect to the coupling parameter yields

$$\begin{aligned}\frac{\partial F}{\partial \lambda} &= -\frac{1}{Z}\frac{\partial Z}{\partial \lambda} \\ &= \frac{1}{h^{3N}N!}\frac{1}{Z}\int \prod_{i=1}^{N} \mathrm{d}^3\boldsymbol{r}_i \mathrm{d}^3\boldsymbol{p}_i \left(\frac{\partial \mathcal{H}}{\partial \lambda}\right) \exp\left(-\beta \mathcal{H}(\{\boldsymbol{r}_i, \boldsymbol{p}_i\})\right) \\ &= \left\langle \frac{\partial \mathcal{H}}{\partial \lambda} \right\rangle_\lambda .\end{aligned} \tag{2.1.8}$$

where $\langle \cdot \rangle_\lambda$ denotes an ensemble average at a fixed coupling parameter (λ). From a time averaging perspective, this means the trajectories are generated from the Hamiltonian $\mathcal{H}$ at the specified value of λ, and then the derivative of the Hamiltonian, $\langle \partial \mathcal{H}/\partial \lambda \rangle_\lambda$, is computed along these trajectories. The free energy of the target system may be obtained by integrating Equation (2.1.8). Generally,

$$F(\lambda = 1) = F(\lambda = 0) + \int_0^1 \left\langle \frac{\partial \mathcal{H}}{\partial \lambda} \right\rangle_\lambda \mathrm{d}\lambda. \tag{2.1.9}$$

The method of TI therefore provides a map between the free energy of a reference system at $\lambda = 0$, which typically has known free energy, and the free energy of a target system, at $\lambda = 1$, providing a way of connecting the free energy with ensemble averages that are available from MD simulation. However, the trade-off of this exchange is apparent from Equation (2.1.9); to numerically evaluate the integral, ensemble averages across a range of different coupling parameters are required, meaning equilibrium MD data is required at a set of different coupling parameters. The choice of exactly how the coupling parameter is introduced can influence the stability of the scheme, and can be used to avoid numerical instabilities in the integrand of Equation (2.1.9), see e.g., Ref. [58]. A particularly common

way of introducing the coupling parameter is given by

$$\mathcal{H} = \mathcal{T} + \lambda \mathcal{U}. \tag{2.1.10}$$

This form allows the free energy to be computed by performing MD simulations with interactions scaled by λ and averaging the full interaction potential over these trajectories, given that $\left\langle \frac{\partial \mathcal{H}}{\partial \lambda} \right\rangle_\lambda = \langle \mathcal{U} \rangle_\lambda$ in this case. Furthermore, the free energy of the reference ($\lambda = 0$) system is an ideal gas, which has known free energy F_{id}.

The alternative formulation of TI appeals directly to standard thermodynamic relations and does not rely explicitly on statistical-mechanical arguments. While a variety of equivalent thermodynamic identities may be employed, the relation most relevant to this thesis is a Gibbs–Helmholtz-type identity for the Helmholtz free energy,

$$U = -T^2 \left(\frac{\partial}{\partial T} \frac{F}{T} \right)_{V,N}, \tag{2.1.11}$$

where U denotes the internal energy. This identity allows the Helmholtz free energy to be obtained by integration from a reference temperature T_0,

$$\frac{F(T)}{T} - \frac{F(T_0)}{T_0} = -\int_{T_0}^{T} \frac{U(T')}{T'^2} \mathrm{d}T'. \tag{2.1.12}$$

The integration is carried out along a fixed-volume and fixed-particle-number thermodynamic path. This formula is used to develop an expression for the free energy of a one-component plasma in Chapter 3, where the integration is performed from a weakly coupled system at high temperature, where analytical forms of the free energy are known.

2.1.4 Numerical techniques

Molecular dynamics (MD) simulations are based on the numerical integration of the classical equations of motion for a many-particle system. Equations (2.1.1) are evolved forward in time using finite-difference integration schemes. The most commonly used scheme is the

velocity–Verlet integrator [51], which is second-order accurate in the time step and symplectic, meaning that it exactly preserves phase-space volume. This property leads to good long-time energy stability in Hamiltonian systems. Denoting the position and velocity at a given time t as $\boldsymbol{r}_j(t)$ and $\boldsymbol{v}_j(t) = \boldsymbol{p}_j(t)/m_j$ respectively, the velocity–Verlet algorithm updates the variables in a "leapfrog" fashion through the following iterative equations:

$$\begin{aligned} \boldsymbol{v}_j\Big(t + \tfrac{\Delta t}{2}\Big) &= \boldsymbol{v}_j(t) + \frac{\Delta t}{2m_j}\boldsymbol{F}_j(t) \\ \boldsymbol{r}_j(t + \Delta t) &= \boldsymbol{r}_j(t) + \Delta t\, \boldsymbol{v}_j\left(t + \tfrac{\Delta t}{2}\right) \\ \boldsymbol{v}_j(t + \Delta t) &= \boldsymbol{v}_j\Big(t + \tfrac{\Delta t}{2}\Big) + \frac{\Delta t}{2m_j}\boldsymbol{F}_j(t + \Delta t). \end{aligned} \tag{2.1.13}$$

Explicitly, the force on the j-th particle is

$$\boldsymbol{F}_j(t) = -\frac{\partial \mathcal{V}\Big(\{\boldsymbol{r}_j\}\Big)}{\partial \boldsymbol{r}_j(t)}. \tag{2.1.14}$$

Evaluating the force for a large many-particle system is typically the most computationally demanding step. For short-ranged interactions, this cost is reduced by introducing neighbour lists, which restrict force calculations to particles within a specified cutoff radius. Combined with spatial binning, this allows the computational effort to scale approximately linearly with system size. For systems with long-ranged interactions, such as Coulombic systems, specialised algorithms are required (see Section 2.2.1). These include the Ewald summation and particle–mesh methods, which split the interaction into short-range and long-range components and evaluate the latter efficiently in reciprocal space.

Modern MD simulations are commonly performed on parallel computing architectures. Parallelisation is most often achieved through spatial domain decomposition, in which the simulation volume is divided into subdomains that are distributed across processors. Each processor advances the particles within its assigned domain and exchanges boundary information with neighbouring domains using message-passing protocols. This approach enables efficient scaling to large particle numbers and high-performance computing systems.

In this thesis, all MD simulations were performed using the Large-scale Atomic/Molecular Massively Parallel Simulator (LAMMPS), an open-source molecular dynamics code that implements these numerical techniques in a highly scalable and extensible framework [59]. LAMMPS provides a wide range of integration algorithms, force calculation methods for both short- and long-ranged interactions, and efficient parallelisation via domain decomposition, making it well suited to the large-scale simulations of dense and partially-ionised plasmas considered here.

2.2 Coulomb interactions

When charges separate due to thermal and pressure ionisation effects, matter can no longer be modelled as a collection of charge-neutral objects (i.e. atoms and molecules) and instead must be described as a system of charged particles (ions and electrons) interacting through electromagnetic forces. Under the warm dense matter conditions relevant to this thesis, typical thermal velocities are small compared to the speed of light, so magnetic interactions and retardation effects are small relative to electrostatic forces. Therefore, as is standard within the field, only electrostatic interactions are considered. Additionally, periodic boundary conditions are employed to represent the bulk physics of warm dense matter and minimise surface effects.

2.2.1 Ewald potential

The electrostatic energy of a bare point charge diverges under periodic boundary conditions. It is therefore standard to endow the charge with a uniform charge-neutralising background and to characterise it as a *pseudo ion* [60]. Restricting to a cubic periodic box of side length L and volume $V = L^3$, the resulting charge density of a pseudo ion located at position $\boldsymbol{r}_i$ is defined as

$$\rho_i(\boldsymbol{r}) = q_i \left(\delta(\boldsymbol{r} - \boldsymbol{r}_i) - \frac{1}{V} \right), \tag{2.2.1}$$

where $q_i = Z_i e$ is the charge of the ion. The charge distribution of a two-component plasma of point charges may be constructed by superposing charges of opposite sign, such that

$$\sum_i q_i = Q = 0, \tag{2.2.2}$$

where Q is the total charge. In the case that $Q = 0$, there is a cancellation of the uniform background terms. The electrostatic potential ψ_i generated by the pseudo ion is a solution of Poisson's equation:

$$\nabla^2 \psi_i(\boldsymbol{r}) = -\frac{\rho_i(\boldsymbol{r})}{\varepsilon_0}. \tag{2.2.3}$$

To solve Poisson's equation in the presence of periodic boundary conditions, both the charge density and electrostatic potential may be expanded as discrete Fourier series:

$$\rho_i(\boldsymbol{r}) = \frac{1}{V} \sum_{\boldsymbol{k}} \tilde{\rho}_i(\boldsymbol{k}) \exp(i\boldsymbol{k} \cdot \boldsymbol{r}) \tag{2.2.4}$$

$$\psi_i(\boldsymbol{r}) = \frac{1}{V} \sum_{\boldsymbol{k}} \tilde{\psi}_i(\boldsymbol{k}) \exp(i\boldsymbol{k} \cdot \boldsymbol{r}). \tag{2.2.5}$$

The $\boldsymbol{k}$-vectors are given by $\boldsymbol{k} = 2\pi \boldsymbol{n}/L$ where $\boldsymbol{n} \in \mathbb{Z}^3$ is a vector of integers. The Fourier coefficients of the pseudo ion charge density are given by the following volume integral,

$$\tilde{\rho}_i(\boldsymbol{k}) = \int_V \rho_i(\boldsymbol{r}) \exp(-i\boldsymbol{k} \cdot \boldsymbol{r}) \mathrm{d}^3\boldsymbol{r} = \begin{cases} q_i \exp(-i\boldsymbol{k} \cdot \boldsymbol{r}_i) & \boldsymbol{k} \neq \boldsymbol{0} \\ 0 & \boldsymbol{k} = \boldsymbol{0}, \end{cases} \tag{2.2.6}$$

where $\boldsymbol{0}$ denotes the zero vector. The presence of the uniform background removes the $\boldsymbol{k} = \boldsymbol{0}$ mode and therefore suppresses divergent long-range Coulomb energy contributions, ensuring that the solution to Poisson's equation is well defined under periodic boundary conditions. Inserting Equations (2.2.4) and (2.2.5) into the Poisson equation (2.2.3), and operating with the Laplacian yields

$$-\frac{1}{V} \sum_{\boldsymbol{k}} \tilde{\psi}_i(\boldsymbol{k}) k^2 \exp(i\boldsymbol{k} \cdot \boldsymbol{r}) = -\frac{1}{\varepsilon_0 V} \sum_{\boldsymbol{k} \neq 0} q_i \exp(i\boldsymbol{k} \cdot (\boldsymbol{r} - \boldsymbol{r}_i)), \tag{2.2.7}$$

where $k^2 = \boldsymbol{k} \cdot \boldsymbol{k}$. This equation must hold for all $\boldsymbol{r}$, which is only possible if

$$\tilde{\psi}_i(\boldsymbol{k}) = \frac{q_i}{\varepsilon_0 k^2} \exp(-i\boldsymbol{k} \cdot \boldsymbol{r}_i), \tag{2.2.8}$$

when $\boldsymbol{k} \neq \boldsymbol{0}$. The full electrostatic potential of the pseudo ion may now be written as

$$\psi_i(\boldsymbol{r}) = \frac{\tilde{\psi}_i(\boldsymbol{0})}{V} + \frac{q_i}{\varepsilon_0 V} \sum_{\boldsymbol{k} \neq 0} \frac{1}{k^2} \exp\left[i\boldsymbol{k} \cdot (\boldsymbol{r} - \boldsymbol{r}_i)\right]. \tag{2.2.9}$$

The term associated with the $\boldsymbol{k} = \boldsymbol{0}$ mode corresponds to a spatial average of the real-space potential and is not fixed by Poisson's equation. In open (non-periodic) space, the gauge is typically fixed by requiring that the electrostatic potential tends to zero infinitely far away from the charge distribution. However, in periodic boundary conditions, this is not valid given that the charge distribution is infinitely repeated. A standard choice to fix the gauge, which is used throughout this thesis, is to set the spatial average of the periodic potential to zero:

$$\frac{1}{V} \int_V \psi_i(\boldsymbol{r}) \mathrm{d}^3\boldsymbol{r} = \frac{\tilde{\psi}_i(\boldsymbol{0})}{V} \equiv 0, \tag{2.2.10}$$

which yields the final expression [18, 60]

$$\psi_i(\boldsymbol{r}) = \frac{q_i}{\varepsilon_0 V} \sum_{\boldsymbol{k} \neq 0} \frac{1}{k^2} \exp\left[i\boldsymbol{k} \cdot (\boldsymbol{r} - \boldsymbol{r}_i)\right]. \tag{2.2.11}$$

Although this representation is correct, it is not well-suited to numerical evaluation. Accurately resolving the short-range singularity of the Coulomb interaction requires the inclusion of a large number of reciprocal-space modes, leading to slow convergence. More generally, the Coulomb potential under periodic boundary conditions exhibits two distinct features. First, it is long-ranged, decaying slowly with separation, so that each charge interacts with an infinite set of its periodic images; this behaviour is naturally described in reciprocal space. Second, the potential contains a short-range singularity as $r \to 0$, which is inefficiently captured by a Fourier representation but is straightforward to evaluate in real space.

These observations motivate the standard Ewald strategy [51] of decomposing the charge density into two contributions: a smooth, long-range component ρ^L, which is treated in reciprocal space, and a charge-neutral short-range component ρ^S, which is spatially localised and evaluated directly in real space. The full decomposition may be written

$$\rho_i(\boldsymbol{r}) = \rho_i^S(\boldsymbol{r}) + \rho_i^L(\boldsymbol{r}). \tag{2.2.12}$$

Including the uniform background, the charge distributions take the form:

$$\rho_i^S(\boldsymbol{r}) = q_i\delta(\boldsymbol{r} - \boldsymbol{r}_i) - q_i n_G(\boldsymbol{r} - \boldsymbol{r}_i) \tag{2.2.13}$$

$$\rho_i^L(\boldsymbol{r}) = q_i n_G(\boldsymbol{r} - \boldsymbol{r}_i) - \frac{q_i}{V}, \tag{2.2.14}$$

where $q_i n_G(\boldsymbol{r})$ is a screening charge cloud. A very common choice for this object is a Gaussian function due to its well-known analytical properties. Explicitly, we use the following charge density to screen the point charge

$$q_i n_G(\boldsymbol{r}) = q_i \left(\frac{\alpha}{\sqrt{\pi}}\right)^3 \exp\left[-\alpha^2 r^2\right]. \tag{2.2.15}$$

Here, α is the *Ewald parameter*, which controls the lengthscale over which the short-range distribution is screened. This Gaussian charge generates the following electrostatic potential in open (non-periodic) space:

$$\psi_{G,i}(r) = \frac{q_i}{4\pi\varepsilon_0}\frac{\mathrm{erf}(\alpha r)}{r}. \tag{2.2.16}$$

Note that the long-range charge distribution is globally neutralised over the whole box, whereas the short-range charge distribution is neutralised on the lengthscale of $1/\alpha$. This decomposition is visualised in Figure 2.1. The electrostatic potential may also be split into short- and long-range parts accordingly,

$$\psi_i(\boldsymbol{r}) = \psi_i^S(\boldsymbol{r}) + \psi_i^L(\boldsymbol{r}), \tag{2.2.17}$$

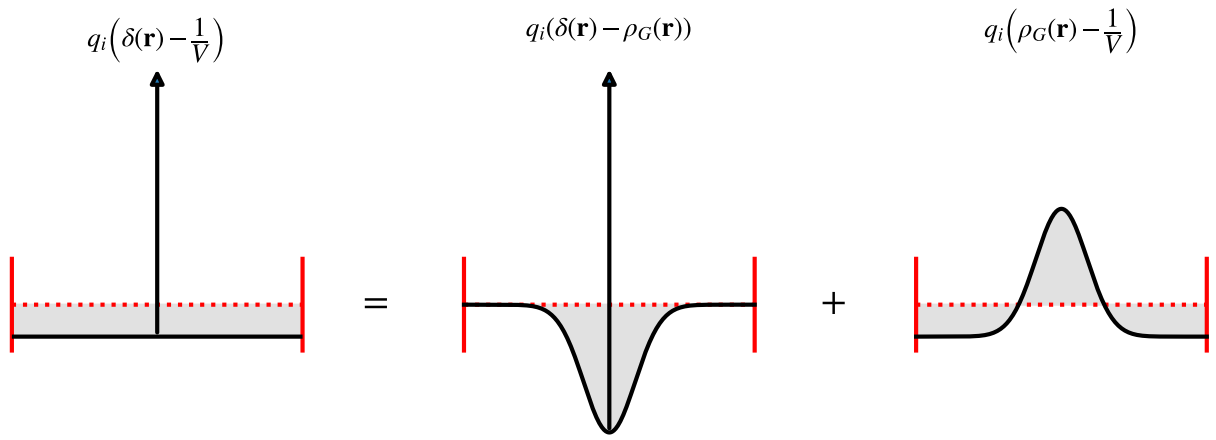

Figure 2.1: Schematic of the Ewald charge-splitting procedure under periodic boundary conditions. The red dotted line indicates the x axis, while the red vertical lines denote the boundaries of the simulation cell. The pseudo ion charge density $q_i(\delta(\boldsymbol{r}) - 1/V)$ (left) is decomposed into a short-range, charge-neutral component $q_i(\delta(\boldsymbol{r}) - \rho_G(\boldsymbol{r}))$ (centre) and a smooth, long-range component $q_i(\rho_G(\boldsymbol{r}) - 1/V)$ (right). The short-range contribution is locally neutralised on the length scale $1/\alpha$, whereas the long-range contribution is globally neutralised by the uniform background.

where, by linearity, each part satisfies its own respective Poisson's equation. Under periodic boundary conditions, Poisson's equation determines the electrostatic potential only up to an additive constant. Consequently, the short- and long-range potentials ψ^S and ψ^L are individually defined only up to arbitrary constants; a specific choice of gauge is therefore required to fix the overall constant. It is natural to solve Poisson's equation for the short-range potential in real space. Therefore, instead of relying on a Fourier series to impose periodicity, the charge distribution itself is written as a sum over integer vectors $\boldsymbol{n} \in \mathbb{Z}^3$:

$$\rho^S_{i,\mathrm{per}}(\boldsymbol{r}) = \sum_{\boldsymbol{n}} \left(q_i \delta(\boldsymbol{r} - \boldsymbol{r}_i + \boldsymbol{n}L) - q_i n_G(\boldsymbol{r} - \boldsymbol{r}_i + \boldsymbol{n}L)\right), \tag{2.2.18}$$

where $\rho^S_{i,\mathrm{per}}$ is the short-range charge distribution with explicit periodicity. Using the well-known real-space solutions to Poisson's equation for a delta function and the result for a

free-space Gaussian (Equation (2.2.16)), the electrostatic potential is

$$\psi_i^S(\boldsymbol{r}) = \frac{q_i}{4\pi\varepsilon_0} \sum_{\boldsymbol{n}\in\mathbb{Z}^3} \left(\frac{1}{|\boldsymbol{r}-\boldsymbol{r}_i+\boldsymbol{n}L|} - \frac{\operatorname{erf}(\alpha|\boldsymbol{r}-\boldsymbol{r}_i+\boldsymbol{n}L|)}{|\boldsymbol{r}-\boldsymbol{r}_i+\boldsymbol{n}L|} \right) + \mathcal{C} \tag{2.2.19}$$

$$= \frac{q_i}{4\pi\varepsilon_0} \sum_{\boldsymbol{n}\in\mathbb{Z}^3} \frac{\operatorname{erfc}(\alpha|\boldsymbol{r}-\boldsymbol{r}_i+\boldsymbol{n}L|)}{|\boldsymbol{r}-\boldsymbol{r}_i+\boldsymbol{n}L|} + \mathcal{C}, \tag{2.2.20}$$

where $\operatorname{erfc}(\cdot)$ is the complementary error function and $\mathcal{C}$ is an unspecified integration constant which shall be fixed by the gauge. Similar to the calculation of Equation (2.2.5), the long-range potential is naturally solved in reciprocal space. Following similar steps to Equations (2.2.4) through to (2.2.8) yields

$$\psi_i^L = \frac{\tilde{\psi}_i^L(\boldsymbol{0})}{V} + \frac{q_i}{\varepsilon_0 V} \sum_{\boldsymbol{k}\neq\boldsymbol{0}} \frac{1}{k^2} \exp\left[-k^2/(4\alpha^2)\right] \exp\left[i\boldsymbol{k}\cdot(\boldsymbol{r}-\boldsymbol{r}_i)\right], \tag{2.2.21}$$

where the difference arises from a Gaussian charge distribution giving an additional exponential factor in the sum and, as before, the $\boldsymbol{k}=\boldsymbol{0}$ mode is undetermined. The final step is to impose the gauge condition. This requires averaging the charge-splitted electrostatic potential over the box:

$$\frac{1}{V}\int \left(\psi_i^S(\boldsymbol{r}) + \psi_i^L(\boldsymbol{r})\right) \mathrm{d}^3\boldsymbol{r} = \mathcal{C} + \frac{\tilde{\psi}_i^L(\boldsymbol{0})}{V} + \frac{q_i}{4\pi\varepsilon_0 V} \sum_{\boldsymbol{n}\in\mathbb{Z}^3} \int_V \frac{\operatorname{erfc}(\alpha|\boldsymbol{r}-\boldsymbol{r}_i+\boldsymbol{n}L|)}{|\boldsymbol{r}-\boldsymbol{r}_i+\boldsymbol{n}L|} \mathrm{d}^3\boldsymbol{r}. \tag{2.2.22}$$

Given that the final integral involves a sum over periodic boxes, it may be replaced by a volume integral over $\mathbb{R}^3$ with an appropriate change of integrand. After changing integration variables, the final integral corresponds to the following volume integral over all space which can be solved in spherical coordinates:

$$\sum_{\boldsymbol{n}\in\mathbb{Z}^3} \int_V \frac{\operatorname{erfc}(\alpha|\boldsymbol{r}-\boldsymbol{r}_i+\boldsymbol{n}L|)}{|\boldsymbol{r}-\boldsymbol{r}_i+\boldsymbol{n}L|} \mathrm{d}^3\boldsymbol{r} = \int_{\mathbb{R}^3} \frac{\operatorname{erfc}(\alpha r)}{r} \mathrm{d}^3\boldsymbol{r} = \frac{\pi}{\alpha^2}. \tag{2.2.23}$$

Therefore, applying the gauge fixing condition, Equation (2.2.10), gives

$$\mathcal{C} + \frac{\tilde{\psi}_i^L(\mathbf{0})}{V} = -\frac{1}{4\pi\varepsilon_0}\frac{q_i\pi}{\alpha^2 V}. \tag{2.2.24}$$

Putting these results together, the final electrostatic potential using the charge splitting procedure is

$$\begin{aligned}\psi_i(\boldsymbol{r}) = \frac{q_i}{4\pi\varepsilon_0}\Bigg(&\sum_{\boldsymbol{n}\in\mathbb{Z}^3}\frac{\operatorname{erfc}\left(\alpha\left|\boldsymbol{r}-\boldsymbol{r}_i+\boldsymbol{n}L\right|\right)}{\left|\boldsymbol{r}-\boldsymbol{r}_i+\boldsymbol{n}L\right|}\\ &+\frac{4\pi}{V}\sum_{\boldsymbol{k}\neq 0}\frac{\exp\left[-k^2/4\alpha^2\right]}{k^2}\exp\left[i\boldsymbol{k}\cdot\left(\boldsymbol{r}-\boldsymbol{r}_i\right)\right]-\frac{\pi}{\alpha^2 V}\Bigg).\end{aligned} \tag{2.2.25}$$

This is the standard Ewald form available in, for example, Refs. [18, 61–63]. Note that Gaussian or OCP unit systems are often used, sometimes in combination with the choice $\alpha = \sqrt{\pi}/L$. Many sources do not explicitly address the gauge fixing described here. As has been shown, the final term is equal to the volume integral of the short-range electrostatic potential over the box, and is responsible for ensuring the total electrostatic potential does not depend on the Ewald parameter α. This is equivalent to the statement

$$\frac{\partial\psi_i(\boldsymbol{r})}{\partial\alpha} = 0, \tag{2.2.26}$$

which can be explicitly shown. Although this property has been previously noted [64], it is typically not explicitly linked to gauge fixing requirements. If this final term is not included, different Ewald parameters correspond to different gauge choices, and naively computing the electrostatic energy would render different zeros of energy. This is especially important when comparing simulations with different particle number when a uniform background is present, as performed in Chapter 3. The Ewald parameter controls the tradeoff between the real- and reciprocal-space sum convergence rates and is typically chosen to optimise numerical efficiency. An equivalent derivation of the Ewald technique when $Q = 0$ (i.e. there is no

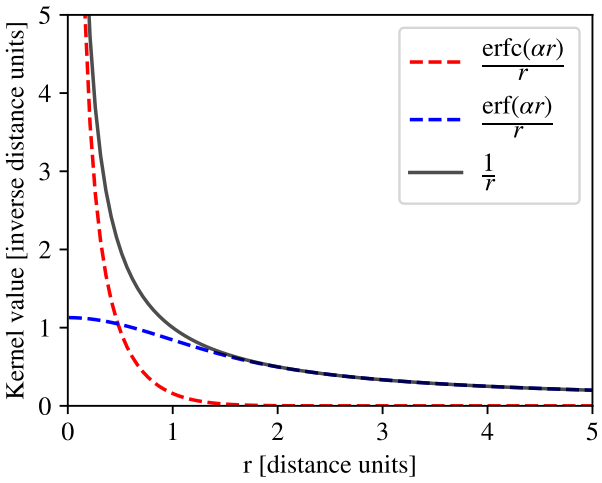

Figure 2.2: Illustration of the Ewald decomposition of the Coulomb kernel corresponding to Equation (2.2.27). In this figure the Ewald splitting parameter is set to $\alpha = 1$ in the chosen arbitrary distance units.

uniform background) involves performing a direct decomposition of the Coulomb kernel:

$$\frac{1}{r} = \frac{\operatorname{erfc}(\alpha r)}{r} + \frac{\operatorname{erf}(\alpha r)}{r}, \tag{2.2.27}$$

which is equivalent to the charge density splitting performed in this section. The derivation then proceeds by treating the second, long-range term in reciprocal space. In Figure 2.2, this decomposition is visualised to show the long and short-range parts of the Ewald potential. The short-range contribution, $\operatorname{erfc}(\alpha r)/r$, decays rapidly with increasing separation and is therefore well suited to evaluation directly in real space. By contrast, the complementary long-range contribution, $\operatorname{erf}(\alpha r)/r$, is smooth at the origin and varies slowly with distance, making it amenable to treatment in reciprocal space.

2.2.2 Electrostatic energy in a periodic box

Now that a general, numerically efficient form of the electrostatic potential of a pseudo ion is available, the energy of a system of charges may be calculated. The well-known general

formula for the electrostatic energy of an assembled charge distribution is

$$U = \frac{1}{2}\int \rho(\boldsymbol{r})\psi(\boldsymbol{r})\mathrm{d}\boldsymbol{r}, \tag{2.2.28}$$

where ρ is the total charge density of the system and ψ is the total electrostatic potential generated by the system. A naive application for a system of pseudo ions in periodic boundary conditions results in

$$U = \frac{1}{2}\int_V \left[\sum_i \rho_i(\boldsymbol{r})\right] \sum_j \psi_j(\boldsymbol{r})\,\mathrm{d}^3\boldsymbol{r} = \frac{1}{2}\sum_{i,j} q_i\psi_j(\boldsymbol{r}_i), \tag{2.2.29}$$

where the volume integral is over the cubic box and the double sum runs over all particles in the box. In the final equality, the gauge-fixing condition has been applied, meaning that the volume integral of the potential over the box vanishes.

Inspecting Equation (2.2.29), it is evident that the $(i = j)$ term corresponds to the pseudo ion self-energy and is divergent. A pseudo ion with charge q_i will have a self-energy of

$$\lim_{\boldsymbol{r}\to\boldsymbol{r}_i} q_i\psi_i(\boldsymbol{r}), \tag{2.2.30}$$

which includes the interaction with itself in the central box and its periodic images. The interaction with the periodic images provides a constant geometry-dependent energy contribution and should be included, while the self-interaction within the central box diverges and must be removed in classical electrostatics. The total pseudo ion self-energy may therefore be redefined as the following limit:

$$\frac{q_i^2}{4\pi\varepsilon_0 L}\xi = q_i \lim_{\boldsymbol{r}\to\boldsymbol{r}_i}\left(\psi_i(\boldsymbol{r}) - \frac{1}{4\pi\varepsilon_0|\boldsymbol{r}-\boldsymbol{r}_i|}\right), \tag{2.2.31}$$

where the dimensionless Madelung constant ξ has been introduced, and Equation (2.2.31) corresponds to a particle's interaction with its own background and array of images, while subtracting off the divergent Coulomb interaction in the central box present within the Ewald

potential ψ. Replacing the divergent self interactions in Equation (2.2.29) with this term yields a total energy of

$$U = \frac{1}{2}\sum_{i\neq j} u_{ij}(\boldsymbol{r}_{ij}) + \frac{1}{2}\sum_{i}\frac{q_i^2}{4\pi\varepsilon_0}\frac{\xi}{L}, \tag{2.2.32}$$

where $\boldsymbol{r}_{ij} = \boldsymbol{r}_i - \boldsymbol{r}_j$ is the radial separation vector. The pair potential between pseudo ions may be written explicitly as:

$$\begin{aligned} u_{ij}(\boldsymbol{r}_{ij}) =& q_i\psi_j(\boldsymbol{r}_i) \\ =& \frac{q_iq_j}{4\pi\varepsilon_0}\Bigg(\sum_{\boldsymbol{n}\in\mathbb{Z}^3}\frac{\operatorname{erfc}\left(\alpha\left|\boldsymbol{r}_{ij}+\boldsymbol{n}L\right|\right)}{\left|\boldsymbol{r}_{ij}+\boldsymbol{n}L\right|} + \frac{4\pi}{V}\sum_{\boldsymbol{k}\neq 0}\frac{\exp\left[-k^2/4\alpha^2\right]}{k^2}\exp\left[i\boldsymbol{k}\cdot\boldsymbol{r}_{ij}\right] - \frac{\pi}{\alpha^2V}\Bigg). \end{aligned} \tag{2.2.33}$$

Finally, the limit in Equation (2.2.31) is calculated. Noting that

$$\lim_{r\to 0}\left(\frac{\operatorname{erfc}(\alpha r)}{r} - \frac{1}{r}\right) = -\frac{2\alpha}{\sqrt{\pi}}, \tag{2.2.34}$$

which corresponds to the self-energy correction term, the Madelung constant divided by the box length evaluates to

$$\frac{\xi}{L} = \sum_{\boldsymbol{n}\neq\boldsymbol{0}}\frac{\operatorname{erfc}(\alpha|\boldsymbol{n}L|)}{|\boldsymbol{n}L|} + \frac{4\pi}{V}\sum_{\boldsymbol{k}\neq 0}\frac{\exp\left[-k^2/4\alpha^2\right]}{k^2} - \frac{\pi}{\alpha^2V} - \frac{2\alpha}{\sqrt{\pi}}. \tag{2.2.35}$$

When the Madelung constant ξ is multiplied by the natural Coulombic energy scale $q^2/(4\pi\varepsilon_0 L)$, this quantity gives twice the electrostatic self-energy per particle of a simple cubic lattice of unit-charge pseudo ions with lattice spacing L, including the neutralising background. Through the application of Equations (2.2.32) and (2.2.35), the total electrostatic energy of a system of charges under periodic boundary conditions may now be calculated.

2.2.3 Numerically convenient form

The total energy above is often written in a different way [51, 65, 66], which is more analogous to its direct implementation in the LAMMPS codebase. Therefore, in this section it shall be rewritten slightly, with comments on some numerical implementation details given. Specifically, in the COUL-type pair styles[1] coupled with the EWALD k-space routine, the electrostatic energy takes a different form that separates into position-dependent real (r) and reciprocal (k) parts, and two constant terms corresponding to the self (s) and correction (c) contributions. The total energy is therefore

$$U = U^{(r)} + U^{(k)} + U^{(s)} + U^{(c)}. \tag{2.2.36}$$

The first term is the real-space sum that is performed over all pairs of particles in the central box and nearby periodic images:

$$U^{(r)} = \frac{1}{4\pi\varepsilon_0}\frac{1}{2}\sum_{ij}{\sum_{\boldsymbol{n}}}' q_i q_j \frac{\operatorname{erfc}\left(\alpha\left|\boldsymbol{r}_i - \boldsymbol{r}_j + \boldsymbol{n}L\right|\right)}{\left|\boldsymbol{r}_{ij} + \boldsymbol{n}L\right|}, \tag{2.2.37}$$

where the prime on the sum over integer vectors $\boldsymbol{n}$ denotes that, when $\boldsymbol{n} = 0$, the $i = j$ terms are omitted. This real-space energy contribution includes the real-space sum in the Ewald potential and a contribution associated with the first term of the Madelung constant in Equation (2.2.35). In practice, the real-space sum is truncated with a cutoff r_c, so that only particle separations satisfying $|\boldsymbol{r}_i - \boldsymbol{r}_j + \boldsymbol{n}L| < r_c$ contribute to Equation (2.2.37). For typical choices, $r_c < L/2$ which corresponds to the *minimum image convention*: each particle pair interacts only through the closest of its periodic replicas. This convention places bounds on the value of the Ewald parameter α. Note that LAMMPS itself does not enforce the minimum image convention for the real-space energy sums, and may include contributions from multiple periodic images within the real-space cutoff [67].

1. These are a set of LAMMPS pairstyles that model charged particle interactions. Further explanation may be found within the LAMMPS documentation: `https://docs.lammps.org/pair_coul.html`.

The reciprocal space energy may be rewritten in terms of the Fourier component of the total charge density

$$\tilde{\rho}(\boldsymbol{k}) = \sum_{i}^{N} q_i \exp\left[-i\boldsymbol{k}\cdot\boldsymbol{r}_i\right], \tag{2.2.38}$$

by collating all reciprocal-space terms that occur in both the Ewald potential and Madelung self-energy:

$$\begin{aligned} U^{(k)} =& \frac{1}{4\pi\varepsilon_0}\frac{2\pi}{V}\sum_{\boldsymbol{k}\neq 0}\frac{\exp\left[-k^2/4\alpha^2\right]}{k^2}\sum_{i,j} q_i q_j \exp\left[-i\boldsymbol{k}\cdot(\boldsymbol{r}_i-\boldsymbol{r}_j)\right] \\ =& \frac{1}{4\pi\varepsilon_0}\frac{2\pi}{V}\sum_{\boldsymbol{k}\neq 0}\frac{\exp\left[-k^2/4\alpha^2\right]}{k^2}\left|\tilde{\rho}(\boldsymbol{k})\right|^2, \end{aligned} \tag{2.2.39}$$

where the sum after the first equality runs over all particles twice. This form is typically the starting point for algorithms that approximate the underlying charge distribution to achieve better computational scaling with particle number than the raw k-space sum [66]. Importantly, the computation of the instantaneous charge structure factor $|\tilde{\rho}(\boldsymbol{k})|^2$ is a global quantity and requires access to all particle positions at a given timestep. LAMMPS therefore computes this outside of the main energy compute loop which is parallelised through domain decomposition and does not have access to all particle positions. The self-energy correction term is

$$U^{(s)} = \frac{1}{4\pi\varepsilon_0}\left(-\frac{\alpha}{\sqrt{\pi}}\sum_i q_i^2\right), \tag{2.2.40}$$

which arises directly from summing over the final term in the Madelung energy, Equation (2.2.35). Finally, the uniform background correction term is obtained by grouping all volume-dependent constant contributions, and writing the sum in terms of the total charge as

$$U^{(c)} = \frac{1}{4\pi\varepsilon_0}\frac{1}{2}\sum_{i,j}\left(-q_i q_j\frac{\pi}{\alpha^2 V}\right) = \frac{1}{4\pi\varepsilon_0}\left(-\frac{\pi}{2\alpha^2 V}\right)\left(\sum_i q_i\right)\left(\sum_j q_j\right) = \frac{1}{4\pi\varepsilon_0}\left(-\frac{\pi}{2\alpha^2 V}Q^2\right). \tag{2.2.41}$$

Here Q is the total charge of the pseudo ions, defined by Equation (3.2.8). This term is only nonzero when there is a uniform background present ($Q \neq 0$), otherwise if there is

charge neutrality across the point charges ($Q = 0$), all uniform backgrounds will cancel. Equation (2.2.41) also shows that the constant associated to the gauge fixing condition is only relevant in the case that there is an explicit uniform background present (when Q is nonzero). To compute the forces on the particles, derivatives with respect to particle positions may be taken, for which closed-form expressions are available [66].

2.3 One-component plasma models

Having established the underlying concepts for the numerical study of dense plasma using molecular dynamics (MD), this section provides a brief review of the various models that have been investigated in the literature and are suitable for MD. We begin with one-component plasma (OCP) models, which, for the purposes of this thesis, are defined as models in which only the ions are evolved dynamically. Such models may be applied to systems containing multiple ion species, effectively constituting a mixture of one-component plasmas. An example of this approach is developed in Chapter 3, where hydrogen is modelled as a mixture of atoms and ions.

In OCP-type models, the electrons are typically assumed to adiabatically adjust to the ionic motion, i.e. they employ the Born–Oppenheimer approximation. Once this approximation has been adopted, a specific model for the electronic response must be chosen. A wide range of options exists, two of which shall be reviewed in the following sections. The first is the Coulomb one-component plasma model, which treats the electrons as a uniform neutralising background. The second is the Yukawa one-component plasma model, which assumes the electrons screen the ions, hence modifying the effective particle interactions.

More general effective interparticle potentials, usually based on the wavelength-dependent dielectric response of the electrons, may be constructed to give variants of the screened OCP model [68, 69]. This model has been used for equation of state models for plasmas, e.g. Ref. [70], and to compute properties of liquid metals, where pseudo-potentials are employed to represent strongly bound core electrons [52, 71]. Finally, within the context of this thesis,

DFT-MD can be considered as an advanced OCP model, where the nonlinear electronic response is considered in a quantum-mechanical framework with an approximation for the exchange-correlation energy. The resulting electrostatic energy of this electron distribution is then used to evolve the ions, and acts as an effective many-body potential that mediates the ion-ion interactions.

2.3.1 Coulomb one-component plasma

In this model the electrons are modelled as a static uniform background, while the ions are modelled as point charges interacting through electrostatic forces. This is directly synonymous with a collection of pseudo ions, as introduced in Section 2.2.1. For a single species system of N identical charges $q = Ze$, the total charge density is [18]

$$\rho(\boldsymbol{r}_i) = \sum_i \rho_i(\boldsymbol{r}) = q\left(\sum_i^N \delta(\boldsymbol{r} - \boldsymbol{r}_i) - \frac{N}{V}\right), \tag{2.3.1}$$

with interactions given by any of the equivalent formulations derived in Section 2.2.1. Given that the Coulomb OCP is a relatively simple model, it often serves as a benchmark for strong coupling theory [72] and a reference system for advanced models [73, 74]. The Coulomb OCP model has been extensively studied through both MD and Monte Carlo methods. Starting with the seminal work of Brush, Teller, and Sahlin [18], numerous authors have investigated the equation of state [61, 75–77], transport properties (see, e.g., Refs. [78–80]), and melting properties (see, e.g., Ref. [22]).

An important feature of the Coulomb OCP is that the excess (interaction) thermodynamic properties are fully characterized by the coupling parameter Γ [18, 75]. This can be shown by transforming to units where length is dimensionless, which is chosen here to be the Wigner-Seitz radius d, and energy is measured in thermal energy k_BT. These units are referred to as OCP units. Using a bar to denote a quantity measured in these units, the following relations

may be obtained,

$$\bar{\boldsymbol{r}}_{ij} = \frac{\boldsymbol{r}_{ij}}{d} \quad ; \quad \bar{L} = \frac{L}{d} \quad ; \quad \bar{\alpha} = \alpha d \quad ; \quad \bar{\boldsymbol{k}} = \boldsymbol{k}d \quad ; \quad \bar{V} = \frac{V}{d^3} \quad ; \quad \bar{u}_{ij} = \frac{u_{ij}}{k_B T}. \tag{2.3.2}$$

Consider the full pair potential between two Coulomb OCP pseudo ions in these units,

$$\begin{aligned} \bar{u}_{ij}(\bar{\boldsymbol{r}}_{ij}) = &\frac{(Ze)^2}{4\pi\varepsilon_0 d}\frac{1}{k_B T}\Bigg(\sum_{\boldsymbol{n}\in\mathbb{Z}^3} \frac{\operatorname{erfc}\left(\bar{\alpha}\left|\bar{\boldsymbol{r}}_{ij} + \boldsymbol{n}\bar{L}\right|\right)}{\left|\bar{\boldsymbol{r}}_{ij} + \boldsymbol{n}\bar{L}\right|} \\ &+ \frac{4\pi}{\bar{V}} \sum_{\bar{\boldsymbol{k}}\neq 0} \frac{\exp\left[-\bar{k}^2/4\bar{\alpha}^2\right]}{\bar{k}^2} \exp\left[i\bar{\boldsymbol{k}}\cdot\bar{\boldsymbol{r}}_{ij}\right] - \frac{\pi}{\bar{\alpha}^2\bar{V}}\Bigg) \\ = &\,\Gamma\phi(\bar{\boldsymbol{r}}_{ij}), \end{aligned} \tag{2.3.3}$$

where the $1/d$ prefactor after the first equality arises from the unit transformation and primed quantities are transformed to the new unit system. In the second equality ϕ is a dimensionless pair potential in OCP units. Importantly, the total prefactor is simply equal to the ion-ion coupling parameter, Equation (1.1.6). Let us now consider the configurational contributions to the partition function. These take the form [75]:

$$\int_V \prod_{i,j} d^3\boldsymbol{r}_i \mathrm{d}^3\boldsymbol{r}_j \, \exp[-\beta \sum_{i,j} u_{ij}(\boldsymbol{r}_{ij})] = d^{6N} \int_{\bar{V}} \prod_{i,j} \mathrm{d}^3\bar{\boldsymbol{r}}_i d^3\bar{\boldsymbol{r}}_j \, \exp\Big[-\Gamma\,\Phi(\{\bar{\boldsymbol{r}}_i\})\Big], \tag{2.3.4}$$

where the prefactor is Wigner-Seitz radius, Equation (1.1.5), raised to the power of $6N$. From Equation (2.3.4), it is evident that the configurational statistics are controlled by a single thermodynamic parameter Γ. It follows that, with a similar treatment for the Madelung energy, the excess Helmholtz free energy in this unit system is solely a function of the coupling parameter [75]. Generally, in classical systems with separable potential and kinetic energies, the free energy separates into ideal and excess (interaction) contributions [52],

$$F = F^{\mathrm{id}} + F^{\mathrm{ex}}, \tag{2.3.5}$$

where, by linearity of derivatives, both ideal and excess parts satisfy standard thermodynamic

relations. The excess free energy, commonly expressed in intrinsic form as the Helmholtz free energy per particle, is therefore a function of coupling parameter:

$$f^{\mathrm{ex}}(\Gamma) = \frac{F^{\mathrm{ex}}}{Nk_BT}, \tag{2.3.6}$$

and hence all excess thermodynamic properties derived from it are functions of Γ alone in the thermodynamic limit. This simple dependence makes the Coulomb OCP a useful reference system in Chapter 3. Importantly, this result may be used to find a TI relation using Equation (2.1.11). Dividing Equation (2.1.12) by Nk_B and using

$$\frac{\partial\Gamma}{\partial T} = -\frac{\Gamma}{T} \tag{2.3.7}$$

to change integration variables yields

$$f = \int_0^\Gamma \frac{U^{\mathrm{ex}}}{Nk_BT}\frac{1}{\Gamma}\mathrm{d}\Gamma = \int_0^\Gamma \frac{u^{\mathrm{ex}}(\Gamma)}{\Gamma}\mathrm{d}\Gamma, \tag{2.3.8}$$

where the fact that the excess free energy is zero for $\Gamma \to 0$ in the thermodynamic limit has been used and $u^{\mathrm{ex}} = U^{\mathrm{ex}}/(Nk_BT)$ is the reduced internal energy. It is also possible to derive the equation from the statistical TI route [75]. In Chapter 3, high fidelity data for the equation of state of the Coulomb OCP are parameterised to use as a reference system in additional TI calculations.

2.3.2 Yukawa one-component plasma models

The Yukawa one-component plasma model originates from treating the electrons within the framework of linear response theory. Under certain simplifying approximations, this typically leads to a relatively simple pair potential between ions with charges q_i and q_j, which is a

function of radial separation r [68]:

$$u_{ij}(r) = \frac{q_i q_j}{4\pi\varepsilon_0} \frac{\exp(-\kappa r)}{r}, \tag{2.3.9}$$

although additional geometry and screening-dependent energy contributions arise in rigorous treatments with periodic boundary conditions, where a uniform background is present [81–83]. Note that both κ and the effective charges q_i can be rescaled to yield a more general empirical model for WDM [84], which has been applied to WDM in a variety of contexts, including as a reference system [73, 85], and to predict structural and dynamical properties when the electron–ion coupling is sufficiently weak [68, 86]. Similarly to the OCP, the excess properties of the Yukawa OCP are fully characterised by the Coulomb coupling Γ and the dimensionless inverse screening length κd, and TI expressions may be formulated for the free energy accordingly [82, 83, 87].

2.4 Two-component plasma models

In this section, we review two prominent approaches for representing dynamical electrons in molecular dynamics simulations. Perhaps surprisingly, a purely classical electron–ion plasma cannot be modelled directly with point charges. The attractive electron–ion Coulomb interaction scales as $U(r) \propto -1/r$, so at short separations the potential becomes arbitrarily deep. Under classical dynamics this drives electrons and ions toward ever smaller separations, producing unphysical tightly bound pairs. This behaviour leads to severe numerical instabilities and an ill-defined equilibrium state. To remedy this issue, one must introduce additional short-range physics that regularises the electron–ion interaction and prevents collapse. Physically, this short-range behaviour is governed by quantum mechanics, which both regularises the interaction and enables stable bound states such as atoms and molecules.

In practice, regularisation is often achieved either by incorporating quantum-diffraction effects on a statistical level through effective interaction potentials, or by adopting electron models in which the electronic degrees of freedom are represented by extended charge

distributions. The two approaches reviewed below follow these strategies respectively. In quantum statistical potentials, the short-range interaction is regularised on the lengthscale of the thermal de Broglie wavelength by using a high-temperature approximation to the two-body density matrix. The second method, WPMD, which we employ in Chapters 4 and 5, introduces explicit variables that parameterise the electronic wavefunction; at low temperatures, the kinetic-energy cost of localisation (often termed the *shape kinetic energy*) stabilises the system against collapse. Note that the shape kinetic energy, in combination with attractive Coulomb interactions (and, in a full description, exchange-correlation effects), plays a central role in the formation of electronic bound states, i.e. atomic and molecular structure.

Other TCP models also exist. For classical simulations, a common strategy is to simply replace the short-range attractive Coulomb asymptote with an effective regularised interaction at small length scales [88]. Alternatively, in the warm dense matter (WDM) regime, time-dependent density functional theory (TDDFT) can be viewed as a more advanced TCP approach: given an approximation for the time-dependent exchange-correlation potential, the electronic state is propagated in time and coupled to an ionic subsystem that is treated classically, with ions either held fixed or evolved simultaneously.

2.4.1 Quantum statistical potentials

The thermal (quantum) density matrix for two particles interacting through the Coulomb interaction may be expressed in terms of an effective interparticle interaction. A perturbative calculation in β yields the following diagonal elements for this interaction [89, 90]:

$$u_{ij}^{(K)}(\boldsymbol{r}_{ij}) = \frac{q_i q_j}{4\pi\varepsilon_0}\left\{1 - \exp\left[-\frac{\boldsymbol{r}_{ij}^2}{\Lambda_{ij}^2}\right] + \sqrt{\pi}\frac{\boldsymbol{r}_{ij}}{\gamma_{ij}\Lambda_{ij}}\operatorname{erfc}\left[\gamma_{ij}\frac{\boldsymbol{r}_{ij}}{\Lambda_{ij}}\right]\right\}, \tag{2.4.1}$$

where erfc[·] is the complementary error function, $\gamma_{ij} = 1$ is a species-dependent correction factor and the thermal de Broglie wavelength is

$$\Lambda_{ij} = \frac{\hbar}{\sqrt{2k_B T \mu_{ij}}} \quad ; \quad \frac{1}{\mu_{ij}} = \frac{1}{m_i} + \frac{1}{m_j}, \tag{2.4.2}$$

where μ_{ij} is the reduced mass. For the case that $\gamma_{ij} = 1$, Equation (2.4.1) is known as the Kelbg potential. This can be further extended to strong coupling by modifying the fitting parameter γ_{ij} at different temperatures, typically leading to the so-called improved Kelbg potential [89]. Useful approximations for $\gamma_{ij}(T)$ are presented in Ref. [89], which are used to model partially-ionised hydrogen. The ion-ion and ion-electron Kelbg interactions are plotted for a hydrogen plasma at $k_B T = 15\,\text{eV}$ in Figure 2.3, where they are compared against bare Coulomb interactions and alternative interactions derived in the following section. As can be seen, the Kelbg potential becomes finite at the origin, while agreeing with the Coulomb interaction at large separations. The small window around $r \to 0$ over which this deviation occurs is closely tied to the thermal de Broglie wavelength of the particles, which gives a statistical measure of electronic extent. Additionally, a temperature-dependent spin-resolved Pauli potential, which introduces additional short-range repulsive interactions between electrons to account for exchange effects may also be included along similar lines [89].

Effective quantum pair potentials have been employed in a wide variety of MD simulations. A small subset of the many applications includes studies of temperature relaxation [91] and dynamic properties such as plasmon dispersion [92]. More recently, quantum-statistical potential models have been extended to investigate the molecular-atomic-plasma transition in dense hydrogen [90].

2.4.2 Wave packet molecular dynamics

Here we outline the basic framework of WPMD, which is the model of choice for describing electron dynamics in the TCP simulations performed in this thesis. WPMD is directly formulated in terms of the wavefunction, and is sometimes argued to capture dynamical

features absent in quantum-statistical potential approaches [21]. A thorough discussion of the method, literature review, and derivation of the developed model is presented in Chapter 4, which includes explicit bound-state wavefunctions in the chemical picture. Therefore, a pedagogical introduction is provided here through the lens of a simpler fixed-width wavepacket model. The basic premise of WPMD is to replace the many-body wavefunction $|\Psi\rangle$ with a simpler functional form typically denoted by $|Q\rangle$. In the language of differential geometry, the space of states accessible to the system is restricted to a submanifold in the full Hilbert space. This is typically achieved by a parameterisation in terms of a set of complex parameters $\{q_\mu\}$:

$$|Q\rangle = |Q(\{q_\mu\})\rangle. \tag{2.4.3}$$

The dynamics of these complex parameters then follow from a time-dependent variational principle. A common choice is to define the following action functional

$$S = \int \mathcal{L}\mathrm{d}t \equiv \int \mathrm{d}t \langle Q| i\hbar \frac{\partial}{\partial t} - \hat{H}|Q\rangle, \tag{2.4.4}$$

where $\mathcal{L}$ is a Lagrangian defined by the state average in the final equality. Equations of motion may then be derived and the choice of parameterisation therefore determines the properties of the model. The most general case of complex parameters is rigorously presented in [93]. Although a full analysis is beyond the scope of this thesis, we note that if the parameters are constrained to be real, some parameterisations will not produce dynamics and therefore care is often needed. All parameterisations used in this thesis employ real parameters, but are chosen so that the variational principle still yields well-defined time evolution (often motivated by the corresponding complex-parameter forms). After taking the time derivative with the chain rule, the Lagrangian may be written:

$$\mathcal{L} = i\hbar \dot{q}_\mu \langle Q| \frac{\partial}{\partial q_\mu} |Q\rangle - \mathcal{H}^{\mathrm{WP}}, \tag{2.4.5}$$

where $\dot{q}_\mu$ denotes the total time derivative of the parameter and the wavepacket Hamiltonian is

$$\mathcal{H}^{\mathrm{WP}}(\{q_\mu\}) = \langle Q|\hat{H}|Q\rangle, \tag{2.4.6}$$

which is, for now, simply a function of the parameters $\{q_\mu\}$. If the parameterisation is chosen appropriately, a dynamical scheme based on generalised Hamiltonian equations will follow, something that is guaranteed for the general case of complex parameters [93]. It is well-known from variational mechanics that the path that extremises the action, Equation (2.4.4), will follow the Euler-Lagrange equations:

$$\frac{d}{dt}\frac{\partial \mathcal{L}}{\partial \dot{q}_\mu} - \frac{\partial \mathcal{L}}{\partial q_\mu} = 0, \tag{2.4.7}$$

which can therefore be used to derive equations of motion suitable for MD implementation.

In dense plasma applications, a product state of single-particle Gaussians is typically chosen. This choice neglects exchange effects (Pauli exclusion), which we approximately reintroduce using effective potentials (see Chapter 4). The many-body electron wavefunction is therefore constrained to a Hartree manifold:

$$|Q\rangle = |q_1\rangle \otimes |q_2\rangle \otimes \ldots \otimes |q_N\rangle, \tag{2.4.8}$$

where $|q_i\rangle$ is the i-th single-particle wavefunction. Additionally, the single-particle wavefunctions themselves are then restricted. Gaussian parameterisations are the predominant choice, and here we first study the simplest case of N fixed-width Gaussians with a common width parameter σ:

$$\langle \boldsymbol{x}|q_i(\boldsymbol{r}_i, \boldsymbol{p}_i)\rangle = \left(\frac{3}{4\pi\sigma^2}\right)^{3/4} \exp\left[-\frac{3}{4\sigma^2}(\boldsymbol{x}-\boldsymbol{r}_i)^2 + i\frac{\boldsymbol{p}_i}{\hbar}\cdot(\boldsymbol{x}-\boldsymbol{r}_i)\right]. \tag{2.4.9}$$

Note that the expectation value of the position operator $\hat{\boldsymbol{x}}$ is equal to the $\boldsymbol{r}_i$ parameter, and

the expectation of the momentum operator $\hat{\boldsymbol{p}}$ is equal to the $\boldsymbol{p}_i$ parameter. Mathematically:

$$\boldsymbol{p}_i = \langle q_i|\hat{\boldsymbol{p}}|q_i\rangle \quad ; \quad \boldsymbol{r}_i = \langle q_i|\hat{\boldsymbol{x}}|q_i\rangle. \tag{2.4.10}$$

Evaluating the kinetic part of the Lagrangian, the first term of Equation (2.4.5), for this state can be performed by inserting a resolution of identity. The full Lagrangian is given by

$$\begin{aligned}
\mathcal{L} &= i\hbar \sum_{\mu} \int \mathrm{d}^3\boldsymbol{x}\, \langle Q|\boldsymbol{x}\rangle \dot{q}_\mu \frac{\partial}{\partial q_\mu} \langle \boldsymbol{x}|Q\rangle - \mathcal{H}^{\mathrm{WP}} \\
&= i\hbar \sum_{i} \int \mathrm{d}^3\boldsymbol{x} \langle Q|\boldsymbol{x}\rangle \left(\dot{\boldsymbol{r}}_i \cdot \frac{\partial}{\partial \boldsymbol{r}_i} + \dot{\boldsymbol{p}}_i \cdot \frac{\partial}{\partial \boldsymbol{p}_i} \right) \langle \boldsymbol{x}|Q\rangle - \mathcal{H}^{\mathrm{WP}} \\
&= i\hbar \sum_{i} \left[\dot{\boldsymbol{r}}_i \cdot \left(\frac{3}{2\sigma^2} \langle \hat{\boldsymbol{x}} - \boldsymbol{r}_i\rangle - i\frac{\boldsymbol{p}_i}{\hbar} \right) + \dot{\boldsymbol{p}}_i \cdot \frac{i}{\hbar} \langle \hat{\boldsymbol{x}} - \boldsymbol{r}_i\rangle \right] - \mathcal{H}^{\mathrm{WP}} \\
&= \sum_{i} \dot{\boldsymbol{r}}_i \cdot \boldsymbol{p}_i - \mathcal{H}^{\mathrm{WP}},
\end{aligned} \tag{2.4.11}$$

where, in the final equality, we simplified using the expectation value relations given in Equation (2.4.10) (since $\langle \hat{\boldsymbol{x}} \rangle = \boldsymbol{r}_i$ we have $\langle \hat{\boldsymbol{x}}_i - \boldsymbol{r}_i \rangle = 0$) and the overall normalisation of the wavefunction. Interestingly, the Lagrangian is a function of all degrees of freedom, and is not limited to apparent configurational variables ($\boldsymbol{r}$ in this case). Therefore, $\mathcal{L}$ is both a *first-order* Lagrangian, meaning that it is first order in time derivatives and, in this specific case, is also a *phase-space* Lagrangian—i.e. it is a function of phase-space variables and their time derivatives. It is not a standard configurational Lagrangian of classical mechanics. Now, the Euler-Lagrange equations may be applied and yield the following Hamiltonian equations:

$$\frac{d\boldsymbol{r}_i}{dt} = \frac{\partial \mathcal{H}^{\mathrm{WP}}}{\partial \boldsymbol{p}_i} \quad ; \quad \frac{d\boldsymbol{p}_i}{dt} = -\frac{\partial \mathcal{H}^{\mathrm{WP}}}{\partial \boldsymbol{r}_i}. \tag{2.4.12}$$

Here, $\mathcal{H}^{\mathrm{WP}}$ plays the role of a classical Hamiltonian function on the phase space defined by $\{\boldsymbol{r}_i, \boldsymbol{p}_i\}$. Finally, we evaluate this Hamiltonian in terms of the parameters. Assuming the electrons interact through standard Coulomb interactions and with an ensemble of ions of

identical charge $q = Ze$, we pick the Hamiltonian operator as

$$\hat{H} = \sum_i \frac{\hat{\boldsymbol{p}}_i^2}{2m} + \frac{e^2}{4\pi\varepsilon_0} \sum_{i<j} \frac{1}{|\hat{\boldsymbol{x}}_i - \hat{\boldsymbol{x}}_j|} - \frac{Ze^2}{4\pi\varepsilon_0} \sum_{i,J} \frac{1}{|\hat{\boldsymbol{x}}_i - \boldsymbol{R}_J|}. \tag{2.4.13}$$

Here the position of the J-th ion is denoted by $\boldsymbol{R}_J$. Evaluating the state average of this with respect to the many-body restricted wavefunction yields

$$\mathcal{H}^{\mathrm{WP}} = \sum_i \left(\frac{\boldsymbol{p}_i^2}{2m} + \frac{9\hbar^2}{8m\sigma^2} \right) + \frac{e^2}{4\pi\varepsilon_0} \sum_{i<j} \frac{\operatorname{erf}\left[\sqrt{3} r_{ij}/(2\sigma)\right]}{r_{ij}} - \frac{Ze^2}{4\pi\varepsilon_0} \sum_{i,J} \frac{\operatorname{erf}\left[\sqrt{3} r_{iJ}/(\sqrt{2}\sigma)\right]}{r_{iJ}}, \tag{2.4.14}$$

where $r_{ij} = |\boldsymbol{r}_{ij}|$ is the radial separation between the expected positions of two wavepackets and $r_{iJ} = |\boldsymbol{r}_{iJ}| = |\boldsymbol{r}_i - \boldsymbol{r}_J|$ is the radial separation between an ion and the expected position of an electron. As well as the standard momentum squared contributions, the kinetic energy part now contains a second term which is typically described as the shape-kinetic energy, and related to the curvature of the wavepacket. In the schemes presented in later sections, the width of the wavepacket is dynamical, and this term causes the Gaussian wavepacket to spread as expected. For fixed-width wavepackets, it instead provides a constant energy offset. In the potential energy term, the finite extent of the charge distributions yields a non-singular electron-electron interaction. These interactions are plotted for ions of charge $Z = 1$ in Figure 2.3, where they can be compared against Kelbg and bare Coulomb interactions. The interaction is finite as $r \to 0$, and is slightly different in shape to the Kelbg potential. It also depends on the extent of the wavepacket width.

To review, by restricting the electronic wavefunction to a Hartree product of fixed-width Gaussian wavefunctions, we have obtained a model that follows classical Hamiltonian dynamics. Apart from a finite shape-kinetic energy offset, the Hamiltonian that generates these dynamics is a standard classical form. The particles interact through an error function pair potential, which is Coulomb-like at large separations and finite at short range. An additional shape-kinetic energy contribution has also been identified. When the width varies dynamically, this

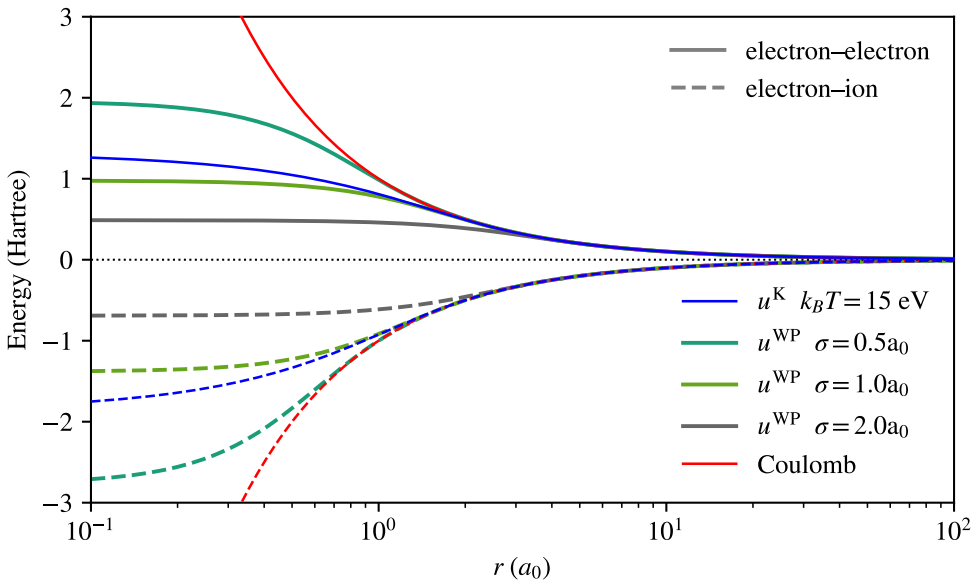

Figure 2.3: Comparison of effective electron–electron (solid lines) and electron–ion interactions (dashed lines) in atomic units. The blue curves show the Kelbg quantum statistical potential $u^{\mathrm{K}}(r)$ at $k_BT = 15\,\mathrm{eV}$. Coloured curves show the WPMD Gaussian-smeared interactions $u^{\mathrm{WP}}(r)$ for fixed widths $\sigma = \{0.5, 1, 2\}\,a_0$. The bare Coulomb limits which are proportional to $1/r$ are shown in red for reference. Distances are in Bohr radii a_0 and energies in Hartree.

energy term is large for narrow Gaussians and therefore stabilises the wavepacket against collapse.

2.5 Chapter summary

This chapter has established the theoretical and numerical framework underpinning all molecular dynamics simulations performed in this thesis. Beginning with the basic principles of classical molecular dynamics, the equations of motion, ensemble concepts, and numerical integration schemes were reviewed, with particular emphasis on the statistical interpretation of time-averaged observables and the computation of thermodynamic quantities. Thermodynamic integration was introduced as a central tool for accessing free energies from molecular dynamics data, a requirement that is fundamental to the ionisation calculations presented in later chapters.

A detailed treatment of electrostatic interactions under periodic boundary conditions was

then developed. Starting from Poisson's equation for pseudo ions, the Ewald summation technique was derived explicitly, with careful attention paid to the role of the neutralising background, gauge fixing, and the separation of real-space, reciprocal-space, and self-energy terms. This formulation provides a consistent and numerically efficient means of evaluating Coulomb interactions in bulk plasmas and forms the basis for all Coulombic interactions in this work. The connection between the formal Ewald expressions and their practical implementation in LAMMPS was also clarified.

Building on this foundation, a systematic overview of molecular dynamics models for dense and partially-ionised plasmas was presented. One-component plasma models were introduced first, including both the Coulomb OCP and Yukawa-type screened interactions. The Coulomb OCP was highlighted as a particularly important reference system, whose excess thermodynamic properties are fully characterised by the coupling parameter Γ. This property enables accurate thermodynamic integration strategies and motivates its use as a benchmark and reference model in Chapter 3. Yukawa OCP models were then discussed as extensions that incorporate electronic screening within linear-response theory.

Finally, two-component plasma models with explicit electronic degrees of freedom were reviewed. The necessity of regularising the classical electron–ion interaction was discussed, motivating the introduction of quantum statistical potentials and WPMD. Quantum statistical potentials were shown to provide an effective, temperature-dependent regularisation of short-range interactions, while WPMD was introduced as a variational, wavefunction-based approach that naturally incorporates quantum diffraction and stabilises bound states through shape kinetic energy. A pedagogical derivation of fixed-width Gaussian WPMD was provided, illustrating how classical Hamiltonian dynamics emerge from a constrained variational principle and how non-singular effective interactions arise.

Together, the material presented in this chapter provides the conceptual and technical foundation for the models developed and applied in the remainder of the thesis. The one-component plasma framework and free-energy techniques introduced here underpin the ionisation calculations in Chapter 3, while the WPMD formalism forms the basis for the

extended bound-state models and statistical analyses presented in Chapters 4 and 5.

Chapter 3

Ionisation calculations using classical molecular dynamics

In this chapter, the ionisation state is computed self-consistently for two OCP-inspired models designed for molecular dynamics simulations. The resulting ionisation behaviour is then analysed in the context of ionisation potential depression and pressure ionisation.

The chapter is structured as follows: First, the concept of the chemical picture is introduced and used to derive the Saha equation. The link between free energy and ionisation potential depression is also explained. Two models suitable for partially-ionised hydrogen are then presented, and expressions for the corresponding Coulomb interactions are derived. To determine the model-dependent ionisation state, a free-energy minimisation framework is developed, which incorporates the TI technique. Simulation results for the ionisation state are subsequently presented, alongside comparisons with approximate models for the free energy. Finally, possible future developments are outlined, including the possible inclusion of electronic screening into partially-ionised OCP models and extension to higher atomic number elements.

3.1 The chemical picture

The chemical picture provides a framework for describing partially-ionised matter in terms of a mixture of distinct species, such as neutral atoms, ions of various charge states, and free electrons [94]. In this approach, bound and free electronic states are treated as separate constituents, with corresponding ionisation and recombination processes. This may be contrasted with the physical picture, which avoids this explicit separation, often leading to greater computational cost [21]. Both DFT and PIMC approaches are based on the physical picture.

For the purposes of this thesis, it is sufficient to consider a hydrogenic plasma which is composed of neutrals (or atoms), ions, and free electrons. It is, of course, possible to generalise these arguments to other materials [95], and to molecule formation at lower temperatures [96,

97]. The chemical process may be represented schematically by the reaction:

$$\mathrm{H} \rightleftharpoons \mathrm{H}^{+} + e^{-}, \tag{3.1.1}$$

which represents the competing processes of ionisation and recombination in a plasma. Now consider an ideal, chemically reacting gas of these three species. Since the particles are not interacting, their partition functions factorise, and therefore their free energies combine linearly. The total ideal free energy is therefore the sum of contributions from ions (i), electrons (e) and neutrals (n):

$$F_{\mathrm{id}} = F_{\mathrm{id}}^{(i)} + F_{\mathrm{id}}^{(e)} + F_{\mathrm{id}}^{(n)}. \tag{3.1.2}$$

We use the well-known formula for the free energy of an ideal gas of particles of species α [98] contained within a region of volume V. Each species has classical kinetic degrees of freedom, and a set of internal energy states denoted by ϵ_k:

$$\frac{F_{\mathrm{id}}^{(\alpha)}}{N_\alpha k_B T} = -\log\left[\frac{V}{N_\alpha \Lambda_\alpha^3}\right] - 1 - \log\left[\sum_k \exp\left(-\frac{\epsilon_k}{k_B T}\right)\right]. \tag{3.1.3}$$

Here N_α is the number of particles of the α species and Λ_α is the thermal de Broglie wavelength, defined by Equation (2.4.2)—here the subscript now represents the species of the particle. The ions have one internal energy state, which is set to zero ($\epsilon_1 = 0$); each free electron has two degenerate spin states ($\epsilon_1 = 0, \epsilon_2 = 0$); while each bound electron within a neutral atom is assumed to occupy a spin-degenerate ground state in the hydrogen atom: ($\epsilon_1 \approx -E_B^H$, $\epsilon_2 \approx -E_B^H$), given in Equation (1.2.1).

The partially-ionised plasma is globally charge neutral $N_i = N_e$ and the total proton (or electron) number $N = N_i + N_n$ is conserved. It is possible to express the total ideal free energy directly in terms of the ionisation state $\bar{z} = N_i/N$ and number density $n = N/V$. Note that for more advanced models, an ensemble of different ionisation states (or charge states) and species fractions would be similarly defined. Returning to the case studied here,

on dividing Equation (3.1.3) by Nk_BT, the classical *reduced* ideal free energy is defined as

$$f_{\rm id}(n,T,\bar{z}) \equiv \frac{F_{\rm id}}{Nk_BT} = f_{\rm id}^{(i)} + f_{\rm id}^{(e)} + f_{\rm id}^{(n)}. \tag{3.1.4}$$

The contribution from each chemical species takes the following form:

$$f_{\rm id}^{(i)} = \bar{z}\log\left[\bar{z}n\Lambda_i^3\right] - \bar{z} \tag{3.1.5}$$

$$f_{\rm id}^{(e)} = \bar{z}\log\left[\frac{1}{2}\bar{z}n\Lambda_e^3\right] - \bar{z} \tag{3.1.6}$$

$$f_{\rm id}^{(n)} = (1-\bar{z})\log\left[\frac{1}{2}(1-\bar{z})n\Lambda_n^3\right] - (1-\bar{z})\frac{E_B^H}{k_BT} - (1-\bar{z}). \tag{3.1.7}$$

A remarkable feature of the chemical picture is that the charge state distribution may be obtained without appealing to the underlying microscopic mechanisms that describe ionisation and recombination processes. In thermal equilibrium, the free energy is minimised, i.e. the reduced total free energy $f = F/(Nk_BT)$ satisfies the condition

$$\frac{\partial f}{\partial \bar{z}} = 0. \tag{3.1.8}$$

This is equivalent to equating the chemical potentials of different species using $(\partial F/\partial N_\alpha)_{T,V} = \mu_\alpha$. The derivative of the reduced ideal free energy is

$$\frac{\partial f_{\rm id}}{\partial \bar{z}} = \log\left[\bar{z}n\Lambda_i^3\right] + \log\left[\frac{1}{2}\bar{z}n\Lambda_e^3\right] - \log\left[\frac{1}{2}(1-\bar{z})n\Lambda_n^3\right] + \frac{E_B^H}{k_BT} = 0, \tag{3.1.9}$$

which can be re-arranged into a common form of the hydrogenic Saha Equation [94]:

$$\frac{\bar{z}^2}{1-\bar{z}} = \frac{1}{n}\left(\frac{\Lambda_n}{\Lambda_i\Lambda_e}\right)^3 \exp\left(-\frac{E_B^H}{k_BT}\right) \approx \frac{1}{\Lambda_e^3 n}\exp\left(-\frac{E_B^H}{k_BT}\right). \tag{3.1.10}$$

This equation is quadratic in $\bar{z}$ and therefore admits a closed-form solution. For more sophisticated models, the corresponding Saha equation (or set of coupled Saha equations in the case of more than 3 species) may be numerically solved. In this thesis, a direct numerical

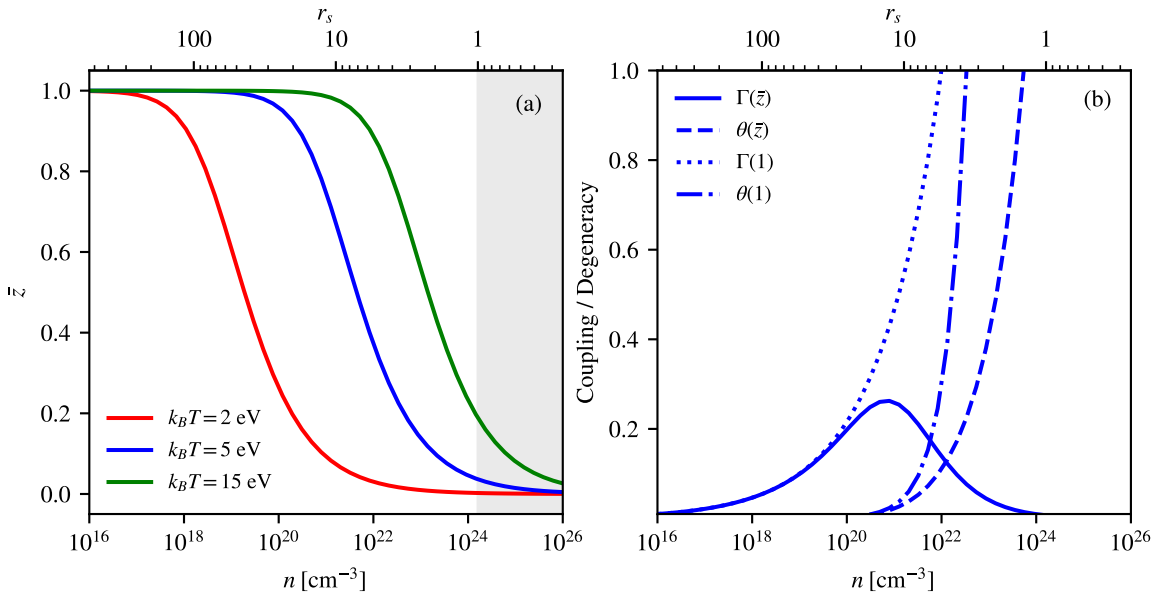

Figure 3.1: (a) Ionisation state $\bar{z}$ as a function of number density n for partially-ionised hydrogen at temperatures $k_BT = \{2, 5, 15\}$ eV. The shaded region indicates where the inter-particle spacing is smaller than the Bohr radius $r_s < 1$. (b) Coupling and degeneracy parameter at $k_BT = \{5\}$ eV. The result is shown using the ionisation state from panel (a) and using a fully ionised system.

minimisation of the free energy is instead performed, which naturally extends to the case where MD simulations are employed. The result of such a calculation is plotted, for three distinct temperatures, as a function of density in Figure 3.1.

The results of this figure may be contextualised in terms of the total free energy of the system in Equations (3.1.4) to (3.1.7). At fixed density, the temperature dependence arises primarily through the binding-energy term in the neutral free-energy contribution, $E_B^H/(k_BT)$. At low temperatures, this term provides a large negative contribution to the free energy for states with a high neutral fraction, resulting in a minimum of the total free energy at small values of $\bar{z}$. As the temperature is increased, the magnitude of this contribution is reduced, diminishing the impact of the bound electrons on the equilibrium ionisation state. When this term is sufficiently negligible, the system may maximise its entropy by splitting into a mixture of two species. Therefore, the translational entropy terms become increasingly significant at higher temperatures, shifting the free-energy minimum towards larger values of $\bar{z}$. This tradeoff between statistical entropy and binding energy explains why ionisation effects occur

at lower temperatures than $T \sim E_B^H/k_B$ for dilute plasmas.

At fixed temperature, the density dependence is controlled by the translational part of the ideal free energy. For each species α, the reduced free energy contains a term proportional to $\log(n_\alpha \Lambda_\alpha^3)$. This dependence follows from the translational partition function $\sim V/\Lambda_\alpha^3$, which is obtained by integrating over the classical single-particle phase space and assigning one quantum state to each cell of volume h^3, where h is Planck's constant. For a particle of species α, the number of translational states in a phase-space element is therefore $d^3r\, d^3p/h^3$. Integration over position gives the factor of V, while the momentum integral yields a factor proportional to $1/\Lambda_\alpha^3$. The quantity $n_\alpha \Lambda_\alpha^3 = N_\alpha/(V/\Lambda_\alpha^3)$ may therefore be interpreted as the occupancy of the available translational states. As the density increases, this occupancy increases and the translational entropy decreases. Because ionisation converts one neutral atom into two free particles, the translational entropy penalty is greater for states with larger $\bar{z}$. Consequently, increasing density favours less ionised configurations, and the free-energy minimum shifts towards smaller values of $\bar{z}$.

Taken together, these effects explain the trends observed in Figure 3.1(a). Increasing temperature reduces the energetic stabilisation of bound states and favours ionisation, while increasing density enhances the entropic cost associated with multiple free particles and favours recombination. In Figure 3.1(b), the (ion or electron) coupling and electron degeneracy parameters are plotted, both using the effective ionisation state of the model and assuming the system is fully ionised. These values are calculated for a temperature corresponding to $k_B T = 5\,\mathrm{eV}$. Interaction and quantum effects, which are neglected within the free-energy model, will influence the result at high densities.

Let us now assume there is an excess contribution to the free energy due to interactions. The total reduced free energy may then be written

$$f \equiv \frac{F}{N k_B T} = f_{\mathrm{id}} + f_{\mathrm{ex}}, \tag{3.1.11}$$

where $f_{\mathrm{ex}} = F_{\mathrm{ex}}/(N k_B T)$ is the reduced excess free energy, accounting for interaction effects

beyond the ideal-gas approximation. In addition, the ideal free energy of the electrons must be modified to account for quantum statistics. In particular, deviations from classical behaviour arising from Fermi–Dirac statistics may be incorporated through a quantum correction Δf. The full ideal free energy of the electrons is therefore written as

$$f^{(e)}_{\mathrm{id,quantum}} = f^{(e)}_{\mathrm{id}} + \Delta f, \tag{3.1.12}$$

where Δf depends on the degree of electron degeneracy and is discussed in detail in Section 3.3.2.

Imposing the minimisation condition, Equation (3.1.8), the Saha equation now takes the form:

$$\frac{\bar{z}^2}{1-\bar{z}} = \frac{1}{n}\left(\frac{\Lambda_n}{\Lambda_i\Lambda_e}\right)^3 \exp\left(-\frac{E_B^H + \Delta I + \Delta\mu_e}{k_B T}\right). \tag{3.1.13}$$

Here the ionisation potential is given by any of the following equivalent expressions:

$$\Delta I = k_B T \frac{\partial f_{\mathrm{ex}}}{\partial \bar{z}} = \frac{\partial F_{\mathrm{ex}}}{\partial N_e} = \frac{\partial F_{\mathrm{ex}}}{\partial N_i}. \tag{3.1.14}$$

Meanwhile, the electron chemical potential correction is given by

$$\Delta\mu_e = k_B T \frac{\partial(\Delta f)}{\partial \bar{z}}, \tag{3.1.15}$$

and satisfies

$$\mu_e = k_B T \log\left(\frac{\bar{z} n \Lambda_e^3}{2}\right) + \Delta\mu_e, \tag{3.1.16}$$

where μ_e is the total free electron chemical potential. Inspecting Equation (3.1.13), it becomes clear that the effect of these excess and quantum corrections can be characterised by the ionisation potential being shifted. The total effective ionisation potential may therefore be defined as

$$I = E_B^H + \Delta I + \Delta\mu_e. \tag{3.1.17}$$

As further elaborated in the remaining chapter, ΔI typically decreases the effective ionisation energy, while quantum corrections will increase the chemical potential of free electrons, therefore increasing the effective ionisation energy. In the ideal ($\Gamma \ll 1$) and nondegenerate ($\theta \gg 1$) limits, $f_{\text{ex}} = \Delta\mu_e = 0$, and the ideal case is recovered.

Generally, the chemical picture is particularly useful at low to moderate densities, where individual bound states remain well defined, and forms the basis of classical descriptions of ionisation equilibrium such as the Saha equation. At higher densities, however, the interactions between bound and free states become relevant, motivating careful extensions of the framework. The remainder of this chapter examines how such an extension can be performed for Molecular Dynamics applications, where strong coupling may be treated exactly on a classical level. In doing so, we investigate different models for the interaction free energy f_{ex} of the system, and their effect on the equilibrium ionisation state. A primary outcome of this chapter is therefore the development of an MD framework capable of computing the self-consistent ionisation state of a given model.

3.2 Hydrogen models

A partially-ionised, charge-neutral Coulomb system is considered. A total of N electrons and an equal number of protons are placed inside a cubic box of volume $V = L^3$, which is subject to periodic boundary conditions. To model bound electronic states, a chemical picture is employed, in which free electrons form a uniform background charge, while each bound electron is spatially localised on a specific ion. The system may therefore be partitioned into N_i ions and N_n neutrals, such that $N = N_i + N_n$. The neutral mass $m_n = m_i + m_e$ is the sum of electron and ion masses. The particles interact through a potential energy function $\mathcal{U}^{(\text{MD})}$, which depends on the instantaneous configuration of the particles and determines the interactions within the system. Modifications to this function serve as the central object for the thermodynamic integration procedure described in Section 3.3.1. The Hamiltonian that

determines the dynamics is

$$\mathcal{H}^{(\mathrm{MD})} = \sum_j \frac{\boldsymbol{p}_j^2}{2m_j} + \mathcal{U}^{(\mathrm{MD})} \tag{3.2.1}$$

where the sum is over all heavy particles (ions and neutrals). In the following subsections, the potentials used to model the particle interactions, and hence build $\mathcal{U}^{(\mathrm{MD})}$, are introduced.

It should be noted that no electronic kinetic-energy terms or internal states arise explicitly in Equation (3.2.1). This reflects the modelling assumption that free electrons form a uniform background charge, while bound electrons are assumed fixed to their respective protons. Nevertheless, these effects are accounted for in the ideal free energy, as discussed in the previous section. To make this explicit, following Ref. [82], the total Hamiltonian of the system is written as

$$\mathcal{H} = \mathcal{H}^{(\mathrm{MD})} + F_{\mathrm{id}}^{\text{non-dyn}}, \tag{3.2.2}$$

where $F_{\mathrm{id}}^{\text{non-dyn}}$ is the ideal free energy associated with the non-dynamical degrees of freedom[1]. Contributions from both bound and free electrons are included in this term and are specified in Section 3.3.2. The Helmholtz free energy may then be written as the sum of two terms:

$$F = F_{\mathrm{id}}^{\text{non-dyn}} + F^{(\mathrm{MD})} = F_{\mathrm{id}}^{\text{non-dyn}} - k_B T \log Z^{(\mathrm{MD})}, \tag{3.2.3}$$

where the partition function that describes the explicit dynamical degrees of freedom $Z^{(\mathrm{MD})}$ takes the standard definition of

$$Z^{(\mathrm{MD})} = \frac{1}{h^{3N} N!} \int \prod_j^N \mathrm{d}^3\boldsymbol{r}_j d^3\boldsymbol{p}_j \exp\left[-\beta \mathcal{H}^{(\mathrm{MD})}\right]. \tag{3.2.4}$$

3.2.1 Bound-state Coulomb model

In the first model considered, which is referred to as the bound-state Coulomb (BSC) model, each bound electron is modelled as a frozen single-particle wavefunction. A natural choice is

1. Here, non-dynamical refers to the fact that these degrees of freedom are not explicitly represented within the MD simulations.

the ground state of an isolated hydrogen atom,

$$\psi_{1\mathrm{s}}(\boldsymbol{r}) = \frac{1}{\sqrt{a_0^3\pi}} \exp\left(-\frac{r}{a_0}\right), \tag{3.2.5}$$

which is defined up to an unneeded phase and $r = |\boldsymbol{r}|$. A neutral particle is configured by superposing the electron onto an ion at position $\boldsymbol{r}_l$. In periodic boundary conditions, the charge density of a neutral (n) particle may therefore be written as

$$\rho^{(n)}_{l,\mathrm{per}}(\boldsymbol{r}) = e\left[\sum_{\boldsymbol{n}\in\mathbb{Z}^3} \delta^3(\boldsymbol{r} - \boldsymbol{r}_l + \boldsymbol{n}L) - \sum_{\boldsymbol{n}\in\mathbb{Z}^3} |\psi_{1\mathrm{s}}(\boldsymbol{r} - \boldsymbol{r}_l + \boldsymbol{n}L)|^2\right], \tag{3.2.6}$$

where periodic boundary conditions have been imposed through a sum over lattice vectors. Alternatively, in the case that the atom is ionised, an ion at position $\boldsymbol{r}_k$ and corresponding free electron can be combined to give the charge density of a pseudo ion. In the BSC model, the free electrons are assumed to be uniformly distributed throughout the system. The charge density is therefore equivalent to the OCP pseudo ion as defined in Chapter 2:

$$\rho^{(i)}_k(\boldsymbol{r}) = e\left[\delta^3(\boldsymbol{r} - \boldsymbol{r}_k) - \frac{1}{V}\right]. \tag{3.2.7}$$

The charge of the pseudo ion is identical to an ion in the Coulomb OCP model [18], and therefore the BSC model may be interpreted as a natural extension to partially-ionised systems. Note that a sum over periodic lattice vectors is included explicitly in the neutral-particle density, Equation (3.2.6), to account for contributions to the charge density within the central simulation cell arising from periodic images of the spatially extended 1s wavefunction. Such a sum is unnecessary for the pseudo ion, as its delta-function charge distribution is localised, and the uniform background charge is global (not periodically replicated).

In a similar style to the OCP, the interactions are written in terms of the pseudo ion and neutral charge densities, such that the electron background acts to modify the inter-particle pair potentials. In this section, the system is therefore considered to be composed of N_n neutrals and N_i pseudo ions with charge distributions given by Equations (3.2.6) and (3.2.7)

respectively. The total charge density due to particles in the central box is

$$\rho_{\text{total}}(\boldsymbol{r}) = \sum_{k}^{N_i} \rho_k^{(i)}(\boldsymbol{r}) + \sum_{l}^{N_n} \rho_l^{(n)}(\boldsymbol{r}). \tag{3.2.8}$$

To compute the electrostatic potential ϕ of the system, Poisson's equation,

$$\nabla^2 \phi(\boldsymbol{r}) = -\frac{\rho(\boldsymbol{r})}{\varepsilon_0}, \tag{3.2.9}$$

is solved for these charge distributions. Exploiting the linearity, the problem may be reduced to computing the electrostatic potential induced by the neutral and ion charge distributions, Equations (3.2.6) and (3.2.7) respectively.

First, the potential generated by a neutral particle in open (non-periodic) space is considered. By leveraging spherical symmetry and writing the Laplacian operator in spherical coordinates, the potential $\phi_l^{(n)}(\boldsymbol{r})$ generated at a distance $r = |\boldsymbol{r}_l - \boldsymbol{r}|$ from a given neutral particle is

$$\frac{1}{r^2}\frac{\partial}{\partial r}\left(r^2 \frac{\partial \phi_l^{(n)}}{\partial r}\right) = -\frac{1}{\varepsilon_0}\rho_l^{(n)}(r). \tag{3.2.10}$$

This may be solved by integrating with respect to the radial coordinate over all space. The final result is

$$\phi_l^{(n)}(r) = \frac{e}{4\pi\varepsilon_0}\left[\frac{\exp(-2r/a_0)}{r}\left(1 + \frac{r}{a_0}\right) + \frac{\mathcal{C}_1}{r}\right] + \mathcal{C}_2, \tag{3.2.11}$$

where the integration constants, $\mathcal{C}_1$ and $\mathcal{C}_2$ remain to be specified. The asymptotic behaviour of the potential near the central proton gives the following condition:

$$\lim_{r\to 0} 4\pi r^2 \frac{d\phi_l^{(n)}}{dr} = -\frac{e}{\varepsilon_0} \tag{3.2.12}$$

which is satisfied for $\mathcal{C}_1 = 0$. In open space, the electrostatic potential should vanish at infinity and $\mathcal{C}_2$ may be set to zero. However, in periodic boundary conditions, this is not necessarily

the case. Using the open-space result, the full periodic potential may be written:

$$\phi^{(n)}_{l,\mathrm{per}}(\boldsymbol{r}) = \frac{e}{4\pi\varepsilon_0}\left[\sum_{\boldsymbol{n}} \frac{\exp(-2r_{\boldsymbol{n}}/a_0)}{r_{\boldsymbol{n}}}\left(1+\frac{r_{\boldsymbol{n}}}{a_0}\right)\right] + \mathcal{C}_3, \tag{3.2.13}$$

where $r_{\boldsymbol{n}} = |\boldsymbol{r} - \boldsymbol{r}_l + \boldsymbol{n}L|$ and $\mathcal{C}_3$ is an unspecified constant. Let us now impose the gauge condition, Equation (2.2.10), to the electrostatic potential generated by a neutral particle. In a similar vein to the calculation presented in Section 2.2.1, after replacing periodic summation with an integral over all space, we arrive at

$$\mathcal{C}_3 = -\frac{e}{4\pi\varepsilon_0}\frac{1}{V}\int_{\mathbb{R}^3} \mathrm{d}^3 r \frac{\exp(-2r/a_0)}{r}\left(1+\frac{r}{a_0}\right) = -\frac{e}{4\pi\varepsilon_0}\frac{2\pi a_0^2}{V}. \tag{3.2.14}$$

Therefore the electrostatic potential of a neutral particle under the chosen gauge is

$$\phi^{(n)}_{l,\mathrm{per}}(\boldsymbol{r}) = \frac{e}{4\pi\varepsilon_0}\left(\sum_{\boldsymbol{n}} \frac{\exp(-2r_{\boldsymbol{n}}/a_0)}{r_{\boldsymbol{n}}}\left(1+\frac{r_{\boldsymbol{n}}}{a_0}\right) - \frac{2\pi a_0^2}{V}\right). \tag{3.2.15}$$

The Coulomb interaction energy may now be computed. The total neutral-neutral (nn) interaction is the following sum over pairs:

$$U^{(nn)} = \sum_{l<m}\int_V \rho^{(n)}_{l,\mathrm{per}}\,\phi^{(n)}_{m,\mathrm{per}}\mathrm{d}^3\boldsymbol{r} = \sum_{l<m} u^{(nn)}_{l,m}, \tag{3.2.16}$$

where the pair potential $u^{(nn)}_{l,m}$ has been defined. This integral, which may be decomposed into proton-proton, proton-bound and bound-bound contributions,

$$u^{(nn)}_{l,m} = \frac{e^2}{4\pi\varepsilon_0}\sum_{\boldsymbol{n}} \frac{\exp(-2r_{lm,\boldsymbol{n}}/a_0)}{r_{lm,\boldsymbol{n}}}\left[1+\frac{5}{8}\left(\frac{r_{lm,\boldsymbol{n}}}{a_0}\right) - \frac{3}{4}\left(\frac{r_{lm,\boldsymbol{n}}}{a_0}\right)^2 - \frac{1}{6}\left(\frac{r_{lm,\boldsymbol{n}}}{a_0}\right)^3\right], \tag{3.2.17}$$

where $r_{lm,\boldsymbol{n}} = |\boldsymbol{r}_l - \boldsymbol{r}_m + \boldsymbol{n}L|$ is the periodically replicated pairwise separation between neutral particles. Note that the neutral self energy should be calculated using quantum mechanics, and is incorporated directly into the free energy as an internal energy state. The

(pseudo) ion-neutral (in) interaction energy is

$$U^{(in)} = \sum_{k,l} \int_V \rho_k^{(i)} \, \phi_{l,\mathrm{per}}^{(n)} \mathrm{d}^3\boldsymbol{r} = \sum_{k,l} u_{l,m}^{(in)}. \tag{3.2.18}$$

The ion-neutral pair potential is therefore

$$u_{l,m}^{(in)} = \frac{e^2}{4\pi\varepsilon_0} \left(\sum_{\boldsymbol{n}} \frac{\exp(-2r_{lm,\boldsymbol{n}}/a_0)}{r_{lm,\boldsymbol{n}}} \left(1 + \frac{r_{lm,\boldsymbol{n}}}{a_0}\right) - \frac{2\pi a_0^2}{V} \right), \tag{3.2.19}$$

which directly follows from the periodic neutral potential and charge neutrality of the pseudo ion.

The interaction energies written above correspond to the total energy of the ion-neutral and neutral-neutral interactions. The actual expressions implemented into LAMMPS, which are exact reformulations of the above expressions, are the following pair potential between particles in the central box and periodic images:

$$u_{\mathrm{pair}}^{(in)}(r) = \frac{e^2}{4\pi\varepsilon_0} \frac{\exp(-2r/a_0)}{r} \left[1 + \left(\frac{r}{a_0}\right)\right], \tag{3.2.20}$$

$$u_{\mathrm{pair}}^{(nn)}(r) = \frac{e^2}{4\pi\varepsilon_0} \frac{\exp(-2r/a_0)}{r} \left[1 + \frac{5}{8}\left(\frac{r}{a_0}\right) - \frac{3}{4}\left(\frac{r}{a_0}\right)^2 - \frac{1}{6}\left(\frac{r}{a_0}\right)^3\right]. \tag{3.2.21}$$

These potentials resemble those used in Ref. [99], and the neutral interactions are screened on the length scale of the bound states, as expected. There is also a volume-dependent contribution which arises from the gauge fixing requirements:

$$U_0^{(in)} = -\frac{e^2}{4\pi\varepsilon_0} \frac{2\pi N_i N_n a_0^2}{V}. \tag{3.2.22}$$

This additional energy term is not configuration-dependent and is therefore simply included as a post-processing step throughout this chapter.

The remaining energy component $U^{(ii)}$ corresponds to the pseudo ion interactions, which form a one-component plasma (OCP) subsystem and can be similarly decomposed as pair

and constant terms [18, 100, 101]. The full interaction energy of the pseudo-ions is given in this thesis in Equation (2.2.32) and fully accounts for the ion-background and background-background contributions of the model [18]. Generally, the presence of the uniform free electron background provides a regularisation to the ion-ion interactions, which would otherwise formally diverge under periodic boundary conditions.

Additionally, constant energy terms that do not affect the dynamics but do depend on the number of particles appear due to gauge-fixing requirements. These terms are particularly relevant for comparing free energies at different ionisation states and only occur when there is an electron background, which corresponds to the condition $N_i \neq 0$. In a similar vein, electron background energy contributions have recently been discussed in the context of phase diagram calculations, where volume- and particle-number-dependent energy terms are also relevant [102].

To conclude the introduction of the BSC model, the total system energy may be written as the sum of the three distinct energy contributions:

$$\mathcal{U}^{(\mathrm{BSC})} = U^{(ii)} + U^{(in)} + U^{(nn)}. \tag{3.2.23}$$

In this chapter, to produce a scheme for efficient free energy calculation, these separate energy contributions may be independently scaled through the introduction of TI coupling parameters.

3.2.2 Short-range repulsion model

In plasma models formulated within the chemical picture, hard sphere potentials are often used, either as a reference potential with known properties, e.g. [70] or directly, e.g. [103]. The justification of this second class of potentials is left to Section 3.4.4. To investigate an analogous effect, we introduce a second model involving a short-range repulsion (SRR) between neutral particles, noting that similar potentials have been previously introduced to model bound electron repulsion effects for partially-ionised plasmas [84, 104]. A third

potential,

$$u^{(nn)}_{\text{pair,SRR}}(r) = \mathcal{A}\left(\frac{1}{r}\right)^{12}, \tag{3.2.24}$$

is introduced in combination with the BSC model and acts solely between neutral pairs. In Equation (3.2.24), $\mathcal{A}$ is the overall constant determining the strength of the interaction and is set by equating $U^{\text{nn}}_{\text{SRR}}(2r_*) = (3/2)k_BT$, to give an effective radius r_*. The total energy due to SRR interactions is

$$U^{(nn)}_{\text{SRR}} = \sum_{l<m} {\sum_{\boldsymbol{n}}}' u^{(nn)}_{\text{pair,SRR}}(|\boldsymbol{r}_l - \boldsymbol{r}_m + \boldsymbol{n}L|), \tag{3.2.25}$$

where the sum runs over all pairs of neutral particles in the central box and over non-zero integer vectors (denoted by the primed summation). The total energy in the SRR model is therefore

$$\mathcal{U}^{(\text{SRR})} = \mathcal{U}^{(\text{BSC})} + U^{(nn)}_{\text{SRR}}. \tag{3.2.26}$$

The potentials discussed thus far have been implemented as a new pair style into the LAMMPS codebase [59], in which all subsequent simulations are performed. Having defined the two hydrogen models, the ionisation calculation methodology will now be introduced.

3.3 Free Energy Minimisation Framework

In any model which distinguishes between bound and free electrons, the ionisation state is a key quantity of interest. In hydrogenic systems, the ionisation state takes a particularly simple form as the ratio of the number of ions to the total number of electrons $\bar{z} = N_{\text{i}}/N$. A system in thermodynamic equilibrium and held at constant density $n = N/V$ and temperature T will exhibit a minimum in the Helmholtz free energy:

$$\left(\frac{\partial f}{\partial \bar{z}}\right)_{n,T} = 0. \tag{3.3.1}$$

Equation (3.3.1) is valid under the constraint of charge neutrality and the reduced free energy per particle is $f = F/Nk_BT$. The ionisation state may therefore be found by computing the free energy across a set of artificial ionisation states, and performing a minimisation procedure. These considerations apply to any chemical picture of hydrogen, and are readily generalisable to heavier elements [94, 95, 105], where different charge states will be present. To the best of the author's knowledge, this approach has not been employed in MD applications where, given a set of interparticle potentials, the effect of strong coupling can be treated exactly. The methodology to compute the free energy is detailed in the following section.

3.3.1 Thermodynamic integration

The Helmholtz free energy depends on the accessible volume of the underlying phase space, and is not directly accessible in MD simulations. For this reason, we have performed a multistep TI to compute the free energy across different ionisation states [50]. A coupling vector $\vec{\lambda}$ may be introduced into the MD potential,

$$\mathcal{U}^{(\mathrm{MD})} \to \mathcal{U}^{(\mathrm{MD})}(\vec{\lambda}) \tag{3.3.2}$$

in a currently unspecified manner. Two important cases are imposed: When the coupling vector is the null vector, $\vec{\lambda} = \vec{0}$, the system is noninteracting (ideal) and when the coupling vector is the unit vector, $\vec{\lambda} = \vec{1}$, the interactions match those of the model i.e. the interactions of the *target* system. The introduction of coupling parameters allows the excess free energy to be written as an integral over ensemble averages evaluated over different coupling strengths [50]:

$$f^{\mathrm{ex}}(n, T, \bar{z}) = \frac{1}{Nk_BT} \int_{\vec{0}}^{\vec{1}} \mathrm{d}\vec{\lambda} \cdot \left\langle \frac{\partial \mathcal{U}^{(\mathrm{MD})}(\vec{\lambda})}{\partial \vec{\lambda}} \right\rangle_{\vec{\lambda}}. \tag{3.3.3}$$

The notation $\langle \cdot \rangle_{\vec{\lambda}}$ denotes an ensemble average computed for a system at the given coupling vector. In the context of MD, this consists of evaluating time averages over trajectories generated by the Hamiltonian of the system with the potential interactions modified by the

coupling vector. Given these trajectories, the components of the vector defined by $\partial\mathcal{H}/\partial\vec{\lambda}$ may be evaluated over them. Therefore, a set of simulations is required to numerically evaluate the integral for each ionisation state. Given that Equation (3.3.3) computes the excess free energy for a set of particle interactions, the ideal free energy of the model is required as input for the calculation.

3.3.2 Ideal free energy

The reduced ideal free energy $f_{\text{id}} = F_{\text{id}}/(Nk_BT)$ is discussed in Section 3.1. In reduced form, Equation (3.2.3) may be written

$$f^{\text{id}} = f_{\text{id}}^{(\text{MD})} + f_{\text{id}}^{\text{non-dyn}}. \tag{3.3.4}$$

This comprises the dynamical ideal free energy contributions which are explicitly present within the MD model $f_{\text{id}}^{(\text{MD})}$ and the non-dynamical contributions $f_{\text{id}}^{\text{non-dyn}}$ which are composed of both bound and free electron parts. In line with the BSC model and the discussion in Section 3.1, each hydrogen atom is in its spin-degenerate ground state with internal binding energy $E_B^H \approx 13.59$ eV derived from quantum-mechanical considerations. This energy is the sum of the Coulomb interaction energy and kinetic energy terms of the 1s wavefunction and ion pair. Free electrons have free energy denoted by $f_{\text{id,quantum}}^{(e)}$, giving a non-dynamical contribution of

$$f_{\text{non-dyn}}^{\text{id}} = -\bar{x}\frac{E_B^H}{k_BT} + f_{\text{id,quantum}}^{(e)}, \tag{3.3.5}$$

where $\bar{x} = 1 - \bar{z}$ is the neutral fraction. Since the ideal system is noninteracting, the MD contributions to the free energy correspond to the translational contributions discussed in Section 3.1:

$$f_{\text{id}}^{(\text{MD})}(n, T, \bar{z}) = \bar{z}\log\left[\bar{z}n\Lambda_i^3\right] - \bar{z} + \bar{x}\log\left[\frac{1}{2}\bar{x}n\Lambda_n^3\right] - \bar{x}. \tag{3.3.6}$$

Note that, if the classical formula for the ideal free energy of the electrons is used, the sum of the MD contribution and the non-dynamical ideal term reproduces the ideal free energy

given in Equation (3.1.4), as expected.

Within the two OCP-inspired models, the electrons are assumed to form a uniform background. Therefore, the most appropriate model is an ideal Fermi gas. The free energy may be derived from quantum-statistical calculations in the grand canonical ensemble [23]. The key results are summarised here. The electrons are non-interacting and contained within a large box. It is assumed they follow a continuous Fermi–Dirac distribution over energy states ϵ,

$$f(\varepsilon, \mu_e) = \frac{1}{\exp\left[\beta(\varepsilon - \mu_e)\right] + 1}, \tag{3.3.7}$$

where μ_e is the free electron chemical potential which sets their number density n_e and $\beta = 1/(k_B T)$ is the inverse temperature in energy units. The free electron number density is therefore an integral over the Fermi–Dirac distribution weighted by the density of states which results in the following result for the electronic number density [23],

$$n_e(\mu_e, T) = \frac{g}{\Lambda_e^3} \mathcal{F}_{3/2}(z), \tag{3.3.8}$$

where $z = \exp(\beta\mu_e)$ and μ_e is the chemical potential of the electrons. This result includes the spin-degeneracy factor $g = 2s + 1 = 2$ which accounts for electrons having spin $s = 1/2$, and therefore two spin states. Here $\mathcal{F}_\nu$ is a Fermi–Dirac integral of order ν, defined by Equation (1.1.8). The Helmholtz free energy of the ideal Fermi gas is then obtainable through many thermodynamic formulae, for example it may be calculated through its definition

$$F = U - TS, \tag{3.3.9}$$

using the internal energy and entropy formulae given in Ref. [23]. The final result may be

written[2]

$$f^{(e)}_{\text{id,quantum}} = \beta\mu_e - \frac{\mathcal{F}_{5/2}(z)}{\mathcal{F}_{3/2}(z)}. \tag{3.3.10}$$

A numerical scheme was devised to calculate the chemical potential that satisfied Equation (3.3.8) for a given Brückner parameter r_s through a SciPy root finding algorithm and numerical implementation of the Fermi–Dirac functions. This value for the free electron chemical potential was then used to calculate $f^{(e)}_{\text{id,quantum}}$.

As discussed in Section 3.1, on application of the free energy minimisation condition, Equation (3.3.1), to the ideal free energy, Equation (3.3.4), the ideal Saha equation can be recovered in the limit where the free electrons are non-degenerate, $\theta \gg 1$. There are different avenues by which excited atomic states could be included within the calculation, either by assuming a parameterised distribution of states in the atom, and modifying the interaction accordingly, or introducing each excited state as another independent species. These extensions pose no fundamental problems to the calculation, but increase the complexity, and are beyond the scope of this work.

3.3.3 Link to the Saha equation

The effective ionisation potential, given by Equation (3.1.17), takes the form

$$I = E_B^H + \Delta I + \Delta\mu_e.$$

The average energy of an electron in a Fermi gas is larger than that in a classical gas, because lower-lying energy states are blocked through the Pauli principle. This means that $\Delta\mu_e > 0$ and the effective ionisation potential is *increased*. This corresponds to more energy being required to ionise a bound electron. Lastly, the presence of interactions modifies the effective ionisation potential through ΔI, which can be identified as ionisation potential depression

2. Note that the free energy formula presented in the published paper that forms the basis for this chapter, Ref. [45], differs due to the definition of the Fermi–Dirac function. In that work the Fermi–Dirac functions are not normalised by the Gamma function, which is explicitly evaluated in the formula giving an additional factor of $\Gamma(5/2)/\Gamma(3/2) = 2/3$. The order of the Fermi–Dirac functions is also defined such that $\nu \to \nu - 1$.

(IPD). Similar expressions have been used previously to quantify IPD [106, 107]. Inspecting Equation (3.1.14),

$$\Delta I = k_B T \frac{\partial f_{\text{ex}}}{\partial \bar{z}}$$

shows that this quantity acts to reduce the ionisation potential when the excess free energy decreases with increasing ionisation. As will be seen, both the BSC and SRR interactions fall into this category. When these interactions are caused by the implicit binding between free electrons and ions in the plasma, this may be interpreted as continuum lowering. Finally, we note that the free energy minimisation method gives direct access to the IPD and could be exploited for this purpose. The fidelity of the result ultimately depends upon the choice of interparticle potentials, which determine the excess free energy f^{ex}.

3.3.4 Bound-state Coulomb model free energy calculation

To compute the free energy of the BSC model, two coupling parameters $\vec{\lambda} = (\lambda_1, \lambda_2)$ are introduced into the MD potential. The first entry λ_1 controls the strength of pseudo ion interactions, while λ_2 modifies all neutral interactions such that

$$\mathcal{U}^{(\text{MD})}(\vec{\lambda}) = \lambda_1 U^{(\text{ii})} + \lambda_2 \left[U^{(\text{in})} + U^{(\text{nn})} \right]. \tag{3.3.11}$$

The intermediate state $\vec{\lambda} = (1, 0)$ constitutes an ideal gas of neutrals immersed in an interacting OCP. Given that extensive equation-of-state data exist for the OCP, it serves as the *reference* system for the calculation, with excess free energy $f_{\text{ex}}^{(\text{OCP})}$ which depends solely on the effective Coulomb coupling parameter, itself a function of the ionisation state, density and temperature. We provide our own parameterisation of data from Caillol [76, 77], specified in the following section. The OCP data involves integrating over a weakly-coupled system with long-range potentials, where the Debye length is necessarily larger than the box size. In this case, the finite size error is sizeable and many more particles have to be used to estimate the interaction energy in the thermodynamic limit [77]. By using the OCP as the reference

system in the calculation, we overcome these issues in a computationally efficient manner. To compute the free energy of the target system, $f^{(\mathrm{BSC})}(n, T, \bar{z})$, we evaluate,

$$f^{(\mathrm{BSC})} = f_{\mathrm{id}} + f_{\mathrm{ex}}^{(\mathrm{OCP})} + \frac{1}{Nk_BT}\int_0^1 \mathrm{d}\lambda_2 \left\langle U^{(\mathrm{in})} + U^{(\mathrm{nn})} \right\rangle_{(1,\lambda_2)}, \tag{3.3.12}$$

which follows from Equation (3.3.3), over different ionisation states.

3.3.5 Parameterisation of OCP data

Applying Equation (3.3.3), the free energy due to interactions of the OCP system is found through

$$f_{\mathrm{OCP}}^{\mathrm{ex}}(n, T, \bar{z}) = \frac{1}{Nk_BT}\int_0^1 \left\langle U^{(\mathrm{ii})} \right\rangle_{(\lambda_1,0)} \mathrm{d}\lambda_1, \tag{3.3.13}$$

The integral is simply equal to the excess free energy of an OCP at an effective coupling parameter $\Gamma^{\mathrm{eff}} = \bar{\Gamma}(\bar{z}n, T)$, and Equation (3.3.13) may be written [18, 75, 77],

$$f_{\mathrm{OCP}}^{\mathrm{ex}}(\Gamma^{\mathrm{eff}}) = \bar{z}\int_0^{\Gamma^{\mathrm{eff}}} \frac{u_{\mathrm{OCP}}^{\mathrm{ex}}(\Gamma)}{\Gamma}\mathrm{d}\Gamma, \tag{3.3.14}$$

where $u_{\mathrm{OCP}}^{\mathrm{ex}} = U^{\mathrm{ex}}/N_i k_B T$ is the excess internal energy per particle of the OCP at a given coupling parameter, in units of k_BT. We performed a parameterisation of OCP internal energy data from Monte-Carlo simulations by Caillol [76, 77], which are well resolved in the weakly-coupled limit. A finite-size correction scheme is also applied in these works. The functional form,

$$u_{\mathrm{OCP}}^{\mathrm{ex}} = \Gamma^{3/2}\left[\frac{A_1}{\sqrt{\Gamma + A_2}} + \frac{A_3}{\Gamma + 1}\right] + \frac{B_1\Gamma^2}{\Gamma + B_2} + \frac{B_3\Gamma^2}{\Gamma^2 + B_4}, \tag{3.3.15}$$

from Ref. [74] was fitted to the data which includes the asymptotic Debye-Hückel limit of the OCP equation of state. The fitting constants are given in table 3.1 and $A_3 = -\sqrt{3}/2 - A_1/\sqrt{A_2}$.

Figure 3.2 shows excellent agreement across a wide range of Coulomb coupling. The largest

Table 3.1: Coefficient values for the functional form parameterising the excess OCP energy.

A_1	A_2	B_1	B_2	B_3	B_4
-0.99787	0.77480	0.093431	1.5534	0.036253	4.1379

differences from the parameterisations given in Ref. [74] are for weak coupling, where, in this work, there is additional data for low coupling from Ref. [77]. Although we note that these discrepancies are small, this regime is relevant to the overall free energy calculation because it is integrated over. The functional form allowed simple and fast evaluation of the free energy of the reference system which was found by performing the integral in Equation (3.3.14) analytically [74]:

$$\begin{aligned} f^{\mathrm{ex}}_{\mathrm{OCP}}(\Gamma) = {} & A_1\sqrt{\Gamma(A_2+\Gamma)} + A_1A_2\log\left(-\sqrt{\Gamma/A_2}+\sqrt{1+\Gamma/A_2}\right) \\ & + 2A_3\left[\sqrt{\Gamma}-\arctan\sqrt{\Gamma}\right] + B_1\left[\Gamma - B_2\log\left(1+\frac{\Gamma}{B_2}\right)\right] + \frac{B_3}{2}\log\left(1+\frac{\Gamma^2}{B_4}\right), \end{aligned} \tag{3.3.16}$$

where the boundary condition $f^{\mathrm{OCP}}(0) = 0$ has been applied. There is a small discrepancy between line 4 in Equation (3.3.16) and the equivalent term in Ref. [74], which we assume is due to a misprint in the latter, while all other terms formally agree.

3.3.6 Short-range repulsion free energy calculation

To compute the free energy of the SRR model, a third coupling parameter is introduced that controls the strength of the additional repulsive interactions,

$$\mathcal{U}^{(\mathrm{MD})}(\vec{\lambda}) = \lambda_1 U^{(\mathrm{ii})} + \lambda_2\left[U^{(\mathrm{in})} + U^{(\mathrm{nn})}\right] + (\lambda_3)^{12} U^{(\mathrm{nn})}_{\mathrm{SRR}}. \tag{3.3.17}$$

Introducing this parameter to the power of 12, mirroring the dependence of the SRR potential, Equation (3.2.24), on radial separation, avoids singularities when evaluating the ensemble average of $\partial U^{(\mathrm{nn})}_{\mathrm{SRR}}/\partial\lambda_3$ [58]. The free energy is calculated by a natural extension of

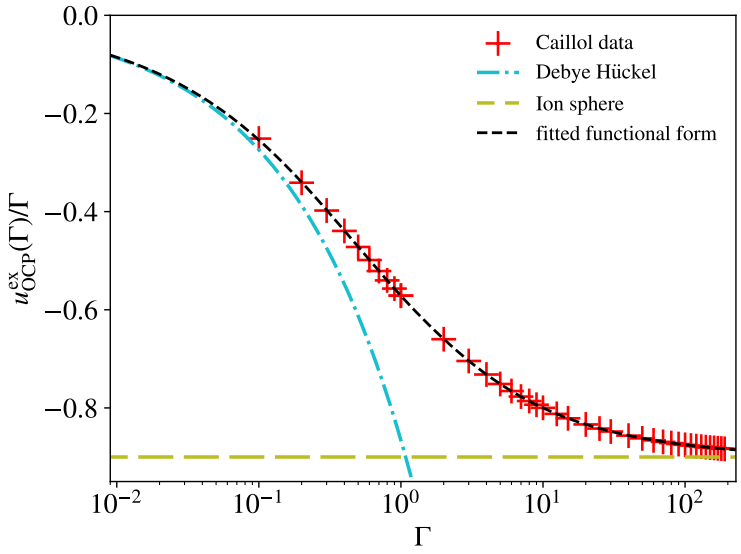

Figure 3.2: Thermodynamic integration curve (black dashed line) used for the reference system in this work. The functional form from Ref. [74] is fitted to OCP data from Refs. [76, 77] given by the red plus symbols. The Debye-Hückel (DH) and ion-sphere (IS) models which are defined in Section 3.4.7 are plotted for comparison.

formula (3.3.3), where the BSC model now acts as the reference system:

$$f^{(\mathrm{SRR})} = f^{(\mathrm{BSC})} + \frac{1}{Nk_BT}\int_0^1 \mathrm{d}\lambda_3 \langle 12\lambda_3^{11} U^{(\mathrm{nn})}_{\mathrm{SRR}} \rangle_{(1,1,\lambda_3)}, \tag{3.3.18}$$

which is an application of Equation (3.3.3) where the coupling vector now has 3 entries $\vec{\lambda} = (\lambda_1, \lambda_2, \lambda_3)$. Computational expense is reduced by choosing the reference system as the BSC model, in which there are already soft repulsive interactions present. The TI method benefits from having similar reference and target systems, such that fewer coupling parameter points are needed to accurately resolve the TI curve and estimate the integral in Equation (3.3.3) [108].

3.4 Simulation Results

Simulation results pertaining to the computation of the ensemble averages in Equations (3.3.12) and (3.3.18) are now presented. The subsequent free energy minimisation and ionisation calculation are also given and discussed. All simulations were performed for a constant

temperature $T = 62500$ K ($k_B T \approx 5.38$ eV) across a range of densities $r_s = a/a_0 = \{4, 3, 2, 1.5, 1, 0.75, 0.5\}$. These conditions were selected because at this temperature, molecule formation between hydrogen atoms is unlikely while partial ionisation is predicted to occur [89, 96]. Ionisation states were chosen in an iterative scheme to sample the minima in free energy. In each simulation $N = 1024$ heavy particles were initialised from a configuration that minimised the potential energy, thermalised for 2.5 ps to the target temperature by applying a velocity rescaling every 0.5 fs, before trajectory data was collected over 5 ps. For both models, statistics were then gathered over 6 independent runs, and used to produce the TI curves discussed below. This procedure ensures that different local configurations of the canonical ensemble are sampled. Finite-size tests were carried out and confirmed sufficient convergence with respect to system size with a relevant example given below. At high densities, $r_s \leq 0.75$, convergence was not reached for the BSC model at low ionisation states. This corresponds to a breakdown of the model and further discussion is provided in Section 3.4.8.

3.4.1 Details of the LAMMPS implementation and simulations

Before discussion of the simulation results, an overview of code implementation and specific LAMMPS features that are used in the TI step is given. As discussed throughout this thesis, the modelling of dense plasmas generally requires a quantum-mechanical element, typically complicating molecular dynamics implementations. However, both the BSC and SRR models are one-component models and therefore use fully classical pairwise potentials, with the electronic quantum effects packaged as underlying assumptions into the interactions. The nature of this approach allows a relatively simple implementation into the LAMMPS codebase [59], which is written in C++ and in an object-oriented style. Specifically, a new pair style was included into the code, which manifests as a class that inherits properties from the FORCE parent class. The pair style features a central compute loop that calculates appropriate interparticle forces and energies based on the charges of each particle, with the magnitude of the additional short-range repulsion determined by the $\mathcal{A}$ parameter.

To compute the trajectories required for the TI calculation, scaling parameters were implemented to modify the strength of the interactions on a per-type basis. For each value of the coupling vector, full MD simulations involving energy minimisation, thermalisation and data collection were then performed. Energy conservation and temperature stability were monitored for these runs and particle trajectory snapshots were saved to data files. Finally, the RERUN feature was used to compute a modified (once again through the scale parameters) pair style over these sampled trajectories through the pre-saved data files. This procedure allowed sufficient flexibility such that no further post-processing was required for the TI calculation.

3.4.2 Computational cost comparison

A standard simulation in this chapter contained $N = 1024$ heavy particles and comprised 2.5 ps of equilibration followed by 5 ps of data collection. Generally, the computational cost increased with density because more particles contributed to the short-range force calculation. As a representative example, the $r_s = 3$, $\bar{z} = 0.5$ BSC simulation required 268 s for the 5 ps production stage on 32 MPI processes. Assuming a similar computational rate during equilibration gives a total wall time of approximately 402 s, corresponding to 3.6 core-hours per independent simulation.

Six independent initial configurations were evolved for each ionisation state and coupling parameter. To obtain an order-of-magnitude estimate, we assume that approximately ten values of both the ionisation state and coupling parameter are sampled, although statistically significant results may be obtainable using fewer values. The total cost at this condition is therefore approximately

$$C_{\mathrm{TI}} \sim (3.6 \text{ core-hours}) \times 6 \times 10 \times 10 \simeq 2 \times 10^3 \text{ core-hours}. \tag{3.4.1}$$

This should be regarded as an order-of-magnitude estimate, since the cost varied with density and ionisation state. Further optimisation of the particle number and numerical parameters

could reduce this cost.

Despite the large number of trajectories required for thermodynamic integration, these classical pair-potential calculations remain substantially cheaper than equivalent first-principles simulations. Ma *et al.* [109] performed finite-temperature Kohn–Sham DFT molecular dynamics for hydrogen at $r_s = 3.23$ and $k_B T = 4.8\,\mathrm{eV}$, close to the conditions considered here. For 14 hydrogen atoms, they report approximately 30 s per timestep on eight CPU cores, using a timestep of 0.1 fs. At the reported computational rate, a trajectory of the same 7.5 ps duration used in the present classical calculations would require approximately 5×10^3 core-hours. The cost of this single DFT state-point trajectory can be compared with the aggregate cost of the classical thermodynamic-integration calculation. Although a standard DFT-MD trajectory does not by itself yield an absolute free energy, the DFT calculation determines the electronic density self-consistently and therefore does not require an explicit ionisation state as external input.

Using the nominal cubic scaling with particle number also discussed in Ref. [109], the corresponding cost for a system containing 1024 hydrogen nuclei and their associated electrons is formally

$$C_{\mathrm{DFT}} \sim 5 \times 10^3 \left(\frac{1024}{14}\right)^3 \simeq 2 \times 10^9 \text{ core-hours.} \tag{3.4.2}$$

This is approximately 10^6 times the cost of the complete classical free-energy calculation at one density. Although this extrapolation is only an order-of-magnitude estimate and depends on implementation details and further averaging over initial configurations that may be required for the DFT calculation, it demonstrates that an equivalent $N = 1024$ Kohn–Sham DFT calculation is practically computationally inaccessible at this condition. By contrast, the more favourable scaling of the classical models will permit substantially larger system sizes than those considered here.

Finally, according to recent private communication, direct PIMC simulations of the uniform electron gas at a similar condition, $r_s = 3.23$ and $T = 55\,700\,\mathrm{K}$, required approximately 10^4 core-hours for a 34-electron simulation capable of resolving equilibrium quantities such as

imaginary-time correlation functions [110]. The cost of a single simulation at this particle number is therefore of the same order of magnitude as the aggregate trajectory cost of the classical thermodynamic-integration calculation. This comparison is illustrative rather than strictly like-for-like, since the uniform electron gas does not include an explicit ionic subsystem.

At the present time, performing direct fermionic PIMC simulations with the particle numbers used in the present classical simulations would be computationally infeasible at this partially degenerate condition. The average fermion sign generally decreases exponentially with particle number, leading to an exponentially increasing sampling cost at fixed statistical precision. This limitation becomes particularly severe as the degeneracy parameter approaches unity and below [20].

3.4.3 Free energy minimisation of bound-state Coulomb model

As an example, TI curves are given on the left-hand side of Figure 3.3, where results are shown for $r_s = 2$ and selected ionisation states. At $\lambda_2 = 0$, all curves start at zero. The neutral trajectories are uncorrelated and therefore sample an integral over the ion-neutral and neutral-neutral potentials, both of which integrate to zero over the box. As λ_2 increases, the curves exhibit an initial sharp decrease, before entering a linear regime. Furthermore, for small λ_2, the fluctuations in the ensemble averages are larger. Both effects are caused by trajectories passing close by one another due to the weak interactions. This results in large fluctuations in the magnitude of the potentials when evaluated over these paths, but with sufficient averaging this effect is reduced, as demonstrated in the left-hand side of Figure 3.3, where the corresponding errors are small. A spline is fit to each curve and integrated to find the free energy using Equation (3.3.12). Given that the spline fitting is less accurate in regions of larger curvature, the integrand is sampled at finer resolution for lower coupling parameters to provide a more accurate calculation of the free energy. The error associated to the final integrated free energy contribution is also available and further discussed in Section 3.4.5.

The right-hand side of Figure 3.3 shows the corresponding free energy curves for the BSC

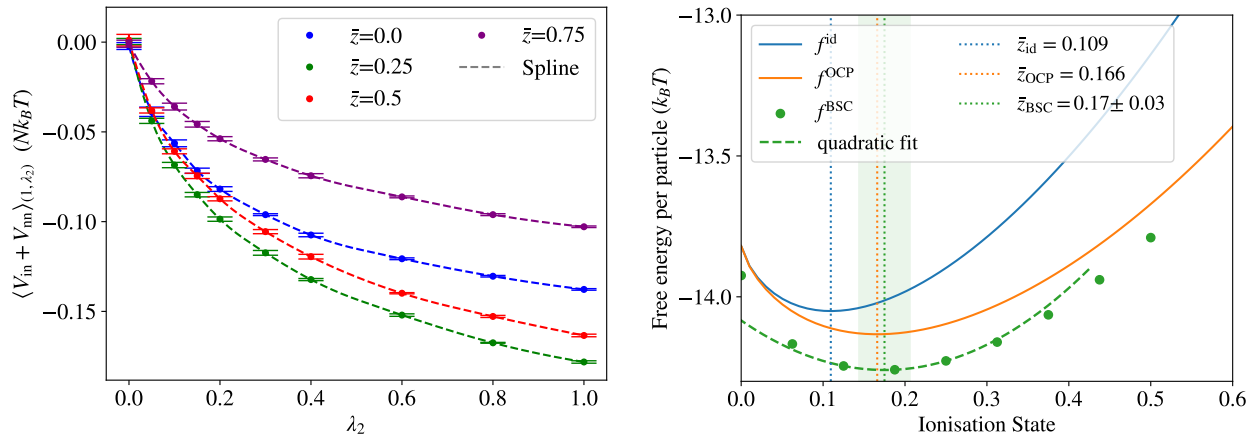

Figure 3.3: Left: Thermodynamic Integration curves for the BSC model at $r_s = 2$, the integrand in Equation (3.3.12) is plotted for different values of λ_2. For clarity, a subset of ionisation states are displayed. The data were averaged over 6 independent runs, while error bars are the corresponding standard deviations. Right: Corresponding free energy minimisation at the same condition. The curves with solid lines correspond to free energies of the ideal (blue, $\vec{\lambda} = \vec{0}$), reference (orange, $\vec{\lambda} = (1, 0)$), and target (purple, $\vec{\lambda} = \vec{1}$) system, while the dotted lines show their minima; the uncertainty in the quadratic minimisation is also displayed in the green shaded rectangle. The corresponding values of these minima are given in the legend.

model, where all sampled ionisation states are included. The ideal case and reference systems are also plotted, which are parameterised functions and are readily minimised. A finite set of data is available to minimise the neutral free energy, and therefore a quadratic curve is fit to the lowest 3 data points to extract the minima. The error mainly depends upon the resolution in ionisation state, which we estimate to be half the interval over which the quadratic curve is fitted. When including the OCP interactions, the collective binding energy between the ions and free electron background *lowers* the free energy at higher ionisation states. Therefore, the ionisation state that minimises the free energy increases. Only ion screening is present and the inclusion of an electronic response would cause a further increase, as there are additional negative free energy contributions due to screening [83]. The increase in ionisation caused by attractive Coulomb interactions is a form of IPD, and corresponds to a lowering of the energy difference between the bound state and the continuum, a connection which was made in Section 3.3.3. At $\bar{z} = 0$, the OCP and ideal systems have the same free energy, as no ions

are present.

The BSC interactions further lower the magnitude of free energy, and the net effect produces a small positive shift in the ionisation state. The decrease in energy is caused by binding between neutrals and the background and the negative asymptote in the neutral-neutral interaction. The latter is the reason for the decrease in free energy at $\bar{z} = 0$ while at $\bar{z} = 1$ the free energies of the target and reference systems necessarily agree. The repulsive effects present in the potentials at small interparticle distances contribute to the small increase in ionisation.

3.4.4 Including short-range repulsion effects

Hard-sphere potentials have been used many times within the chemical picture literature as computational devices [64, 70, 94–96, 103, 111–114]. The charge-neutral interaction in this approach simply restricts the volume accessible to charged species which is an analytically tractable mechanism and has therefore found prevalent use. For example, Saumon and Chabrier found that, at high densities, the free energy of their model was lower when fully neutral compared to when fully ionised [70]. Given that the system was expected to be fully pressure ionised, an additional hard-sphere potential was introduced between neutral species of radius $2a_0$. Although the model presented here does not include the same framework of internal atomic states, or interatomic interactions, we still observe the same phenomenon. Along similar lines, Potekhin introduced an additional unbinding free energy to account for the inner-core screening effect of overlapping atomic orbitals [114]. Furthermore, in many models in the chemical picture, interaction effects between neutrals are modelled directly as hard spheres [96, 103, 113].

Given these motivations, and as a demonstration of the technique, an additional SRR potential (as described in Section 3.2.2) with effective radius $r_* = 1$ has been introduced into the neutral-neutral interaction to study its effect on the predicted ionisation state. We note that such a potential could also be used to model Pauli exclusion effects between bound

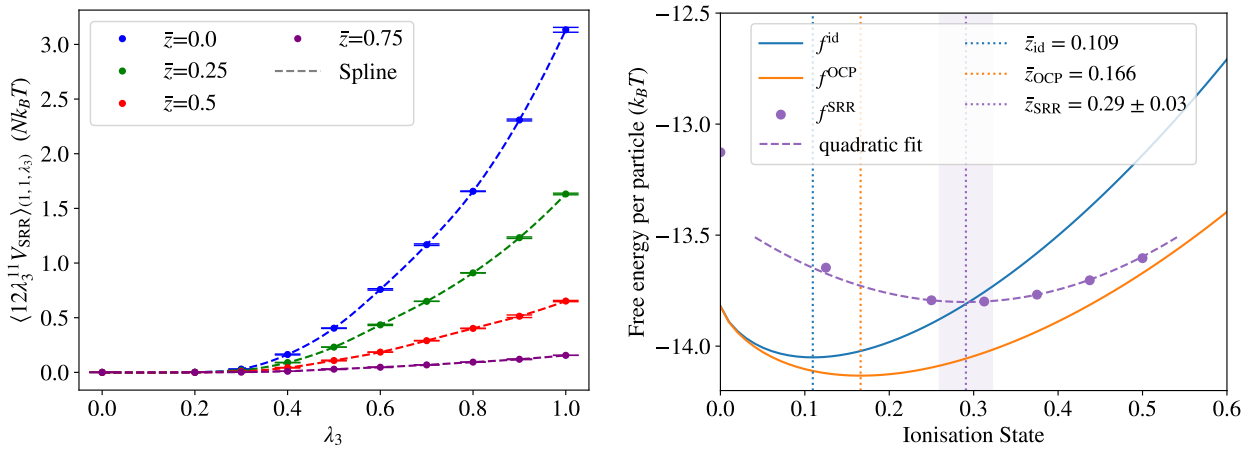

Figure 3.4: Left: Thermodynamic Integration curves for $r_s = 2$ corresponding to the introduction of short-range repulsion into the BSC model. For clarity, a subset of ionisation states are displayed. The data were averaged over 6 independent runs, while error bars are the corresponding standard deviations. Right: SRR model free energy minimisation at $r_s = 2$. The curves with solid lines correspond to free energies of the ideal (blue, $\vec{\lambda} = \vec{0}$), reference (orange, $\vec{\lambda} = (1, 1, 0)$), and target (purple, $\vec{\lambda} = \vec{1}$) system, while the dotted lines show their minima; the uncertainty in the quadratic minimisation is also displayed in the purple shaded rectangle. The corresponding values of these minima are given in the legend.

electrons [84, 104]—these are already treated exactly in the ideal free electron gas but are not present in bound-bound or bound-free interactions. The appropriate form of the repulsive potential is unknown, but could possibly be deduced through comparison with high fidelity data, sourced from experiment or first-principles computations. Alternatively, a scheme based on the pairwise Pauli interactions from wave packet molecular dynamics could be devised [46, 115]. A third integration is required to evaluate the influence of the harder inter-neutral core on the ionisation state. Characteristic integration curves are given on the left side of Figure 3.4 where all curves are suppressed for small λ_3 by the factor of $(\lambda_3)^{11}$ in the derivative of the potential energy function. The free energies for this condition are displayed on the right-hand side of Figure 3.4. The increased atomic repulsion drives the free energy at lower ionisation states up, causing an increase in the minima. The free energy remains below the OCP free energy for higher ionisation states (not shown in figure) due to the attractive neutral-background contributions.

3.4.5 Finite-size tests

Various finite-size tests were performed to check the convergence of the TI calculation. In this section, we present a finite-size study of the free energy calculation for an ionisation state of $\bar{z} = 0.5$ and density of $r_s = 1$ with the BSC model. Different numbers of heavy particles ranging from $N = 128$ to $N = 4096$ were used. To maintain a fixed density, the cubic box was rescaled accordingly with box lengths ranging from $L \approx 8.12\, a_B$ to $L \approx 25.8\, a_B$. TI curves were generated for each case with the same resolution in coupling parameter as used in Figure 3.3. Each curve was then integrated to find the free energy. To calculate the statistical error in the final excess free energy, separate splines were fit to the points given by the upper and lower error bars and integrated accordingly, to give the upper and lower bounds plotted in Figure 3.5. The statistical error is small for all cases, and decreases with system size. This is because, for larger systems, there are more trajectories to sample the integrand in Equation (3.3.12). The systematic error due to system size is also low, and the results are well converged for 2^{10} particles, the number used for all results shown in the main text. As the TI errors are rather small, approximately $5 \times 10^{-3}\, k_B T$ in this case, we assume the error in the full ionisation state calculation is mainly due to having a finite number of free energy data points to minimise.

3.4.6 Thermodynamic integration and resulting free energy data

All collected data is now presented. First, a large number of TI curves were computed during the course of the ionisation calculation. All collected data for the BSC model are presented in Figure 3.6, and all the collected data for additional free energy contributions of the SRR model are presented in Figure 3.7. Inspecting Figure 3.6, a few general trends can be observed. At high densities, when the physical interparticle coupling is stronger, the magnitude of the curves and therefore the final excess free energy contributions are greater. Second, the magnitude of the resulting free energy contribution is not monotonic with respect to ionisation state. For example, by inspecting the $r_s = 1.0$ case, it is evident that for ionisation values

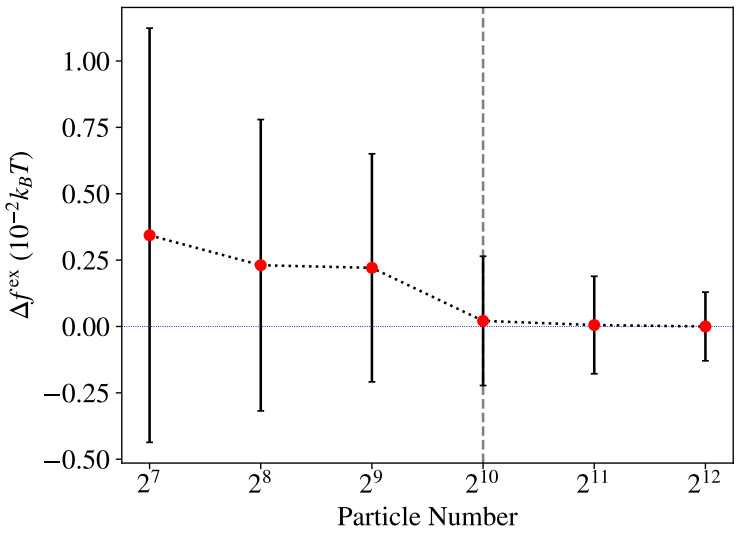

Figure 3.5: Excess free energy of the BSC model computed for different numbers of particles at a fixed density of $r_s = 1$ and ionisation state of $\bar{z} = 0.5$ in units of $10^{-2}k_BT$. The results are shown relative to the result for $N = 2^{12}$ particles: $f^{\text{ex}}_{\text{BSC}} \approx -0.7124$. The dashed grey line indicates the number of particles used for the results in the main text.

close to unity (the red curves), the resulting TI values are small. This is simply because there are fewer neutrals in the system such that the magnitude of their interactions is smaller. As ionisation is increased, the relative magnitude of the TI curves increases, before starting to decrease once more as ionisation tends to zero. This may be attributed to the relative strengths of the ion-neutral and neutral-neutral interactions. Note that all interactions are negative due to the binding between neutrals and free-electron background and attractive asymptote in the neutral-neutral pair potential. The additional screening present in the neutral-neutral interactions provides less binding and therefore contributes less interaction energy during the TI. To summarise, the dependence of the magnitude of the free energy contribution from the BSC TI is a tradeoff between the number of neutrals and the relative strengths of the ion-neutral and neutral interactions. Finally, the dips at very low ionisation and the two highest densities of $r_s = 0.5$ and $r_s = 0.75$ are attributed to an unphysical phase separation between ions and neutrals, further discussed in Section 3.4.8.

All calculated SRR TI curves are shown in Figure 3.7. Similarly to the BSC case, the magnitude of the interactions, and hence the resulting free energy contributions are much

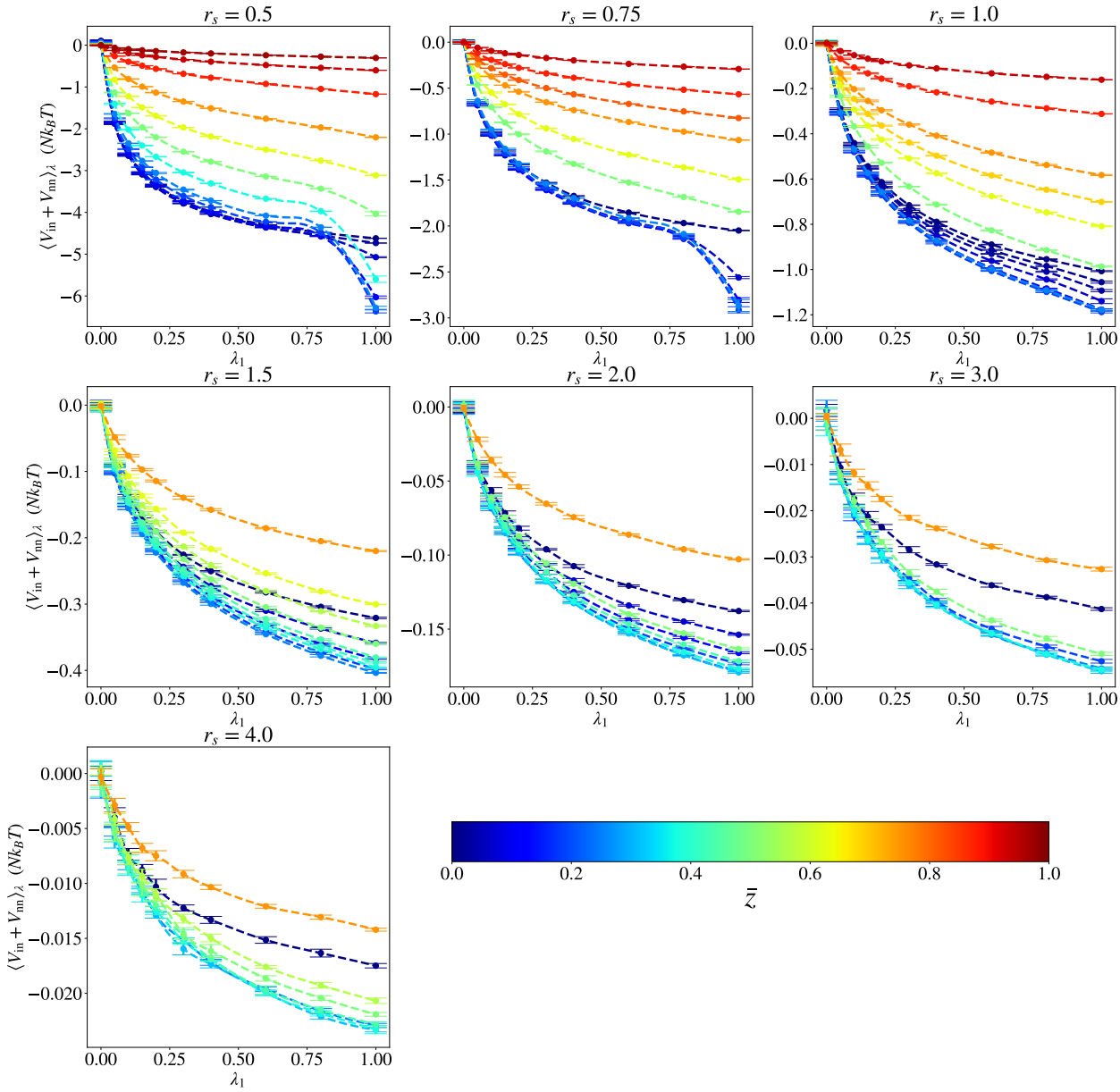

Figure 3.6: Thermodynamic integration data for the BSC model across all considered densities and ionisation states at a temperature of $T = 62500$ K. All y-axes are in units Nk_BT, where N is the total number of electrons. At higher densities (i.e. smaller r_s) larger magnitudes of interaction strength are observed.

greater for higher densities. For presentation purposes some free energy curves for a given density have been split across two subfigures due to the sensitivity of the magnitude with respect to ionisation state. At higher densities and lower ionisation states, neutrals cannot distribute themselves to mitigate the strong repulsive interactions and this manifests as the TI ensemble average evaluating to extremely large values. As previously mentioned, this effect is mitigated at lower coupling by the λ^{11} factor which acts to suppress singularities in $\langle\langle V_{\mathrm{SRR}}\rangle\rangle_{1,1,\lambda_3}$ for small values of the coupling parameter λ_3.

Integrating the curves shown in this section gives the excess free energy of the underlying models at given values of ionisation, density and temperature. These can be combined with calculations for the ideal free energy to produce free energy minimisation curves shown in Figure 3.8. As illustrated in these subfigures, it is clear that the ionisation state is most sensitive to the choice of neutral interaction model at higher densities. Additionally, the BSC interactions do not significantly impact the ionisation state for any considered density. A clear separation between the predictions of the BSC and SRR model manifests at high density.

3.4.7 Simple models for the ionisation state

Before discussing results for ionisation state behaviour across a range of densities, a set of simpler models are introduced. These models contain a similar amount of physics as the MD systems studied here, and are therefore useful for comparison. Here they are presented as models for the excess free energy, but may be converted to an expression for IPD with Equation (3.1.14). The first two models are concerned with the excess OCP contributions to the free energy, linked to the excess internal energy through Equation (3.3.14). The Debye-Hückel (DH) model accounts for ionic screening in the weakly coupled limit [77, 116] and is given by

$$f_{\mathrm{DH}}^{\mathrm{ex}} = -\bar{z}^{3/2}\frac{\Gamma^{3/2}}{\sqrt{3}}. \tag{3.4.3}$$

Alternatively, the ion-sphere (IS) model may be used, which formally provides a lower bound on the excess internal energy, as seen in Figure 3.2, and is applicable in the strongly coupled

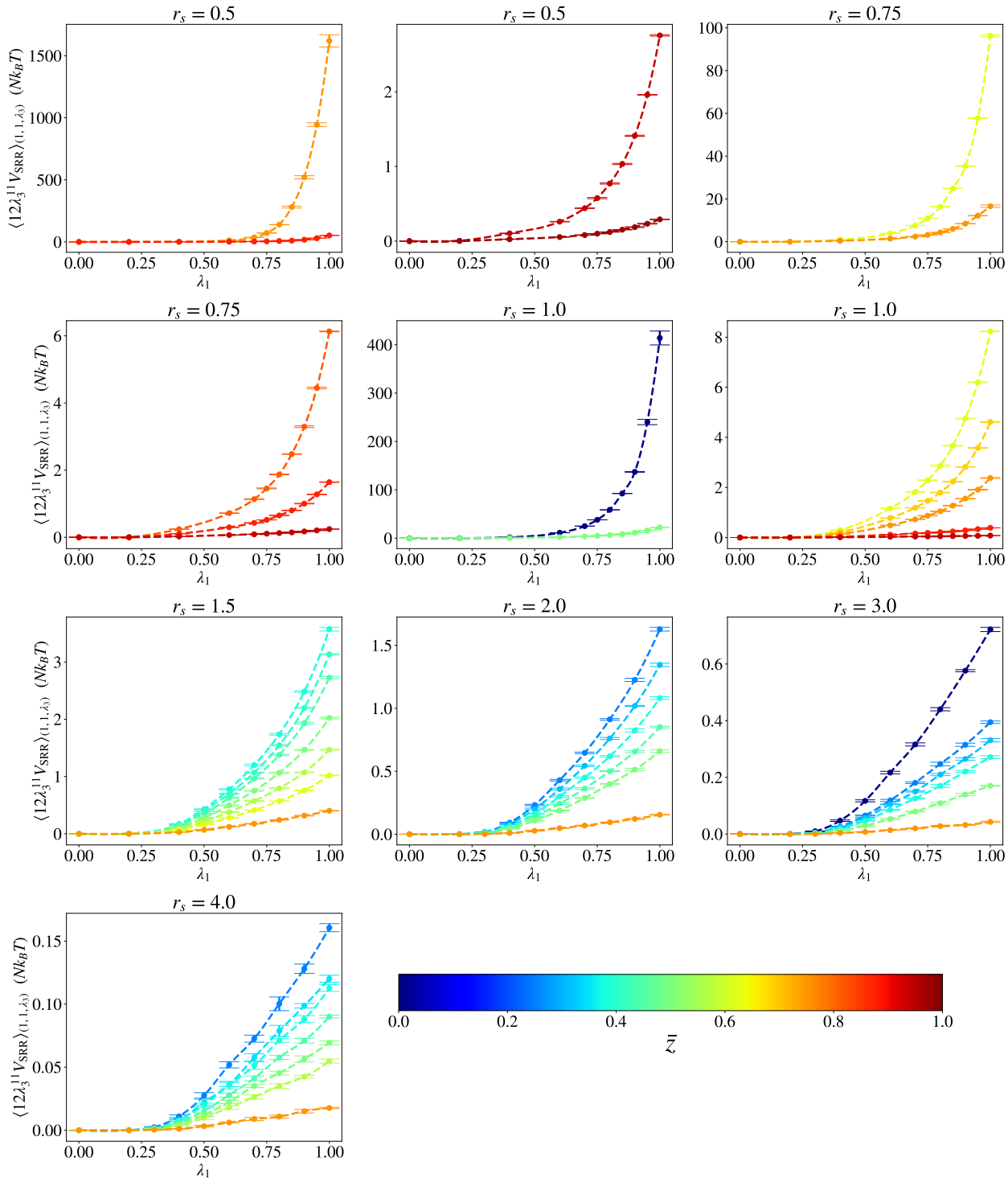

Figure 3.7: Thermodynamic integration data for the SRR model across all considered densities and ionisation states at a temperature of $T = 62500$ K. To resolve a large range of energies, results for some densities have been split across 2 plots.

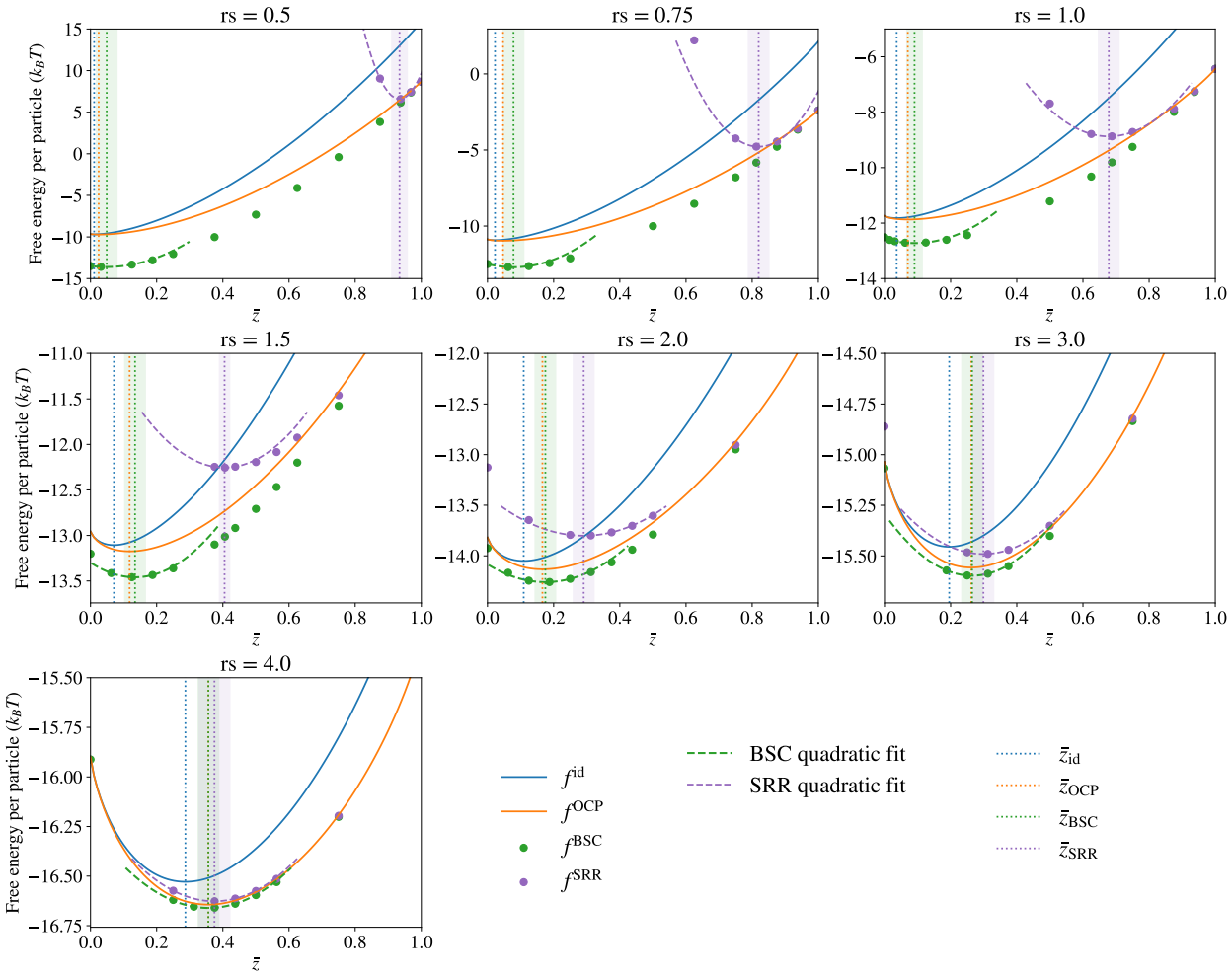

Figure 3.8: Free energy minimisation data for both BSC and SRR models across density and ionisation states at a temperature of $T = 62500$ K. Note that some calculated data points lie outside of the displayed ranges.

limit [116, 117]. The following expression is used,

$$f_{\mathrm{IS}}^{\mathrm{ex}} = -\bar{z}^{4/3}\frac{9\Gamma}{10}. \tag{3.4.4}$$

For the IS model, integration of the potential over the weakly coupled limit introduces a substantial error in the OCP free energy at strong coupling. Therefore alternative reference systems have been suggested in the literature by employing external data [117]. However, to be consistent with commonly used IS models, e.g. Ref. [113], Equation (3.4.4) is used in this work.

Both DH and IS models apply to the OCP subsystem and don't include neutral interactions. To estimate the effect of neutrals, the Carnahan-Starling equation of state may be utilised [118] which provides free energy formulae for interacting hard spheres. Neutrals interacting through the SRR potential with the effective radius r_* may, in a simple approximation, be modelled as hard spheres of radius $R = r_*$. In the model, the excess free energy due to hard-sphere interactions is

$$f_{\mathrm{HS}}^{\mathrm{ex}} = \bar{x}\frac{4\eta - 3\eta^2}{(1-\eta)^2} \quad , \quad \eta = 2\pi\bar{x}nR^3. \tag{3.4.5}$$

Here η is the packing fraction, and, as before, $\bar{x}$ is the neutral fraction. Finally, to estimate the effect of ion and neutral interactions simultaneously, the DH and HS free energy terms may be combined linearly, the minima of which is given by $\bar{z}_{\mathrm{DH+HS}}$. As discussed below, this does not include any effect due to ion-neutral interactions.

3.4.8 Ionisation State across density

The minimisation results from the simulations performed with both the BSC model and SRR model are compiled in Figure 3.9. The ionisation state of the ideal hydrogen plasma decreases with increasing density. This is because the density of free particle states decreases and it becomes energetically favourable to reduce the effective number of species, as discussed in Section 3.1. Including the OCP interactions turns on long-range charged-particle interactions

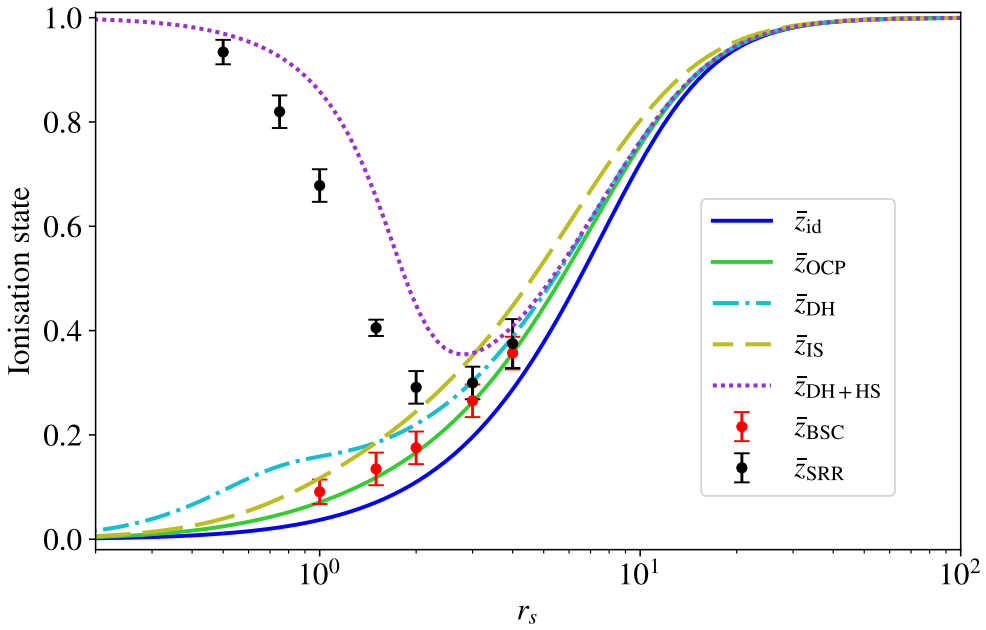

Figure 3.9: Ionisation states for models discussed in the main text plotted against r_s. The BSC model (red) and SRR model (black) correspond to results from numerically minimising free energy data. The solid curves correspond to the ideal case (blue) and OCP reference system (green). The remaining lines relate to the free energy models defined in Section 3.4.7.

and increases the ionisation state. As r_s decreases, the Coulomb coupling parameter is larger, which means the negative excess free energy contributions are greater, and the system exhibits larger binding between the ions and electron background, encouraging ionisation. At the highest densities, $r_s \leq 1$, the free electron degeneracy contributions are dominant and the ionisation state still tends to zero. This is driven by the Fermionic effects in the electrons, which are compared against classical results in Figure 3.10, where the largest discrepancies are seen for $r_s < 2$ and the quantum Fermi energy is significantly higher. If the classical free energy is employed, then a pressure ionisation transition is recovered even in the absence of short-range repulsion effects. Common models for the OCP interactions are the Debye-Hückel and ion-sphere models which, when inserted into the minimisation procedure, give $\bar{z}_{\mathrm{DH}}$ and $\bar{z}_{\mathrm{IS}}$ respectively. These models are defined in the previous section. When compared with the OCP reference calculation, both models overpredict the ionisation state. The Debye-Hückel model is correct in the weak coupling limit, and therefore good agreement is found for $r_s \gtrsim 5$. The ion-sphere model is more appropriate in the strongly-coupled (high density) regime, where

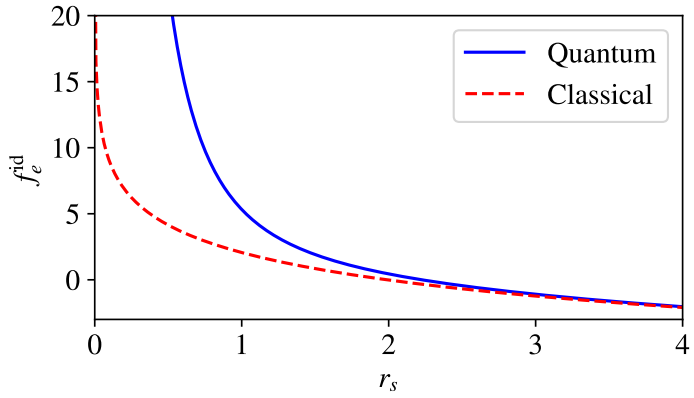

Figure 3.10: Dependence of the reduced ideal free energy for a gas of electrons resolved against r_s at a fixed temperature of $k_B T = 5.38\,\mathrm{eV}$.

it outperforms the Debye-Hückel prediction when compared against the more accurate OCP prediction. Generally, the overprediction for both models is substantial, considering that the magnitude of deviation is similar to the difference between ideal and OCP curves. For example, at $r_s = 2$, the IPD energy predicted by the DH model, calculated using Equation (3.1.14) with each model evaluated at its corresponding minimised ionisation state, is 1.74 times larger than that of the OCP reference system. The deviation is directly related to both models overestimating the magnitude of the excess internal energy, which can be seen in Figure 3.2. We now discuss the effect of introducing neutral interactions, starting with the BSC model introduced in Section 3.2.1. For $r_s \gtrsim 4$, the Coulomb interactions of the neutrals have a negligible effect and the deviation in ionisation from the ideal case is purely driven by OCP interactions in the plasma. As the density increases, the effect of the neutral interactions causes a small increase in the ionisation state. This arises from ion-neutral and neutral-neutral repulsion effects. At the two highest densities considered: $r_s = 0.5$ and $r_s = 0.75$, and for high neutral fractions, the neutral-ion mixture separated into a dense ball of neutral particles surrounded by ions, hence breaking the isotropy of the fluid. This phase separation is a further indication that the inter-neutral potential is too weak and these points are omitted from Figure 3.9. We note that at higher ionisation states, this effect is not present, and allows the BSC system to be used as an appropriate reference system when performing integration

calculations with the SRR potential.

Finally, the effect of increasing the strength of collisions between neutrals has a large effect in the high density region, as expected. The pressure ionisation transition is recovered, because portions of the neutral-neutral potential that were attractive are now repulsive. This illustrates that interaction-induced ionisation is due to both long-range Coulomb interactions and short-range repulsive interactions. For pressure ionisation to occur, an additional repulsive interaction was artificially introduced, suggesting that effects beyond frozen-core Coulomb interactions are required when modelling bound states in dense plasmas. As discussed in the preceding section, by minimising a Debye-Hückel model for the ions combined with a hard-sphere equation of state for the neutrals, the $\bar{z}_{\mathrm{DH+HS}}$ curve is produced. There is qualitative agreement between this model and the full SRR model. However, a limited treatment of the OCP energy, neglect of the ion-neutral interaction, and replacement of the SRR potential by hard spheres results in an overestimation of the ionisation state at high densities.

3.5 Chapter Summary

Molecular dynamics offers considerable flexibility in the choice of interparticle potential and is accurate at arbitrarily strong coupling. Meanwhile, for plasmas, the interparticle potentials are closely connected to the ionisation state. Therefore, the presented thermodynamic integration technique provides the possibility to extend existing models that use the chemical picture. It is also essential to determine the self-consistent ionisation state within molecular dynamics itself for models that could be formulated in the chemical picture such as quantum statistical potentials and wave packet molecular dynamics, which was the primary motivation for this work. Furthermore, the dependence of ionisation state on the interplay between ionic screening and neutral repulsion in hydrogen has been investigated. The excluded-volume method has been used in all chemical-picture-based models of dense plasmas thus far to evaluate repulsive interaction effects. Given that the presented method applies to arbitrary interaction potentials,

we make the first step beyond this paradigm with the bound-state Coulomb and short-range repulsion models.

The results presented from the one-component models motivate further improvements, some of which are addressed in the following chapters. For example, free electron interaction effects can be included either in effective ion-ion potentials [68, 102, 119], potentially with pseudo-potential schemes for bound electrons [71]. The effect of dynamic electrons in two-component models [46] is studied in the following chapters. Generally, free electrons provide additional screening and therefore further lower the free energy at higher ionisation states [83], causing the equilibrium ionisation state to increase. Alternatively, multispecies systems with excited states and multiple charge states can be included within the minimisation framework.

Generally, the development of models in the chemical picture could be particularly useful for developing computational frameworks for ionisation potential depression (IPD), given that known models falter at strong coupling [17], and that IPD is non-trivial to extract from first-principles computations [120–123]. In the results presented, an IPD effect is present, and dominated by ion-ion Coulomb interactions at lower densities. Additionally, molecular dynamics provides a promising route to ionic transport coefficients, provided reliable interparticle potentials are supplied. The framework developed in this chapter allows the ionisation state to be predicted, which helps to assess the validity of the underlying model and ultimately assess the reliability of the resulting transport phenomena.

Having established a self-consistent ionisation framework within classical molecular dynamics, the following chapter extends this methodology to a partially-ionised dense plasma model based on wave packet molecular dynamics, where electronic degrees of freedom are treated dynamically.

Chapter 4

Modelling partially-ionised dense plasma

In this chapter, a wave packet molecular dynamics (WPMD) model appropriate for partially-ionised dense plasma that incorporates bound-state wavefunctions is introduced. As discussed in previous chapters, WPMD is a TCP model that includes dynamic electrons. In the context of dense plasmas, models that include dynamically evolving electrons are generally motivated by their *non-adiabatic* character. That is, they treat the coupled dynamical evolution of both electrons and ions without invoking the Born–Oppenheimer approximation. This is advantageous because it enables energy transfer between classical and quantum subsystems, thereby allowing, in principle, the nonequilibrium study of dense plasmas. Examples include temperature relaxation between ions and electrons [124], as well as the relaxation of non-thermal electron distributions.

A second motivation for wavepacket models is their *scalability*. Their relative simplicity permits simulations of comparatively large system sizes ($N > 1000$), enabling the investigation of long-wavelength phenomena such as hydrodynamic transport. However, this simplicity comes at the cost of accuracy. The approximate nature of these models often reduces their fidelity and frequently renders them semi-empirical, with parameters adjusted to reproduce equilibrium properties. A pertinent example is the requirement of a confining potential in wavepacket models, the form and strength of which must typically be chosen empirically. It remains an open question whether such techniques can ultimately provide robust physical predictions for nonequilibrium properties. Nevertheless, when their semi-empirical character is fully acknowledged and they are carefully benchmarked against *ab initio* methods, wavepacket models can be used to study the structural and dynamical equilibrium properties of dense plasmas while still allowing energy transfer between electrons and ions. They are also of fundamental interest, as they provide a framework for exploring the classical-to-quantum transition in extended dense plasma systems.

In this chapter, the underlying theoretical formalism of wavepacket models is first presented,

followed by appropriate modifications to incorporate bound electronic states within a chemical picture. The numerical scheme used to compute Coulomb interactions and purpose-built Pauli potentials is then introduced. The complete model is subsequently applied to investigate the structural properties of partially-ionised dense hydrogen, with particular emphasis on the role of the confining potential. The self-consistent ionisation state of the model is determined using the framework developed in the previous chapter.

4.1 Bound-state model

In this section, the underlying theoretical description of wavepacket models is reviewed, before the appropriate modifications to include bound electrons are introduced.

4.1.1 Ehrenfest molecular dynamics

In contrast to Section 5.1, where an external ionic potential was considered, here the ions are modelled dynamically. We therefore start at the level of mixed quantum-classical dynamics, specifically Ehrenfest molecular dynamics [37], by considering the non-adiabatic time evolution of a charge-neutral system of N classical protons coupled to N quantum-mechanical electrons. By taking the classical particles to be protons, we specialise to the case of hydrogen, although the generalisation to heavier elements is possible. The proton phase space is therefore parameterised by the spatial coordinates and momenta $\{\boldsymbol{R}_I(t), \boldsymbol{P}_I(t)\}$ where the index $I = 1 \dots N$ labels each proton. Meanwhile the time-dependent electronic state is the N-electron many-body wavefunction $|\Psi_e\rangle$, a vector in the corresponding Hilbert space. The classical Hamiltonian that determines both the total energy and the evolution of the protons is

$$\mathcal{H}(\{\boldsymbol{R}_I(t)\}, \{\boldsymbol{P}_I(t)\}; \Psi_e(t)) = \sum_I \frac{\boldsymbol{P}_I^2}{2M_p} + \frac{e^2}{4\pi\varepsilon_0} \sum_{I<J} \frac{1}{|\boldsymbol{R}_I - \boldsymbol{R}_J|} + \langle\Psi_e|\hat{H}_e(\{\boldsymbol{R}_I\})|\Psi_e\rangle, \quad (4.1.1)$$

where M_p is the proton mass. The ions evolve in the time-dependent mean-field potential of the electrons and under their own Coulomb interactions. For a non-relativistic Coulomb system, the electronic Hamiltonian is

$$\hat{H}_e(\{\boldsymbol{R}_I\}) = -\sum_i \frac{\hbar^2}{2m_e}\nabla_i^2 + \frac{e^2}{4\pi\varepsilon_0}\sum_{i<j}\frac{1}{|\hat{\boldsymbol{x}}_i - \hat{\boldsymbol{x}}_j|} - \frac{e^2}{4\pi\varepsilon_0}\sum_{I,i}\frac{1}{|\boldsymbol{R}_I - \hat{\boldsymbol{x}}_i|}, \tag{4.1.2}$$

where the lower case indices label electrons, ∇_i is the gradient operator with respect to the coordinates of the i-th electron and $\hat{\boldsymbol{x}}_i$ is the position operator. Meanwhile, the electron dynamics are governed by the time-dependent many-electron Schrödinger equation,

$$i\hbar\frac{\partial|\Psi_e\rangle}{\partial t} = \hat{H}_e|\Psi_e\rangle. \tag{4.1.3}$$

Ehrenfest molecular dynamics is used in its exact form within quantum chemistry, where small numbers of degrees of freedom may be studied on short timescales [37]. To access the dynamics of larger systems over longer timescales, the required particle numbers necessitate further approximations.

4.1.2 Mixed bound-free functional form

In the WPMD method [93, 125], the electronic wavefunction is modelled as a parameterised function, in other words the following replacement is made:

$$|\Psi_e\rangle \to |Q(\{q_\mu\})\rangle, \tag{4.1.4}$$

where $\{q_\mu\}$ are the state parameters, which are henceforth constrained to be real. As introduced in Section 5.1, the equations of motion can be derived from a generalisation of Equation (4.1.3), derived from the following action functional [93]:

$$S = \int \mathrm{d}t\mathcal{L}(\{q_\mu\},\{\dot{q}_\mu\}) = \int \mathrm{d}t\langle Q|i\hbar\frac{d}{dt} - \hat{H}_e|Q\rangle, \tag{4.1.5}$$

where $\mathcal{L}$ is the Lagrangian and $|Q\rangle$ is the parameterised many-electron state with the q_μ-dependence now implicit. The time-dependent variational principle now yields the Euler-Lagrange equations,

$$\frac{\partial \mathcal{L}}{\partial q_\mu} - \frac{d}{dt}\frac{\partial \mathcal{L}}{\partial \dot{q_\mu}} = 0, \tag{4.1.6}$$

and reduces to true Schrödinger evolution when the state is unrestricted [93]. This variational principle is also employed in real-time time-dependent density functional theory calculations [37, 39, 126]. The electron dynamics are hence constrained to a submanifold of the full Hilbert space, specified by the choice of $|Q(\{q_\mu\})\rangle$. All further approximations depend on how the parameters are chosen, and for plasmas the state is typically a Hartree product of localised Gaussian wavefunctions [46, 125] – inspired by the point particle description of classical plasma – although antisymmetrized forms have been considered for lower temperatures [127]. In this chapter we follow Ref. [99] and employ a mixed ansatz of N_n bound electrons with single-particle orbitals $|b_i\rangle$ and $N_e = N - N_n$ free electrons with single-particle orbitals $|q_i\rangle$, and choose the constrained many-body wavefunction to be of Hartree form,

$$|Q\rangle = |q_1\rangle \otimes |q_2\rangle \otimes \ldots \otimes |q_{N_e}\rangle \otimes |b_1\rangle \otimes \ldots \otimes |b_{N_n}\rangle. \tag{4.1.7}$$

Imposing this form establishes a chemical picture [94] and the ionisation state must therefore be determined to model equilibrium systems. Here, we determine the ionisation state through the self-consistent method introduced in Chapter 3 [45]. As an alternative, using the schemes outlined in Refs. [93, 99], stochastic transitions between manifolds that include different numbers of bound and free states could be considered as an extension to this work. Note that limited effects due to the missing antisymmetric structure are accounted for through the use of Pauli potentials, introduced in the following section. Applying this framework to hydrogen plasma, we choose the bound-state wavefunction as a propagating, isolated hydrogen ground

state wavefunction attached to a specific proton,

$$\langle \boldsymbol{x}|b_k\rangle = \frac{1}{\sqrt{a_0^3\pi}} \times \exp\left[-\frac{|\boldsymbol{x}-\boldsymbol{r}_k|}{a_0} + \frac{im_e}{\hbar}\boldsymbol{v}_k\cdot(\boldsymbol{x}-\boldsymbol{r}_k)\right]. \tag{4.1.8}$$

Together the ion and bound electron pair form a neutral particle. The variables $\boldsymbol{r}_k$ and $\boldsymbol{v}_k$ denote the position and velocity of a neutral particle. This ansatz may be motivated by applying a Galilean transformation to a stationary 1s wavefunction. An important note is that the functional form does not introduce any additional quantum degrees of freedom, because the bound electrons are assumed to adiabatically follow the motion of underlying protons labelled by $k = 1, \ldots, N_n$. To model free electrons the anisotropic Gaussian state developed in Ref. [46] is employed,

$$\langle \boldsymbol{x}|q_j\rangle = \left((2\pi)^3 \det(\Sigma_j)\right)^{-1/4} \times \exp\left[-\boldsymbol{\xi}_j^T\left(\frac{1}{4}\Sigma_j^{-1} - \frac{i}{\hbar}\Pi_j\right)\boldsymbol{\xi}_j + i\boldsymbol{p}_j^T\boldsymbol{\xi}_j\right], \tag{4.1.9}$$

where Σ_j and Π_j are three-by-three symmetric matrices that parameterise the time-dependent rotation and elongation of the wavepacket and $\boldsymbol{p}_j$ is the expected momentum. The spatial coordinate $\boldsymbol{\xi}_j = \boldsymbol{x} - \boldsymbol{r}_j$ is the relative position vector from the expected position of the wavepacket at $\boldsymbol{r}_j$ and the index $j = 1, \ldots N_e$ labels free electrons. Finally, the remaining $N_i = N - N_n$ protons are relabelled according to the imposed chemical picture with positions $\boldsymbol{r}_i$ where $i = 1, \ldots N_i$, and shall be subsequently referred to as ions.

4.1.3 Equations of motion and total energy

The resulting expression for the wavepacket Hamiltonian is simply the Ehrenfest Hamiltonian, Equation (4.1.1), evaluated for the restricted wavefunction. Explicitly,

$$\mathcal{H} = \mathcal{H}(\{\boldsymbol{r}_i\}, \{\boldsymbol{p}_i\}, \{\boldsymbol{r}_k\}, \{\boldsymbol{p}_k\}; |Q\rangle), \tag{4.1.10}$$

which is a functional of the restricted wavefunction $|Q\rangle$ that depends on the neutral and electron degrees of freedom, i.e.

$$|Q\rangle = |Q(\{\boldsymbol{r}_j\}, \{\boldsymbol{p}_j\}, \{\Sigma_j\}, \{\Pi_j\}, \{\boldsymbol{r}_k\}, \{\boldsymbol{p}_k\})\rangle. \tag{4.1.11}$$

The numerical method by which the state averages are computed is explained in Section 4.2. The equations of motion that follow from Equations (4.1.1) and (4.1.6) for the position and momentum degrees of freedom are

$$\frac{d\boldsymbol{r}_\gamma}{dt} = \frac{\partial \mathcal{H}}{\partial \boldsymbol{p}_\gamma} \quad ; \quad \frac{d\boldsymbol{p}_\gamma}{dt} = -\frac{\partial \mathcal{H}}{\partial \boldsymbol{r}_\gamma}, \tag{4.1.12}$$

for the ions ($\gamma = i$) and neutrals ($\gamma = k$) and the expected positions and momenta of the electrons ($\gamma = j$). Meanwhile, the internal electronic degrees of freedom obey the following symmetrized Hamiltonian equations of motion [46]:

$$\begin{aligned} \frac{d}{dt}\Sigma_{j\alpha\beta} &= \frac{1}{2}\left(\frac{\partial \mathcal{H}}{\partial \Pi_{j\alpha\beta}} + \frac{\partial \mathcal{H}}{\partial \Pi_{j\beta\alpha}}\right), \\ \frac{d}{dt}\Pi_{j\alpha\beta} &= -\frac{1}{2}\left(\frac{\partial \mathcal{H}}{\partial \Sigma_{j\alpha\beta}} + \frac{\partial \mathcal{H}}{\partial \Sigma_{j\beta\alpha}}\right), \end{aligned} \tag{4.1.13}$$

where $\Sigma_{j,\alpha\beta} = [\Sigma_j]_{\alpha\beta}$ is the α, β component of the symmetric width matrix and, similarly, $\Pi_{j\alpha\beta} = [\Pi_j]_{\alpha\beta}$ is a component of the conjugate width-momentum matrix, both corresponding to the j-th electron.

4.1.4 Pauli potentials

We follow an idea based on the pairwise truncation of the antisymmetrization operator [125, 128] which manifests as an effective Pauli potential being added to the classical Hamiltonian. Several works have studied the behaviour of Pauli potentials in the ground state [129, 130], which have resulted in empirical developments through comparison with high-fidelity ground-state data. Here, we wish to study the transition from ionised plasma to atomic gas, where

molecular hydrogen formation is minimal due to thermal dissociation. Therefore, to partially account for the Fermionic nature of the electrons, we assign each a constant spin and include an additional potential between same-spin electrons. Following previous works we include the dominant pairwise antisymmetric kinetic energy contributions [115]. Consider the following two-particle triplet state, constructed from two normalised single-particle orbitals $|\alpha\rangle$ and $|\beta\rangle$:

$$|\Psi_2^A\rangle = |\alpha\rangle \otimes |\beta\rangle - |\beta\rangle \otimes |\alpha\rangle. \tag{4.1.14}$$

An additional pair potential is included that captures kinetic energy contributions to a pairwise antisymmetrized state:

$$\mathcal{V}^P = \frac{\langle \Psi_2^A | \hat{K}_e | \Psi_2^A \rangle}{\langle \Psi_2^A | \Psi_2^A \rangle} - \langle \alpha | \otimes \langle \beta | \hat{K}_e | \alpha \rangle \otimes |\beta\rangle, \tag{4.1.15}$$

where the product state contribution implicitly present within the model has been subtracted. Note that while the product state is normalised, an additional factor is applied to normalise the antisymmetrized state which is consistent with previous models [46, 125]. When summed over all electron pairs, the form of Equation (4.1.15) produces an interaction that depends on all free electron degrees of freedom, and hence increases the complexity of the model significantly. The two particle kinetic energy operator takes the standard form

$$\hat{K}_e = \frac{1}{2m_e} \left(\hat{\boldsymbol{p}}_1^2 + \hat{\boldsymbol{p}}_2^2 \right). \tag{4.1.16}$$

All electrons in the model are assigned a constant spin, and same-spin electrons act through this additional potential while opposite-spin interactions are assumed to be purely electrostatic, neglecting higher-order correlation effects [130].

4.2 Numerical implementation

By including bound-state orbitals in the many-body wavefunction, an extension to the anisotropic wavepacket model developed in Ref. [46] is proposed. Furthermore, the existing LAMMPS [59] implementation has been extended to include the additional bound-state Coulomb and Pauli potentials specified. In this section, we detail an on-the-fly scheme to compute these additional terms, allowing for an efficient numerical implementation.

4.2.1 Bound-state Coulomb interactions

All Coulomb interactions are computed by taking state averages of the electronic Hamiltonian, Equation (4.1.2), with respect to the different single-particle orbitals. Therefore, the pairwise Coulomb interaction between a neutral with index k and ion with index i takes the following form:

$$\begin{aligned} u_C^{(\mathrm{in})}(r_{ik}) &= \frac{e^2}{4\pi\varepsilon_0}\langle b_k| \left(\frac{1}{|\boldsymbol{r}_k - \boldsymbol{r}_i|} - \frac{1}{|\hat{\boldsymbol{x}} - \boldsymbol{r}_i|} \right) |b_k\rangle \\ &= \frac{e^2}{4\pi\varepsilon_0} \frac{\exp[-2r_{ik}/a_0]}{r_{ik}} \left(1 + \frac{r_{ik}}{a_0} \right). \end{aligned} \tag{4.2.1}$$

This depends solely on the ion-neutral radial separation denoted by $r_{ik} = |\boldsymbol{r}_i - \boldsymbol{r}_k|$. The resulting pair potential is a screened, purely repulsive interaction. Similarly, the Coulomb interaction between two neutral particles k and l depends on the radial separation $r_{kl} = |\boldsymbol{r}_k - \boldsymbol{r}_l|$,

$$\begin{aligned} u_C^{(\mathrm{nn})}(r_{kl}) &= \frac{e^2}{4\pi\varepsilon_0}\langle b_k| \otimes \langle b_l| \left(\frac{1}{|\hat{\boldsymbol{x}}_1 - \hat{\boldsymbol{x}}_2|} - \frac{1}{|\boldsymbol{r}_k - \hat{\boldsymbol{x}}_2|} - \frac{1}{|\boldsymbol{r}_l - \hat{\boldsymbol{x}}_1|} + \frac{1}{|\boldsymbol{r}_k - \boldsymbol{r}_l|} \right) |b_k\rangle \otimes |b_l\rangle \\ &= \frac{e^2}{4\pi\varepsilon_0} \frac{\exp[-2r_{kl}/a_0]}{r_{kl}} \left(1 + \frac{5}{8}\left(\frac{r_{kl}}{a_0}\right) - \frac{3}{4}\left(\frac{r_{kl}}{a_0}\right)^2 - \frac{1}{6}\left(\frac{r_{kl}}{a_0}\right)^3 \right), \end{aligned} \tag{4.2.2}$$

which is screened due to the presence of two bound electrons and features a negative (attractive) asymptote, allowing for molecule formation at lower temperatures. These analytical formulae

are equivalent to the BSC model interactions defined in Chapter 3 and provide fast and stable energy and force contributions in the implementation. Given that the free-free and ion-free interactions are already present within the model [46], the final additional Coulomb interaction is the interaction between a free electron and neutral particle. The state average may be written as an integral over the charge density of a free electron with index j and ion-neutral interaction:

$$\begin{aligned} u_C^{(\mathrm{en})} &= \frac{e^2}{4\pi\varepsilon_0}\langle q_j| \otimes \langle b_k| \left(\frac{1}{|\hat{\boldsymbol{x}}_1 - \hat{\boldsymbol{x}}_2|} - \frac{1}{|\hat{\boldsymbol{x}}_1 - \boldsymbol{r}_k|} \right) |q_j\rangle \otimes |b_k\rangle \\ &= \int \mathrm{d}^3\boldsymbol{x}_1 |\langle \boldsymbol{x}_1 | q_j \rangle|^2 u_C^{(\mathrm{in})}(|\boldsymbol{x}_1 - \boldsymbol{r}_k|), \end{aligned} \tag{4.2.3}$$

where the integration kernel $u_C^{(\mathrm{in})}$ is defined in Equation (4.2.1). No closed-form solution is readily available for this integral. To proceed, the integration kernel is approximated as a sum of Gaussian modes using the scheme outlined in Ref. [46],

$$u_C^{(\mathrm{in})} \approx \sum_p c_p \exp[-\alpha_p r^2], \tag{4.2.4}$$

which yields a tractable analytical expression to evaluate the free-neutral energy contributions. This treatment of Coulomb interactions closely mirrors the treatment of the short-range ion-free and free-free Coulomb interactions [46]. To calculate the Coulomb energy through a Gaussian decomposition, the sum over the following integral is required:

$$I_p = \int \mathrm{d}^3\boldsymbol{x} |\langle \boldsymbol{x} | q_j \rangle|^2 \exp\left[-\alpha_p (\boldsymbol{x} - \boldsymbol{r}_k)^2\right], \tag{4.2.5}$$

where p is the index of the respective mode. This integral may be evaluated through standard multidimensional Gaussian integral formulae. A similar expression is found in Appendix A of Ref. [131]. Performing the integral and applying the following identity, which is a special case

of Equation (24) in Ref. [132],

$$\Sigma_i^{-1} - \Sigma_i^{-1}\left(\Sigma_i^{-1} + 2\alpha_p \mathrm{I}\right)^{-1}\Sigma_i^{-1} = 2\alpha_p\left[\mathrm{I} + 2\alpha_p\Sigma_i\right]^{-1},$$

where I is the identity matrix, yields the following formula

$$I_p = \frac{\exp\left[-\boldsymbol{r}^{\mathrm{T}}\left(\alpha_p\left[\mathrm{I} + 2\alpha_p\Sigma_i\right]^{-1}\right)\boldsymbol{r}\right]}{\sqrt{\det\left(\mathrm{I} + 2\alpha_p\Sigma_i\right)}}. \tag{4.2.6}$$

Here $\boldsymbol{r} = \boldsymbol{r}_j - \boldsymbol{r}_k$. This is the final expression used within the mode sum to compute the Coulomb interactions of the model. The electron–neutral pair interaction may now be written

$$\mathcal{V}_{en}^{C}(\boldsymbol{r}_n) = \sum_p c_p I_p. \tag{4.2.7}$$

The internal LAMMPS implementation sums from large to small values of α_p, truncating the sum when energy contributions are negligible. This is motivated by the fact that some modes are only relevant at small interparticle separations, as shown in Figure 4.1.

The c_p and α_p coefficients in Equation (4.2.4) are obtained using the method presented in Ref. [46], which is elaborated here. The integrated squared error weighted by the radial shell volume,

$$L = \int_0^{r_{max}} \mathrm{d}r\, r^2 \left\{V(r) - \sum_p c_p \exp\left[-\alpha_p r^2\right]\right\}^2, \tag{4.2.8}$$

was minimised to find a Gaussian decomposition of $V(r)$. To obtain an analytical formula for the amplitudes, the derivative of the loss function with respect to c_p may be taken, resulting in

$$\frac{\partial L}{\partial c_p} = \int \mathrm{d}r\, 2r^2 \left\{\sum_{p'} c_{p'} \exp\left[-(\alpha_p + \alpha_{p'})r^2\right] - V(r)\exp\left[-\alpha_p r^2\right]\right\}. \tag{4.2.9}$$

Employing the minimisation condition $0 = \partial L/\partial c_p$ and using known formulae for Gaussian

integrals gives the following linear equation,

$$\boldsymbol{b} = \mathrm{A}\boldsymbol{c}, \tag{4.2.10}$$

under the following identifications:

$$[\boldsymbol{c}]_p = c_p \tag{4.2.11}$$

$$[\mathrm{A}]_{pq} = \frac{1}{4}\left(\frac{\pi}{(\alpha_p + \alpha_q)^3}\right)^{1/2} \tag{4.2.12}$$

$$[\boldsymbol{b}]_p = \int \mathrm{d}r\, r^2 V(r) \exp\left[-\alpha_p r^2\right]. \tag{4.2.13}$$

The optimal $\{c_p\}$ coefficients may therefore be obtained through inversion of the A matrix. Therefore, the loss function was numerically minimised with respect to the width coefficients $\{\alpha_p\}$ preconditioned with the optimal amplitude coefficients $\{c_p\}$. With this new notation, the loss is expressed as

$$L(\{\alpha_p\}) = \boldsymbol{c}^{\mathrm{T}}\mathrm{A}\boldsymbol{c} - 2\boldsymbol{c}^{\mathrm{T}}\boldsymbol{b} + \int \mathrm{d}r\, r^2 V^2(r). \tag{4.2.14}$$

For the case of the ion-neutral interaction, it is simple to find an explicit form for the $\boldsymbol{b}$ integral and the final constant term in Equation (4.2.14). To achieve a stable numerical minimisation algorithm, α_p modes were added sequentially. The ion-neutral decomposition used for the simulations performed here is given in Figure 4.1. This decomposition contains 18 modes with a loss of $L < 2 \times 10^{-7}\,\mathrm{Ha}^2\mathrm{a}_0^3$.

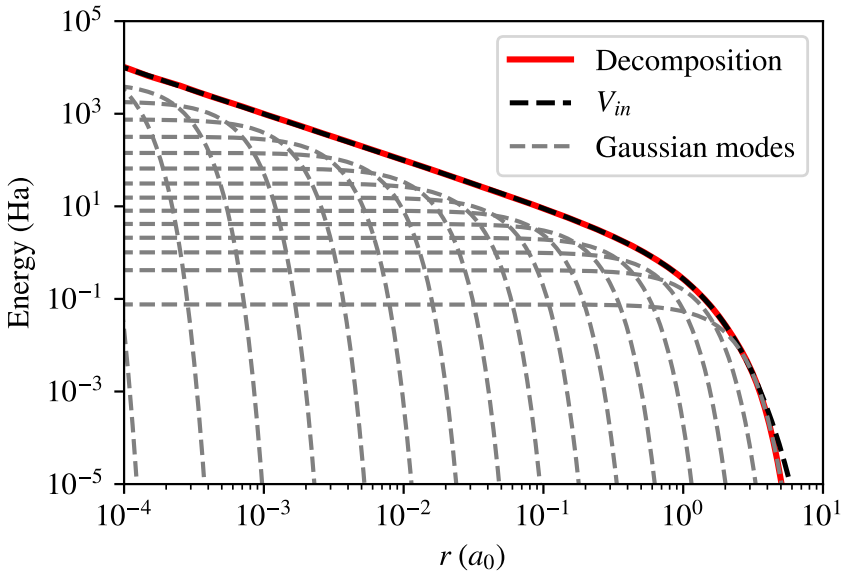

Figure 4.1: Decomposition of the ion-neutral kernel used internally within the LAMMPS implementation to compute the electron-neutral Coulomb energy. Individual Gaussian modes are depicted with grey dashed lines and the sum over these modes is shown in red and closely matches the target (black dashed) line.

4.2.2 Pauli interactions

The general Pauli potential, Equation (4.1.15), may be expressed in terms of single-particle matrix elements,

$$\mathcal{V}^{\mathrm{P}} = -\frac{1}{1-|\langle\alpha|\beta\rangle|^2}\left(\mathrm{Re}\left[\langle\alpha|\frac{\hat{\boldsymbol{p}}^2}{m_e}|\beta\rangle\langle\beta|\alpha\rangle\right] - \frac{1}{2}\left(\langle\alpha|\frac{\hat{\boldsymbol{p}}^2}{m_e}|\alpha\rangle + \langle\beta|\frac{\hat{\boldsymbol{p}}^2}{m_e}|\beta\rangle\right)|\langle\alpha|\beta\rangle|^2\right). \quad (4.2.15)$$

Given that neither closed-form expressions for the kinetic matrix elements nor the overlap are currently available for the free-bound case, a further decomposition of the bound-state orbital in terms of isotropic propagating Gaussians $|g_k\rangle$ is applied to perform on-the-fly calculations,

$$|b_k\rangle = \sum_p c_p |g_{k,p}\rangle, \quad (4.2.16)$$

where

$$\langle\boldsymbol{x}|g_{k,p}\rangle = \left(\frac{2\alpha_p}{\pi}\right)^{3/4}\exp\left[-\alpha_p(\boldsymbol{x}-\boldsymbol{r}_k)^2 + im_e\boldsymbol{v}_k\cdot(\boldsymbol{x}-\boldsymbol{r}_k)\right]. \quad (4.2.17)$$

The c_p and α_p are fitting parameters determined to best approximate the bound state. In the non-propagating case this is a common technique within self-consistent-field calculations, and we have used the decomposition provided by Ditchfield *et al.* based on an energy minimisation procedure [133]. For all simulations, the free-bound calculation was performed using a six mode decomposition, providing an accurate estimate of the kinetic energy. The numerical implementation permits a reduction in the number of modes, balancing computational efficiency against the accuracy of the bound-state representation. Performing the decomposition enables the matrix elements in Equation (4.2.15) to be evaluated. To compute the Pauli interaction on-the-fly, explicit formulae are required for the overlap and kinetic energy matrix elements between anisotropic Gaussians $|q_i\rangle$ and isotropic Gaussians $|g_{j,p}\rangle$. To write down concise expressions for the required quantities the following notation is introduced:

$$\boldsymbol{k}_{ij} = \frac{\boldsymbol{p}_i - \boldsymbol{p}_j}{\hbar} \tag{4.2.18}$$

$$a_{ij} = \boldsymbol{r}_i^{\mathrm{T}} \mathrm{M}_i \boldsymbol{r}_i + \boldsymbol{r}_j^{\mathrm{T}} \mathrm{M}_j^* \boldsymbol{r}_j. \tag{4.2.19}$$

$$\boldsymbol{\Delta}_{ij} = \mathrm{M}_{ij}^{-1} \boldsymbol{c}_{ij} \tag{4.2.20}$$

$$\boldsymbol{c}_{ij} = \mathrm{M}_i \boldsymbol{r}_i + \mathrm{M}_j^* \boldsymbol{r}_j \tag{4.2.21}$$

$$\mathrm{M}_{ij} = \mathrm{M}_i + \mathrm{M}_j^* \tag{4.2.22}$$

$$\mathrm{M}_i = \frac{1}{4}\Sigma_i^{-1} - \frac{i}{\hbar}\Pi_i. \tag{4.2.23}$$

For an isotropic Gaussian $|g_{j,p}\rangle$, as defined in Equation (4.2.17), the internal degrees of freedom reduce to

$$\Sigma_j = \frac{1}{4\alpha_p}\mathrm{I} \quad ; \quad \Pi_j = 0. \tag{4.2.24}$$

Therefore, the general expressions for anisotropic matrix elements are applicable using the notation Equations (4.2.18)–(4.2.23) with minimal alteration. The overlap between two anisotropic wavepackets follows from known formulae for multidimensional Gaussian integrals:

$$\langle q_i|q_j\rangle = \left(8\det\left(\mathrm{M}_{ij}^*\right)\sqrt{\det\left(\Sigma_i\right)\det\left(\Sigma_j\right)}\right)^{-1/2} \times \exp\left[(\boldsymbol{\Delta}_{ij}^*)^{\mathrm{T}}\boldsymbol{c}_{ij}^* - i(\boldsymbol{\Delta}_{ij}^*)^{\mathrm{T}}\boldsymbol{k}_{ij} - \frac{1}{4}\boldsymbol{k}_{ij}^{\mathrm{T}}(\mathrm{M}_{ij}^*)^{-1}\boldsymbol{k}_{ij} - a_{ij}^* + \frac{i}{\hbar}(\boldsymbol{p}_i^{\mathrm{T}}\boldsymbol{r}_i - \boldsymbol{p}_j^{\mathrm{T}}\boldsymbol{r}_j)\right]. \tag{4.2.25}$$

The kinetic energy matrix element may be calculated by equating moments of the product of the real-space wavefunctions to derivatives of the overlap integral, i.e. differentiation under the integral sign. Doing the calculation yields the following result for the mean displacement:

$$\boldsymbol{d}_{ij} = \frac{\langle q_i|\hat{\boldsymbol{x}} - \boldsymbol{r}_j|q_j\rangle}{\langle q_i|q_j\rangle} = -\frac{i}{2}\left(\mathrm{M}_{ij}^*\right)^{-1}\boldsymbol{k}_{ij} + \boldsymbol{\Delta}_{ij}^* - \boldsymbol{r}_j. \tag{4.2.26}$$

which corresponds to the first moment vector. The second-order moment tensor is

$$\mathrm{N}_{ij} = \frac{\langle q_i|(\hat{\boldsymbol{x}} - \boldsymbol{r}_j)(\hat{\boldsymbol{x}} - \boldsymbol{r}_j)^{\mathrm{T}}|q_j\rangle}{\langle q_i|q_j\rangle} = \frac{1}{2}\left(\mathrm{M}_{ij}^*\right)^{-1} + \boldsymbol{d}_{ij}\boldsymbol{d}_{ij}^{\mathrm{T}}. \tag{4.2.27}$$

With these results, the kinetic energy matrix element may now be written concisely:

$$\langle q_i|\frac{\boldsymbol{p}^2}{2m}|q_j\rangle = \left[\frac{\boldsymbol{p}_j^2}{2m} + \frac{2i\hbar}{m}\boldsymbol{p}_j^{\mathrm{T}}\mathrm{M}_j\boldsymbol{d}_{ij} - \frac{2\hbar^2}{m}\mathrm{Tr}(\mathrm{M}_j\mathrm{M}_j\mathrm{N}_{ij})\right]\langle q_i|q_j\rangle. \tag{4.2.28}$$

Using these formulae, the free-free kinetic Pauli potential may be derived; an explicit formula is given in Ref. [24]. For the free-bound interaction, the relevant matrix elements are computed with the following propagating Gaussian mode sums:

$$\langle q_j|b_k\rangle = \sum_p c_p\langle q_j|g_{k,p}\rangle \tag{4.2.29}$$

$$\langle q_j|\hat{\mathbf{p}}^2|b_k\rangle = \sum_p c_p\langle q_j|\hat{\mathbf{p}}^2|g_{k,p}\rangle, \tag{4.2.30}$$

where each Gaussian wavefunction is given in Equation (4.2.17). Application of Equation (4.2.15) gives the free-bound kinetic Pauli potential. To compute the forces, analytical expressions for the matrix element derivatives are required. For the bound-bound interactions, it was numerically confirmed that the velocity dependence is negligible for characteristic neutral thermal velocities at temperatures where partial ionisation is expected. Neglecting the velocity dependence permits known formulae for the stationary 1s wavefunction to be used [134], resulting in the following neutral–neutral pair potential,

$$V_P^{(\mathrm{nn})}(\tilde{r}) = \frac{2\hbar^2}{3m_e a_0^2} \frac{\exp(-2\tilde{r})\left(\tilde{r}^2 + \tilde{r}^3 + \frac{1}{3}\tilde{r}^4\right)}{1 - \exp(-2\tilde{r})\left(1 + 2\tilde{r} + \frac{5}{3}\tilde{r}^2 + \frac{2}{3}\tilde{r}^3 + \frac{1}{9}\tilde{r}^4\right)}, \tag{4.2.31}$$

which acts between neutrals with same-spin bound electrons. Here $\tilde{r} = r_{kl}/a_0$ is the radial distance between two neutral particles labelled by k and l, measured in Bohr radii.

4.2.3 Confining potential

When applying WPMD to systems where ionisation effects are present, electrons tend to spread indefinitely, thereby diminishing their interactions. To remedy this, a confining potential is often used to empirically adjust the extent of the electrons and regularise the model [36, 46, 128, 129]. In fact, even in the noninteracting case, the partition function associated to the classical Hamiltonian will diverge when the electrons are unconfined [135], a feature which is investigated in Chapter 5. In this work, a harmonic potential is added to each free electron through the electronic Hamiltonian,

$$\hat{V}_\Sigma = \frac{A}{2}(\hat{\boldsymbol{x}} - \langle\hat{\boldsymbol{x}}\rangle)^2, \tag{4.2.32}$$

where A is the coupling strength. The effect of this empirical parameter is investigated in the following section. Evaluating the state average in Equation (4.2.32) for each free electron

gives the following contribution to the classical Hamiltonian,

$$\mathcal{V}_\Sigma = \sum_{j=1}^{N_e} \frac{A}{2} \mathrm{Tr}\left(\Sigma_j\right), \tag{4.2.33}$$

which is a special case of the potential already used in Ref. [46]. To estimate a relation between the spatial extent of each free electron and the confinement strength A, the shape kinetic energy for an isotropic wavepacket may be equated with its confining potential. This leads to

$$A = \frac{\hbar^2}{4 m_e \sigma_0^4}, \tag{4.2.34}$$

where σ_0 is a representative unbound confinement width characterising the electrons under a given confining strength. A similar characterization of the confining potential has been used previously in Ref. [136]. After presenting general remarks on the molecular dynamics simulations, the implications of confinement for the resulting structural properties are discussed in the following section.

4.3 The role of the confining potential

4.3.1 Simulation details

To assess the efficacy of the models, we compare against PIMC data from Ref. [47]. While these data provide a valuable benchmark, they remain affected by finite-size errors arising from the restricted system sizes that are computationally accessible within the PIMC method. These data are available for the structural properties of hydrogen at two conditions, both corresponding to a degeneracy parameter of unity, i.e. $\theta = 1$. The low temperature condition corresponds to a Wigner–Seitz radius of $r_s = 3.23$ and temperature of $T = 55700\,\mathrm{K}$. At this condition, hydrogen is generally expected to be a partially-ionised atomic fluid [47, 96] and therefore exhibits strong electron–ion coupling. The high-temperature condition corresponds to a temperature of $T = 145000\,\mathrm{K}$ and Wigner–Seitz radius of $r_s = 2$, and is expected to

be fully ionised. At this condition the electron–ion coupling is weak [119] and bound state formation is minimal due to thermal effects.

Molecular dynamics simulations were performed within a periodic cubic box of volume $V = L^3$, with an Ewald treatment of long-range Coulomb energies and associated forces [46]. For the low-temperature condition, a timestep of 10^{-4} fs and Pauli interaction cutoff of $12\,a_0$ ensured acceptable energy conservation, with the total energy typically deviating by considerably less than one percent from its initial value over the course of an NVE run. The high temperature condition required a smaller timestep of 5×10^{-5} fs, likely because the higher thermal velocities of the particles necessitated finer temporal resolution. To collect particle configuration data for structural analysis, each simulation was initialised from a configuration that minimised the interaction energy, before a velocity scaling procedure was applied to reach the desired temperature. Specifically, both the electron and ion velocities were intermittently rescaled over a 10 fs period to match the target temperature, followed by an additional 25 fs during which only the ion velocities were rescaled. The system was then evolved for 25 fs in the microcanonical ensemble to collect data, over which the fractional change in the total energy $|\Delta\mathcal{H}/\mathcal{H}|$ remained below 2.5×10^{-2} for all simulations referenced in this work.

4.3.2 Calculation of radial distribution functions

The structural properties of the model are investigated through the calculation of radial distribution functions (RDFs), which provide a quantitative measure of spatial correlations between particles. The RDF describes how the local density of a species b varies as a function of distance from a reference particle of species a, relative to the density of an ideal, uncorrelated system at the same average number density. In this sense, $g_{ab}(r)$ captures deviations from perfect spatial randomness: values greater than unity indicate an enhanced probability of finding a particle pair at separation r, while values less than unity indicate spatial depletion. As such, RDFs provide direct insight into short- and intermediate-range ordering, coordination

structure, and correlation effects arising from interactions in many-body systems. This subsection explains how they are calculated for point particles and distributed particles such as Gaussian wavepackets.

The general formula for the instantaneous radial distribution function between a species a and b with respective indices a_i and b_j is [131]

$$g_{ab}(\boldsymbol{x}) = \frac{V}{N_a(N_b - \delta_{ab})} \left\langle \sum_{i=1}^{N_a} \sum_{j=1}^{N_b} {}' \delta^3 \left(\boldsymbol{x} - [\hat{\boldsymbol{x}}_{a_i} - \hat{\boldsymbol{x}}_{b_j}] \right) \right\rangle \tag{4.3.1}$$

where N_a is the number of particles corresponding to species a, δ_{ab} is the Kronecker delta function which ensures correct normalisation of the self RDF, and $\delta^3(\boldsymbol{x})$ is the three-dimensional Dirac delta function. The prime on the sum indicates that for $a = b$, terms with $i = j$ are excluded. Within the context of isotropic systems, the RDF is typically ensemble averaged and further averaged over spherical shells of width δr to give $\bar{g}(r)$. For point particles (the ions), it is possible to express the RDF as a histogram,

$$\bar{g}_{ab}(r) = \frac{1}{V_{\text{shell}}(r, \delta r)} \frac{V}{N_a(N_b - \delta_{ab})} \sum_{i=1}^{N_a} \sum_{j=1}^{N_b} {}' \mathbb{I}(r \leq |\boldsymbol{r}_{a_i} - \boldsymbol{r}_{b_j}| < r + \delta r) \tag{4.3.2}$$

where $\mathbb{I}$ is an indicator function that returns unity if the separation lies within the spherical shell defined by the interval $[r, r + \delta r)$, and zero otherwise. To compute the averaged RDF for arbitrary wavefunctions, we employ the following generalization of Equation (4.3.2):

$$\bar{g}_{ab}(r) = \frac{1}{V_{\text{shell}}(r, \delta r)} \frac{V}{N_a(N_b - \delta_{ab})} \frac{1}{N_s} \sum_{s=1}^{N_s} \sum_{i=1}^{N_a} \sum_{j=1}^{N_b} {}' \mathbb{I}(r \leq |\boldsymbol{y}_{ij}^s| < r + \delta r). \tag{4.3.3}$$

Here, the simple binning of pairwise distances is replaced by N_s independent samples indexed by s and denoted by $\boldsymbol{y}_{ij}^s$. For proton–free electron RDFs, these samples are generated from the following probability distribution:

$$P_{ij}(\boldsymbol{y}) = \langle q_j | \delta^3 \left(\mathbf{y} - [\hat{\boldsymbol{x}}_j - \boldsymbol{r}_i] \right) | q_j \rangle = \frac{\exp\left[-\frac{1}{2} (\boldsymbol{y} - \boldsymbol{r}_{ij})^{\mathrm{T}} \Sigma_j^{-1} (\boldsymbol{y} - \boldsymbol{r}_{ij}) \right]}{\left((2\pi)^3 \det \Sigma_j \right)^{1/2}}. \tag{4.3.4}$$

Similarly, for proton–bound calculations, the corresponding probability distribution is

$$P_{ik}(\boldsymbol{y}) = \langle b_k|\delta^3\left(\boldsymbol{y} - [\hat{\boldsymbol{x}}_k - \boldsymbol{r}_i]\right)|b_k\rangle = \frac{1}{a_0^3\pi}\exp\left[-\frac{2|\boldsymbol{y}-\boldsymbol{r}_{ik}|}{a_0}\right]. \tag{4.3.5}$$

Changing coordinates to $\boldsymbol{z} = \boldsymbol{y} - \boldsymbol{r}_{ik}$ and radially integrating results in the Gamma distribution with shape parameter $k = 3$ and scale parameter $\theta = a_0/2$. This enables a fast sampling routine, since the Gamma distribution can be directly sampled with common numerical libraries. Once radial distances are sampled, angular coordinates are generated from a uniform distribution over the unit sphere to find $\boldsymbol{z}$. These are then translated to obtain samples for $\boldsymbol{y} = \boldsymbol{z} + \boldsymbol{r}_{ik}$.

4.3.3 Structural properties of the fully ionised model

The role of the confining potential in the *fully ionised* model is now analysed. The electronic wavefunction is therefore modelled as a product state of anisotropic Gaussians, with no bound-state wavefunctions. The results for the proton–proton and electron–proton RDFs under the two conditions and for a range of different confinement widths are shown in Figure 4.2. First, we consider the top row, corresponding to the partially-ionised condition at $r_s = 3.23$ and $T = 55700\,\mathrm{K}$. A varying number of independent simulations were carried out at each confinement strength to obtain sufficient statistics, particularly to resolve weakly coupled ions at strong electron confinement. In panel (c), increasing the spatial extent σ_0 reduces the short-range correlation in the electron–proton RDF and at $\sigma_0 = 1.3\,a_0$ only longer-range electron screening remains. At $\sigma_0 = 0.5\,a_0$, the electron–ion RDF shows a stronger short-range correlation. This peak at $r \approx 0.3\,r_s$ corresponding to $r \approx 1.0\,a_0$ is a signature of bound-state formation [96], even though no bound-state wavefunctions are present. A similar correlation shoulder is observed in the reference PIMC data. Two clear limits emerge: When the widths are small, $\sigma_0 \lesssim a_0$, the effective interaction potentials approach those of point particles, exhibiting deep attractive wells in the ion–electron interaction. For large widths, $\sigma_0 > a_0$, the electrons are delocalised, leading to weaker interactions and reduced correlation with the ions.

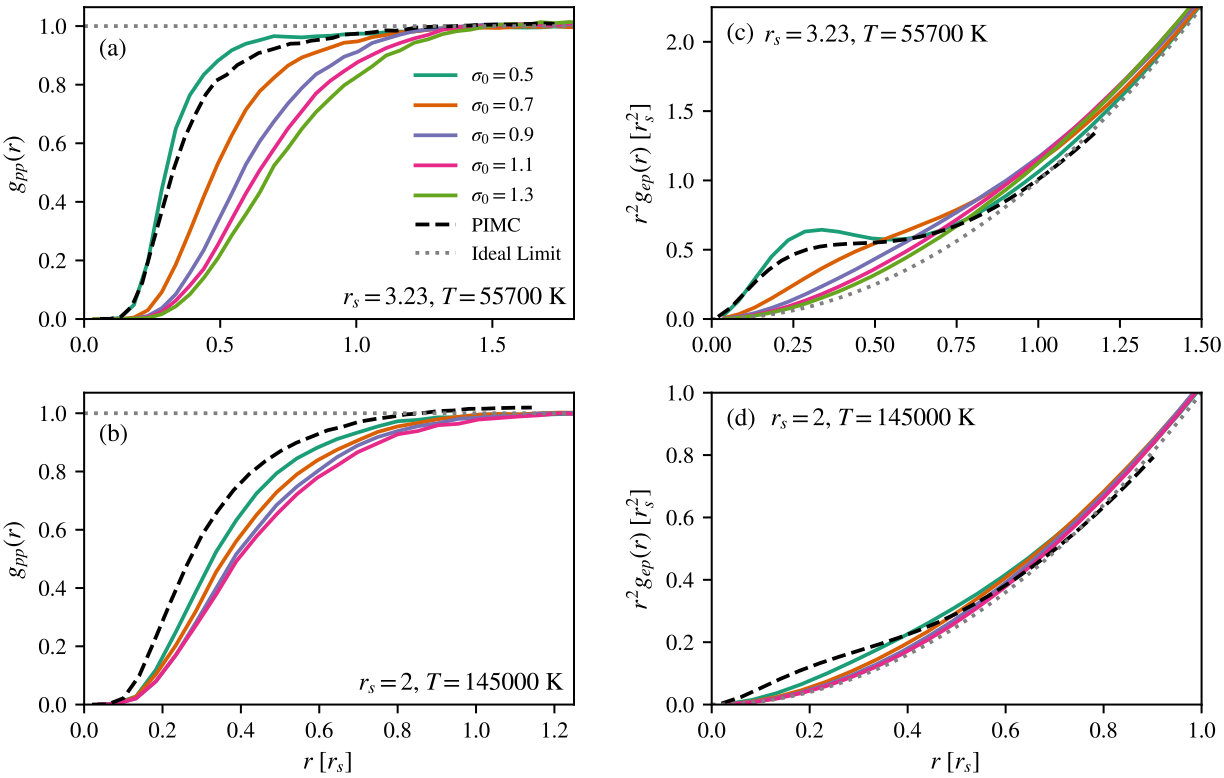

Figure 4.2: Radial distribution function (RDF) dependence on confinement parameter σ_0 for the fully ionised wavepacket model. The results are compared against reference path integral Monte Carlo data from Ref. [47] and the ideal (uncorrelated) limit. Panels (a) and (c) correspond to the proton–proton and radially weighted electron–proton RDFs at the partially-ionised condition: $r_s = 3.23$ and $T = 55700\,\mathrm{K}$. Panels (b) and (d) correspond to proton–proton and radially weighted electron–proton RDFs at the fully ionised condition: $r_s = 2$ and $T = 145000\,\mathrm{K}$. Hartree atomic units are used in the legend.

The corresponding ionic RDFs in panel (a) support this general picture: electronic screening determines the effective ion–ion interaction, and a clear transition is observed from moderately coupled protons at $\sigma_0 = 1.3a_0$ to more strongly coupled protons at $\sigma_0 = 0.5a_0$. At this state point, the structural properties are evidently sensitive to the choice of confinement strength. The second row in Figure 4.2 corresponds to data for the fully ionised condition at $r_s = 2$ and $T = 145000\,\mathrm{K}$. Although a similar general trend is observed, the electron–ion RDF is strongly suppressed. This is a hallmark of weaker electron–ion coupling; consequently, the resulting structural properties are less sensitive to the confinement strength, which supports previous conclusions [36]. In summary, the static structure of dense plasma wavepacket simulations is most sensitive to the confining potential in the partially-ionised regime. Additionally, the

electron–ion coupling – and therefore bound state formation – can be substantially increased by confining the electrons to below the length scale of electron bound states. Regulating the spatial extent of the free electrons alters the model, and, as shown below, the resulting ionisation state becomes a function of the confining parameter.

4.4 Prediction for the partially-ionised model

4.4.1 Ionisation calculation

As discussed in Section 4.1, employing a functional form that consists of N_n bound electrons and N_e free electrons renders the equilibrium charge state distribution a quantity that must be specified *a priori*. In the case of hydrogen, this corresponds to evaluating the ionisation state, $\bar{z}$. The free energy minimisation framework developed in Chapter 3 is therefore employed. To perform the thermodynamic integration, all interactions, denoted by V, are scaled by a coupling parameter λ, leading to a new potential

$$\mathcal{U}(\lambda) = \lambda V. \tag{4.4.1}$$

Using $\mathcal{U}(\lambda)$ directly in molecular dynamics simulations allows the free energy per particle to be calculated with [45, 50]

$$\frac{F}{N} = \frac{F_{\text{id}}}{N} + \frac{1}{N}\int_0^1 \langle V \rangle_\lambda \mathrm{d}\lambda, \tag{4.4.2}$$

where $\langle \cdot \rangle_\lambda$ is an ensemble average for a system defined by the potential energy function $\mathcal{U}(\lambda)$ with coupling parameter λ. To calculate the ideal free energy F_{id}, we assume the expression for classical point particles given in Equation (3.1.4), thereby neglecting the shape kinetic energy of the free electrons to make contact with the known ideal limit, as done previously [99]. The additional dynamical shape degrees of freedom follow the equipartition theorem and therefore contribute additional thermal energy contributions. These additional contributions are also not included, as is common practice when extracting thermodynamic properties from WPMD simulations, see for example, Ref. [137].

Molecular dynamics simulations were performed at different values of λ to sample the potential energy function. For a given ionisation state $\bar{z}$ and value of the coupling parameter λ, 12 independent runs were performed for $N = 1024$ total electrons. After an initial 25 fs of velocity scaling at full coupling ($\lambda = 1$), the coupling parameter was sequentially reduced in discrete steps. Each time the coupling parameter was reduced, a thermalisation step of 10 fs was applied, during which velocity rescaling was applied to maintain the temperature of the system. Following this, data for $\langle V \rangle_\lambda$ were collected for 10 fs, while the system was evolved in the microcanonical ensemble. This process is plotted in Figure 4.3(a) for one initial configuration and $\bar{z} = 1$, in which the modified potential energy $\mathcal{U}(\lambda)$ is also shown. While the ions traverse distances approximately twice the interparticle spacing over 10 fs, averaging over multiple configurations ensures sufficient sampling of the equilibrium distribution; additionally, no large scale fluctuation of $\mathcal{U}(\lambda)$ is present.

The results after averaging the ensemble average across 12 independent runs are plotted in Figure 4.3(b) for five different ionisation states. The error bars represent the standard deviation associated to averaging over independent samples. Note that while these errors are small, the thermal fluctuations in the time trace may still be large, which is the case for small coupling, see Figure 4.3(a). At zero coupling ($\lambda = 0$) the full interacting potential energy function is evaluated over uncorrelated particle trajectories which is equivalent to integrating V over a uniform configuration. A positive contribution from the Pauli interactions emerges in this limit, which is repulsive. Furthermore, each particle experiences Coulomb interactions due to (1) an effective uniform background charge generated by all particles except itself, and (2) its own periodic images. Therefore the self-energy at zero coupling is equal to the Madelung energy [61], which, assuming the spatial extent of the electrons is considerably smaller than the box length L, is given by

$$\langle V_{\text{coul}} \rangle_{\lambda=0} = \frac{e^2}{4\pi\varepsilon_0} \frac{\xi}{2L} 2N. \tag{4.4.3}$$

Here V_{coul} is the Coulomb interactions of the model and $\xi = 2.837297479$ [61] is the Madelung

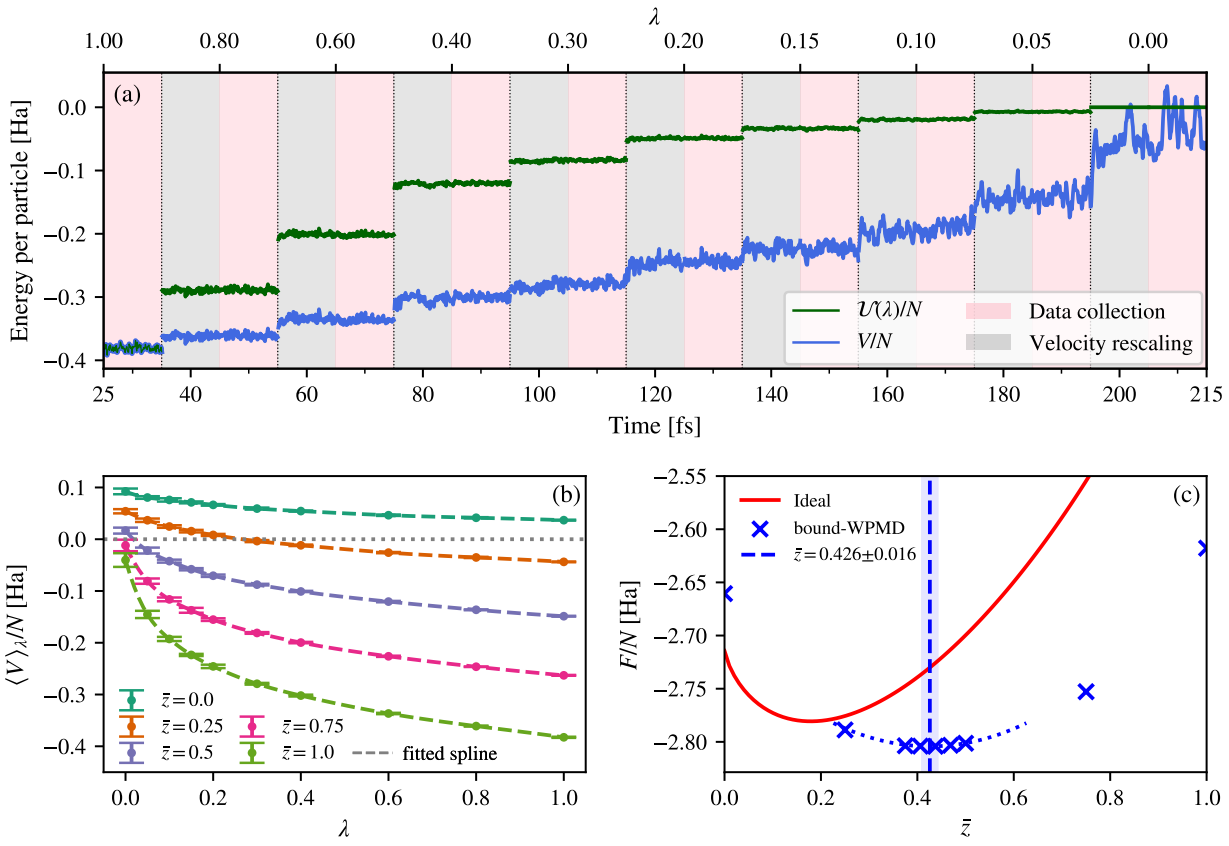

Figure 4.3: Each step of the ionisation calculation for $\sigma_0 = 1.1\,a_0$. Panel (a) shows the time trace of the scaled potential energy function $\mathcal{U}(\lambda)$ and the unscaled energy V across a single molecular dynamics run for $\bar{z} = 1$. The thin black dotted lines indicate the times at which the system coupling parameter is modified, with values given on the top axis. In panel (b) the resulting thermodynamic integration curves are plotted for selected ionisation states $\bar{z}$. Each data point is generated by averaging over 12 runs and taking the mean and standard deviation of the resulting ensemble averages to give the associated error bars. Panel (c) shows the resulting free energy (per particle) minimisation curve generated from all sampled ionisation states, including the final minima of $\bar{z} = 0.426 \pm 0.016$. The analysis method is described in more detail in Ref. [45].

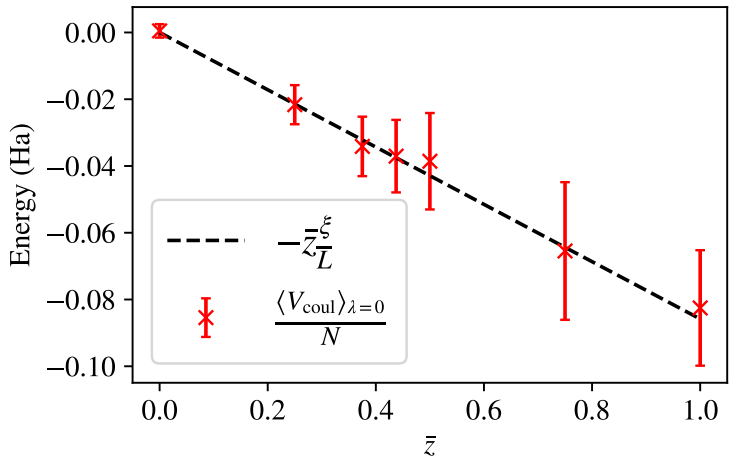

Figure 4.4: Ensemble average of Coulomb energy at zero coupling, compared against the Madelung energy. Here $\sigma_0 = 1.1$ and the error bars are generated in the same manner as Figure 4.3(b).

constant of a simple cubic lattice of ions with unit spacing. This term is also discussed in Section 2.2.1. The short-range neutral Coulomb interactions average to zero when $L \gg a_0$ [45], as discussed in Section 3.2.1 for the BSC model. To benchmark the thermodynamic integration calculation, $\langle V_{\text{coul}}\rangle_{\lambda=0}$ was explicitly calculated and is plotted across ionisation state in Figure 4.4. As can be seen, Equation (4.4.3) holds within statistical error.

As the coupling parameter λ is increased and the corresponding interactions are scaled, particles start to interact and arrange themselves accordingly, meaning $\langle V\rangle_\lambda$ decreases. Similarly to Chapter 3, the calculation exhibits nonlinear behaviour at small coupling, followed by linear scaling around $\lambda \approx 0.3$. Again, to address this imbalance, low coupling values are sampled at a finer resolution. The resulting data are smoothly interpolated with a cubic spline which is integrated to find the excess free energy. Finally, these values are combined with the ideal free energy, and the result is numerically minimised using the same procedure as described in our previous work [45]. The result for $\sigma_0 = 1.1\,a_0$ is shown in Figure 4.3(c). For $N = 1024$ total electrons, we have already shown the finite-size error is minimal when compared to the error bounds of the ionisation state minimisation procedure, see Figure 3.5 and related discussion. It was also checked that long-range Coulomb finite-size effects were not relevant by performing the calculation for a fully ionised system with $N = 256$

total electrons. The difference in the final free energy was within statistical error.

This calculation was repeated for varying electron widths, with the resulting ionisation states and free energies summarised in Table 4.1. Numerical values for the mean electron width,

$$\langle \sigma \rangle = \left\langle \frac{1}{N_e} \sum_{j=1}^{N_e} \frac{1}{3} \mathrm{Tr}\left(\Sigma_j\right) \right\rangle, \tag{4.4.4}$$

are also presented, with the associated error from averaging over distinct runs. These results highlight that the ionisation state and free energy are model-dependent, through their dependence on the confinement parameter σ_0. As confinement strength is increased and the average free electron extent is reduced, the overall free-electron–proton binding energy is increased. This reduces the effective ionisation energy, because it requires less energy to promote a bound electron to a free electron. This *ionisation potential depression* causes an increase in the equilibrium ionisation state and is connected directly to the derivative of the excess free energy with respect to ionisation state in Equation (3.1.14). Note that in the limit of weak confinement, the electrons will become delocalised and therefore comprise a uniform electron background. In this limit, the ionisation state will tend to that of a mixture of neutrals and one-component plasma of ions. At the considered density, the effect of neutral interactions is small and a lower bound on the ionisation state can be produced by combining the ideal free energy with an OCP equation of state, i.e. the green curve in Figure 3.9, which is also presented in Table 4.1 as the OCP model.

Ionisation states may be inferred from path integral Monte Carlo simulations in a variety of ways, see [21, 96, 138–140], although results can differ between approaches. Direct comparison is possible with Ref. [138], where a chemical model employing the Chihara decomposition was fitted to the imaginary-time density-density correlation function. In Figure 4.5, relatively close agreement is found for confinement widths $\sigma_0 = 0.9\, a_0$ and $\sigma_0 = 1.1\, a_0$. We also note that a trajectory analysis approach [96] could be used to determine the number of free electrons (anisotropic wavepackets) that are effectively bound in the simulation. Such an approach may reduce the overall sensitivity in the final ionisation state. However, given that the ionisation

Table 4.1: Ionisation state $\bar{z}$, free energy F, and mean width $\langle\sigma\rangle$, for different confinement parameters σ_0 in Hartree atomic units at $r_s = 3.23$ and $T = 55700\,\mathrm{K}$. Numbers in parentheses denote the associated uncertainty in the final digit. The error in the free energy is estimated by taking the maximum deviation between the quadratic minimum and the neighbouring free energy values adjacent to the lowest sampled data point. For comparison, the inferred path integral Monte Carlo (PIMC) ionisation state from Ref. [138] for $N = 32$ atoms is also given based on data for the imaginary-time correlation function (ITCF). The one component plasma (OCP) model is defined in Ref. [45].

σ_0 $[a_0]$	$\bar{z}_{\min}$	$\langle\sigma\rangle$ $[a_0]$	$-F(\bar{z}_{\min})/N$ [Ha]
0.5	0.66(2)	0.5433(5)	2.934(3)
0.7	0.55(2)	0.832(1)	2.849(1)
0.9	0.47(2)	1.173(1)	2.8196(6)
1.1	0.43(2)	1.574(2)	2.804(1)
1.3	0.382(2)	2.043(4)	2.794(1)

Method	$\bar{z}_{\min}$	Notes
PIMC inferred [138]	0.45	Chemical model fit to ITCF
OCP model [45]	0.24	Scalar minimisation
Ideal	0.18	Scalar minimisation

state is definition-dependent, a rigorous comparison based on structural properties is preferred, and performed in the following section.

4.4.2 Computational cost comparison

A representative fully ionised bound-WPMD simulation containing 1024 protons and 1024 explicit electrons required $1.59 \times 10^4\,\mathrm{s}$ on 16 MPI processes to evolve 25 fs. This corresponds to approximately 70 core-hours. For each ionisation state, the thermodynamic-integration protocol comprised 25 fs of initial thermalisation, followed by ten 10 fs sampling intervals separated by nine 10 fs thermalisation intervals, giving a total trajectory length of 215 fs. One independent thermodynamic-integration sequence therefore required approximately 6.1×10^2 core-hours. Using 12 independent trajectories for each of approximately ten sampled ionisation states gives

$$C_{\text{TI-WPMD}} \sim \left(6.1 \times 10^2\,\text{core-hours}\right) \times 12 \times 10 \simeq 7 \times 10^4\,\text{core-hours} \tag{4.4.5}$$

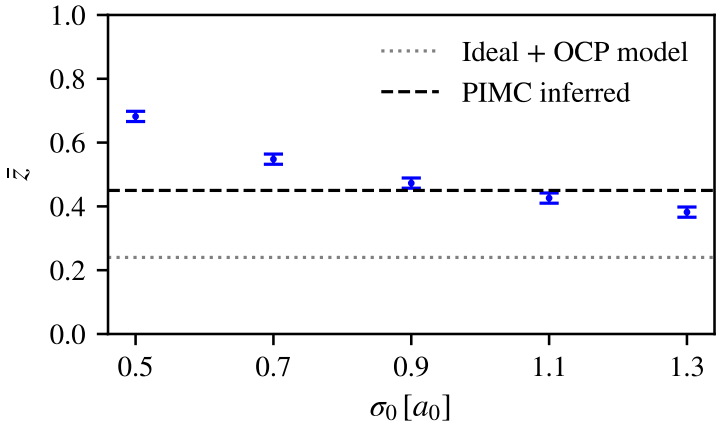

Figure 4.5: Minimised ionisation state $\bar{z}_{\mathrm{min}}$ plotted against confinement parameter σ_0 at $r_s = 3.23$ and $T = 55700\,\mathrm{K}$. Results are presented alongside path integral Monte Carlo inferred results from Ref. [138] and the one component plasma (OCP) model. These data may be found in Table 4.1.

to determine $\bar{z}_{\mathrm{min}}$ for one value of the confinement parameter. Repeating the calculation for all five confinement parameters considered in Table 4.1 therefore required approximately 4×10^5 core-hours. These values are expected to provide upper-bound estimates because introducing bound states reduces the computational cost: their interactions are less expensive to evaluate and the bound electrons have fewer dynamical degrees of freedom.

The OCP result in Table 4.1 was obtained by evaluating an existing parameterisation of the OCP excess free energy and performing a one-dimensional numerical minimisation. Its incremental numerical cost was therefore negligible compared with the bound-WPMD calculation. For comparison, explicitly generating the underlying $N = 1024$ classical free-energy data was estimated in Chapter 3 to require approximately 2×10^3 core-hours, around a factor of 40 less than the equivalent bound-WPMD calculation of $\bar{z}_{\mathrm{min}}$.

As discussed in Section 3.4.2, direct PIMC simulations of the uniform electron gas capable of resolving imaginary-time correlation functions required approximately 10^4 core-hours for 34 electrons at similar thermodynamic conditions [110]. In practice, the average fermion sign decreases rapidly with increasing particle number, leading to an exponentially increasing sampling cost at fixed statistical precision. An equivalent direct PIMC calculation with 1024 protons and 1024 electrons is therefore computationally infeasible at these partially degenerate

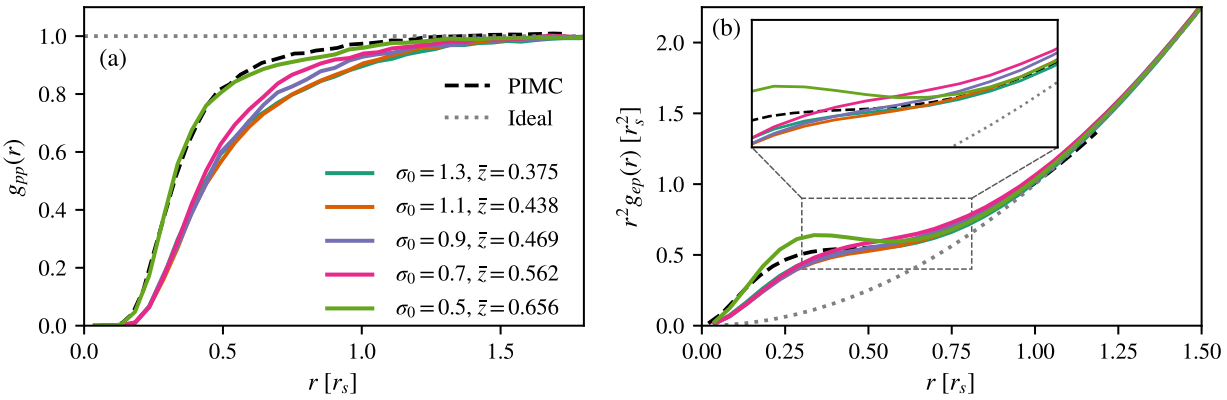

Figure 4.6: Radial distribution functions (RDFs) from the bound-WPMD model for different values of the confinement parameter σ_0. Self-consistent ionisation states are computed via free energy minimisation and found in Table 4.1. (a) proton–proton (pp). (b) electron–proton (ep).

conditions. The bound-WPMD calculation is substantially more expensive than the classical OCP treatment, but remains tractable at particle numbers that are not presently accessible using direct PIMC.

4.4.3 Impact on structural properties

Figure 4.6 shows the structural properties of the partially-ionised model, henceforth referred to as the bound-WPMD model, evaluated at the computed equilibrium ionisation states. The method by which the bound electron RDFs are calculated is discussed below. In Figure 4.6(b), the inclusion of bound-state wavefunctions reduces the sensitivity of the electron–proton correlations for $\sigma_0 \geq 0.7\,a_0$ when compared with the fully ionised model. At these conditions, the electron screening agrees moderately well with the path integral Monte Carlo reference, although the correlation shoulder is slightly diminished at small separation. At $\sigma_0 = 0.5\,a_0$, electron–proton correlations are pronounced, comparable to the fully ionised result shown in Figure 4.2(c). The associated ion structure in Figure 4.6(a) suggests a similar picture. Surprisingly, the enhanced electron–ion interaction for narrow electron widths yields the closest ion structure to the reference data. As discussed in Section 4.3.3, imposing a confinement length scale for the free electrons that is smaller than the characteristic size of the bound states

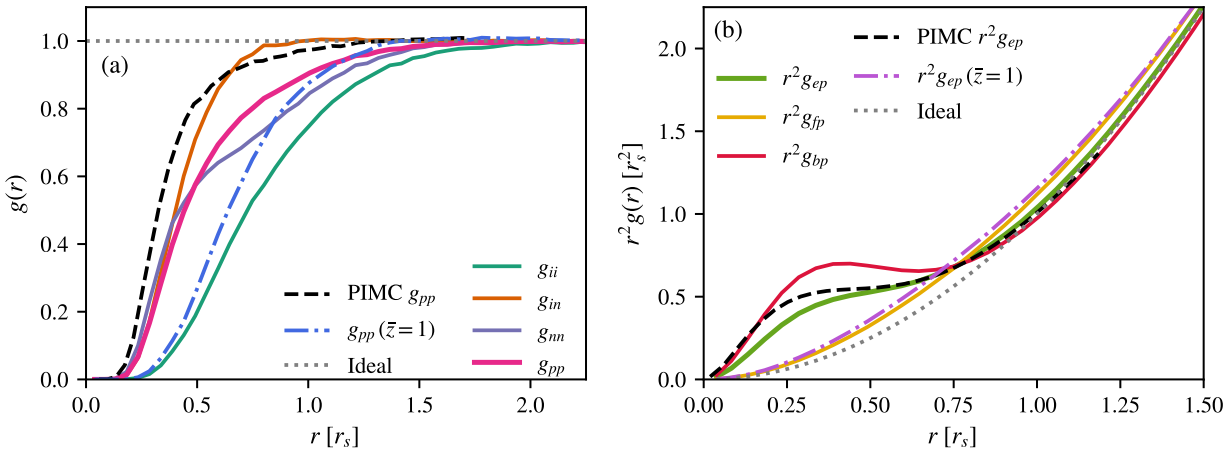

Figure 4.7: Radial distribution functions (RDFs) at $r_s = 3.23$ and $T = 55{,}700$ K computed with the bound-WPMD model for $\bar{z} = 0.44$, compared with path-integral Monte Carlo data, fully ionised ($\bar{z} = 1$) results, and the ideal uncorrelated case. (a) ion–ion (ii), ion–neutral (in), and neutral–neutral (nn) RDFs, combined via Equation (4.4.7) to yield the total proton–proton RDF (pp). (b) Free–proton (fp) and bound–proton (bp) RDFs, combined via Equation (4.4.6) to yield the total electron–proton RDF (ep).

artificially enhances the electron–proton interaction strength. This scenario is unphysical, as genuinely free electrons are expected to exhibit only weak attraction to the ionic cores. This is supported by the very strong electron–ion correlation observed in both the partially and fully ionised results. Furthermore, although the ionisation state has a degree of choice in its definition, best agreement is reached for intermediate confinement parameters in Figure 4.5. Therefore, we proceed with an in-depth analysis of $\sigma_0 = 1.1\,a_0$, which corresponds to an interacting mean width of $\langle\sigma\rangle = 1.57\,a_0$. Returning to Figure 4.2(c), this confinement strength provides some electron–proton long-range screening, as expected in a fully-ionised system, while the electrons are not confined below the extent of the 1s wavefunctions employed within the bound state model.

The full electron–proton RDF is calculated by decomposing into bound and free contributions:

$$g_{ep} = \frac{\bar{z}^2 g_{pf} + (1-\bar{z}) g_{pb}}{\bar{z}^2 - \bar{z} + 1}, \tag{4.4.6}$$

which is exhibited in Figure 4.7. Here the proton–free and proton–bound RDFs, g_{pf} and g_{pb} respectively, are computed through the sampling algorithm presented in Section 4.3.2. The

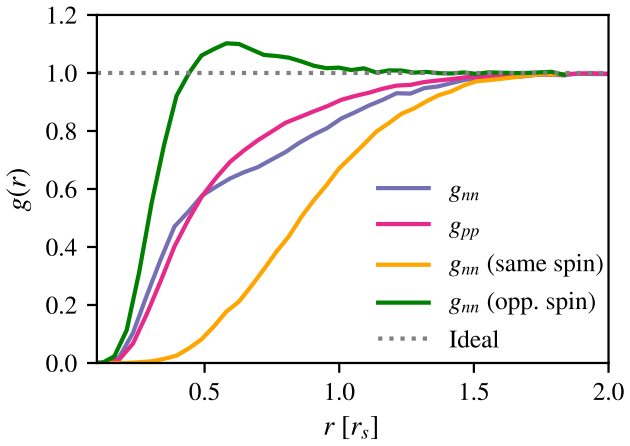

Figure 4.8: Spin-resolved neutral-neutral radial distribution functions (RDFs) at $r_s = 3.23$ and $T = 55{,}700$ K computed with the bound-WPMD model for $\bar{z} = 0.44$. For comparison, the total neutral-neutral and proton–proton RDFs in Figure 4.7 are also plotted.

proton–bound RDF exhibits a clear signature of the bound electrons present in the model, while the proton–free RDF shows longer range screening as observed in the results for $\bar{z} = 1$.

Similar to Equation (4.4.6), a decomposition of the proton–proton RDF

$$g_{pp} = \bar{z}^2 g_{ii} + 2\bar{z}(1-\bar{z})g_{in} + (1-\bar{z})^2 g_{nn} \tag{4.4.7}$$

into ion–ion, ion-neutral and neutral-neutral RDFs denoted by g_{ii}, g_{in} and g_{nn} respectively, is possible. Inspecting Figure 4.7(a), the ion–ion correlation remains moderately coupled. In fact, plotting the ion–ion RDF g_{ii} against an effective Wigner–Seitz radius $\bar{z}^{1/3} r_s$ reveals the ion coupling to be slightly reduced when compared with the proton–proton RDF g_{pp} at $\bar{z} = 1$. The neutral-neutral and ion-neutral RDFs both show weaker short-range correlation, as expected given their heavily screened Coulomb interactions and the repulsive Pauli interactions between same-spin bound electrons. As already discussed, the final combined proton–proton RDF is in better agreement with the path integral Monte Carlo data when compared with the fully-ionised model, although some discrepancy remains. Although the reference data inherently contain finite-size errors, it is nevertheless instructive to consider possible sources of model error within the bound-WPMD model. One explanation could be due to slightly reduced screening observed in the electron–proton correlations, although we note that a

similar effect is seen for the ion–ion RDFs in the fully ionised case in Figure 4.2(b). An alternative explanation is that omission of bound-state polarization artificially enhances the apparent proton–proton coupling in the RDFs; including polarization effects would allow transient molecular-ion (H_2^+) formation and thus reduce the effective coupling. In contrast, the opposite spin neutral-neutral RDF, in Figure 4.8, exhibits a peak indicative of liquid-like structure. This peak originates from the attractive asymptote in the neutral-neutral Coulomb potential, Equation (4.2.2).

4.5 Chapter summary

The bound-WPMD model incorporates an explicit representation of bound electrons and therefore requires a self-consistent determination of the ionisation state. This was achieved using the framework developed in Chapter 3, which combines thermodynamic integration with free energy minimisation. Previous wavepacket-based approaches have accounted for bound-electron effects through semi-empirical effective core potentials in studies of warm dense matter and dynamic electron chemistry [141, 142]. However, these approaches do not include a self-consistent calculation of the underlying charge states. The present work thus provides the first explicit treatment of ionisation equilibria within a wavepacket-based dynamic electron model.

Applying this method to partially-ionised dense hydrogen has enabled a direct comparison of the resulting structural properties with reference path-integral Monte Carlo data. As demonstrated in Section 4.3.3, the confining potential regulates the free electron–ion interaction within the model. Therefore, at physical conditions where strong electron–ion coupling is expected, i.e. partially-ionised conditions, the resulting structural properties are particularly sensitive to its choice. Introducing the partially-ionised model reduces this sensitivity. For weak confinement, there is less electron–ion interaction, which reduces the ionisation potential depression. This results in a smaller ionisation state and therefore increases the electron–ion correlation through inclusion of more bound electrons. At stronger free electron confinement,

there is greater ionisation potential depression, which reduces the number of bound electrons. However, the free electrons have smaller spatial extents and bind more strongly to the ions. A key outcome is that, after imposing physically motivated constraints on the free electron extent, the structural properties of the bound-WPMD model are in better agreement with the selected reference data. This assessment is only possible with a systematic method for determining the ionisation state.

Generally, the inclusion of bound electrons could be used as a scheme in other empirical dynamic-electron MD models for warm dense matter, where weaker-than-expected electron–ion coupling has been identified, for example, Ref. [143]. We emphasize that dense, partially-ionised plasma is a particularly challenging regime to model; in fact, high-fidelity reference data for structural properties have only recently become available [21, 47]. The bound-WPMD model could be extended to molecular hydrogen through the appropriate selection of Pauli potentials [130], or by introducing molecules and molecular ions as additional species and performing additional free energy minimisations. We note that previous works comparing predictions at lower temperatures indicate isotropic Gaussian wavepackets may provide a reasonable description of the structural properties [144]; however, it is well known that they lack the correct molecular binding energies [46]. Introducing additional species would increase the dimensions of the minimisation, although it may be possible to find systematic ways to streamline the free energy calculation [50]. One novel idea would be to use the species' fractions themselves as thermodynamic integration parameters. Additionally, the description of higher atomic number, non-bonded and partially-ionised dense plasma is possible within the framework. This extension, in a hydrogenic framework, would require the consideration of bound states with higher quantum numbers.

Finally, it may be possible to include stochastic transitions between bound and free state manifolds systematically within the framework of wavepacket models [93, 145], providing an interesting course of future research for nonequilibrium modelling of plasmas using dynamic, restricted wavefunction approaches.

Chapter 5

A statistical theory of electronic degrees of freedom

Through the development of an ideal-gas theory for WPMD, a closer analysis is now performed on the role of the confining potential in the model. The content of this chapter is closely related to the material in Reference [49].

As discussed in the previous chapter, WPMD could also complement more established methods for a variety of reasons. In equilibrium, the model captures the joint evolution of electrons and ions over long timescales, enabling direct study of inter-species coupling beyond the Born–Oppenheimer approximation. In addition to dynamic electron properties [36, 146], this allows electron-ion collisional transport to be directly modelled [44]. Furthermore, WPMD has been employed in an ongoing debate regarding the effect of electronic fluctuations on both diffusive and acoustic ion modes in dense plasma [130, 141, 147]. In the previous chapter, the method was extended to include bound-state wavefunctions [48, 99], which allowed the extraction of self-consistent ionisation states [45]. In the nonequilibrium context, the method was used to study the relaxation of a two-temperature electron-proton plasma and yielded slow relaxation rates when compared with semi-classical models [124].

However, as seen in the previous chapter, care must be taken to ensure that the restricted functional form of the electronic wavefunction does not lead to unphysical behaviour. A primary example is the confining potential, which controls the electron extent and hence regulates many properties of the model [48, 135, 146]. The purpose of this chapter is to highlight how the statistical distribution of the additional electron degrees of freedom may be predicted from the Hamiltonian structure of the underlying equations. This provides a practical means to assess the effect of the confining potential. Here, we focus on the statistical properties of WPMD using a Gaussian ansatz, which, as already discussed, has been widely applied to the study of warm dense matter and partially-ionised plasmas.

5.1 Gaussian wavepacket ansätze

One of the wavepacket models studied is the anisotropic Gaussian wavepacket ansatz developed in Reference [46] and used in the previous chapter; see Equation 4.1.9 and associated discussion. The case of isotropic wavepackets is also studied. Constraining the matrices to

$$\Sigma_i = a_i \mathrm{I} \quad ; \quad \Pi_i = \pi_i \mathrm{I}, \tag{5.1.1}$$

where I is the identity matrix and a_i, π_i are real scalars, gives the isotropic state

$$\langle \boldsymbol{x} | g_i \rangle = \mathcal{N} \exp\left[m_i (\boldsymbol{x} - \boldsymbol{r}_i)^2 + \frac{i}{\hbar} \boldsymbol{p}_i^T (\boldsymbol{x} - \boldsymbol{r}_i) \right], \tag{5.1.2}$$

with the complex width variable

$$m_i = \frac{1}{4a_i} - \frac{i}{\hbar}\pi_i. \tag{5.1.3}$$

While the equations of motion for the expected position $\boldsymbol{r}_i$ and expected momentum $\boldsymbol{p}_i$ remain with the same form given in Equation (4.1.12), the evolution equations for the internal degrees of freedom are instead

$$\frac{da_i}{dt} = \frac{1}{3}\frac{\partial \mathcal{H}^{\mathrm{WP}}}{\partial \pi_i} \quad ; \quad \frac{d\pi_i}{dt} = -\frac{1}{3}\frac{\partial \mathcal{H}^{\mathrm{WP}}}{\partial a_i}. \tag{5.1.4}$$

The factor of three is a direct result of transitioning from three spatial degrees of freedom to one in Equation (5.1.1), and could be absorbed by a redefinition of the complex width variable.

The model being employed is equivalent to the fully-ionised model defined in Chapter 4. These modelling choices are briefly reviewed. First, to account for mixed quantum-classical dynamics, Ehrenfest molecular dynamics is employed. Second, all particles are charged and therefore interact through Coulomb interactions, both through the ion-ion interactions and in the electronic Hamiltonian. Third, kinetic Pauli potentials are also employed. These act as effective two-body potentials and are motivated by a pairwise truncation of the antisymmetri-

sation operator [115, 128]. Finally, a confining potential is used to enforce localised Gaussian wavepackets, which is standard in high temperature applications of WPMD. Predicting the effect of this empirical potential is the focus of the present work. An additional potential energy operator, recalled from Equation 4.2.32, is added to the electronic Hamiltonian:

$$\hat{V} = \frac{A}{2}\sum_i \hat{W}_i = \frac{A}{2}\sum_i (\hat{\boldsymbol{x}}_i - \langle\hat{\boldsymbol{x}}_i\rangle)^2, \tag{5.1.5}$$

where $\hat{\boldsymbol{x}}_i$ denotes the position operator of the i-th electron and $\langle\hat{\boldsymbol{x}}_i\rangle$ denotes its expectation value. We have also defined the width-squared operator $\hat{W}_i$, which is used to characterise the extent of the electron wavefunction. As shall be demonstrated, adjusting A modulates the distribution of the width (Σ_i or a_i) variables in the model. This changes the effective Coulomb interactions and resulting structural properties [48]. An alternative scheme based on a global confining potential to impose reflecting wall boundary conditions has also been studied in References [137, 148]. We shall briefly comment how to extend the method presented here to this scheme in Section 5.2.1.

5.2 Statistical theory for the width distribution

In this section, we develop a statistical theory for the internal degrees of freedom based on the non-interacting limit. Specifically, we assume single-particle contributions to the total energy are dominant and that the presence of width-dependent Coulomb and Pauli interactions has a small effect on the internal degrees of freedom. This assumption is correct for sufficiently weakly-coupled systems. More generally, its validity may be assessed by comparison with interacting MD simulations, as performed in Section 5.3. Of course, at sufficiently strongly-coupled conditions, the presence of interactions will perturb the width distribution away from the ideal case. Finally, we note that width distributions have been discussed for isotropic wavepackets in previous works, see e.g. References [124, 125, 137, 149, 150], but they have not been predicted directly.

5.2.1 Anisotropic case

In an ideal gas of anisotropic wavepackets, the Hamiltonian is a sum over kinetic terms and confining potential terms:

$$\mathcal{H}^{\mathrm{WP}} = \sum_i \left(\mathcal{T}_i + \frac{A}{2} \mathrm{Tr}\left\{\Sigma_i\right\} \right). \tag{5.2.1}$$

As discussed in the previous section, the final term represents the confining potential with empirical strength A. This term arises from evaluating the expectation value of Equation (4.2.32) for an anisotropic Gaussian wavefunction, given in Equation (4.1.9). Without this term, the partition function diverges due to infinite wavepacket spread [135]. If, instead, a global confining potential is used, then the final term in this equation should be replaced by an external, position- and shape-dependent potential. For anisotropic wavepackets the kinetic energy is given by [46]

$$\mathcal{T}^{\mathrm{ani}} = \frac{\boldsymbol{p}^2}{2m_e} + \frac{2}{m_e} \mathrm{Tr}\left\{\Pi\Sigma\Pi\right\} + \frac{\hbar^2}{8m_e} \mathrm{Tr}\left\{\Sigma^{-1}\right\}, \tag{5.2.2}$$

where m_e is the electron mass and the particle index has been suppressed. In a non-interacting system with classical Hamiltonian equations, the many-body distribution function factorizes into a set of N single-particle distribution functions:

$$f_1(\boldsymbol{p}, \Sigma, \Pi) = \frac{1}{Z_1} \exp\left[-\beta \left(\mathcal{T} + \frac{A}{2} \mathrm{Tr}\left\{\Sigma\right\} \right) \right], \tag{5.2.3}$$

where $\beta = 1/(k_B T)$ is the inverse temperature and Z_1 is the single-particle partition function associated to the extended phase space of the model [135]. Note that no closed-form expression is readily available for Z_1. To study the resulting distribution over widths, we proceed by integrating the single-particle distribution function over both the position and momentum degrees of freedom to find a marginal distribution in terms of the Σ matrix:

$$f_\Sigma^{\mathrm{ani}}(\Sigma) = \int d^3\boldsymbol{r} \int d^3\boldsymbol{p} \int d^6\Pi \, f_1(\boldsymbol{p}, \Sigma, \Pi). \tag{5.2.4}$$

The Σ matrix is symmetric, and therefore admits an eigendecomposition, $\Sigma = \Lambda D \Lambda^\top$, where $\Lambda \in \mathbb{R}^{3\times 3}$ is an orthogonal matrix of eigenvectors ($\Lambda^\top \Lambda = I$) and $D = \mathrm{diag}(\ell_1, \ell_2, \ell_3)$ is a diagonal matrix of eigenvalues. Therefore, upon making the following change of variables, $\Pi' = \Lambda^\top \Pi \Lambda$, the trace may be written as $\mathrm{Tr}(\Pi\Sigma\Pi) = \mathrm{Tr}(\Pi' D \Pi')$. Orthogonal transformations preserve volume and so the integration measure remains unchanged, i.e. $d^6\Pi = d^6\Pi'$, and the total distribution becomes

$$f_\Sigma^{\mathrm{ani}}(\Sigma) = \mathcal{Z} \exp\left[-\beta\left(\frac{\hbar^2}{8m_e}\mathrm{Tr}\left\{\Sigma^{-1}\right\} + \frac{A}{2}\mathrm{Tr}\left\{\Sigma\right\}\right)\right] I_1, \tag{5.2.5}$$

where $\mathcal{Z}$ is used henceforth as a normalization constant that is redefined as necessary to absorb prefactors. The last term is the following integral:

$$I_1 = \int \exp\left[-\beta\frac{2}{m_e}\mathrm{Tr}\left\{\Pi' D \Pi'\right\}\right] d^6\Pi'. \tag{5.2.6}$$

The matrix Π' is symmetric, so the trace can be expanded accordingly:

$$\mathrm{Tr}(\Pi' D \Pi') = \sum_{p=1}^{3} \ell_p (\Pi'_{pp})^2 + \sum_{1\le p<q\le 3} \left(\ell_p + \ell_q\right)(\Pi'_{pq})^2.$$

Therefore the integral factorizes into six independent Gaussian integrals. Performing these integrals yields

$$f_\Sigma^{\mathrm{ani}}(\Sigma) = \mathcal{Z}\left(\prod_{p=1}^{3}\frac{1}{\sqrt{\ell_p}}\right)\left(\prod_{1\le p<q\le 3}\frac{1}{\sqrt{\ell_p+\ell_q}}\right)\exp\left[-\beta\left(\frac{\hbar^2}{8m_e}\mathrm{Tr}\left\{\Sigma^{-1}\right\} + \frac{A}{2}\mathrm{Tr}\left\{\Sigma\right\}\right)\right]. \tag{5.2.7}$$

Since the shape matrix Σ is symmetric, it has six degrees of freedom. We wish to study the distribution of widths, which depend on the three eigenvalues of Σ, denoted by ℓ_1, ℓ_2, ℓ_3. To isolate these, we express the integral in terms of these three variables and integrate over the three rotation variables μ_1, μ_2, μ_3 which parameterise the possible orientation of the eigenbasis.

It is possible to show that the Jacobian associated to this transformation is [151]

$$\mathcal{J}(\ell_1, \ell_2, \ell_3, \mu_1, \mu_2, \mu_3) = \prod_{1 \le p < q \le 3} |\ell_p - \ell_q| g(\mu_1, \mu_2, \mu_3), \tag{5.2.8}$$

where g is the distribution function of the μ degrees of freedom. After integrating over the rotational degrees of freedom, the marginal distribution function over the eigenvalues is

$$f_{\boldsymbol{\ell}}^{\text{ani}}(\ell_1, \ell_2, \ell_3) = \mathcal{Z} \left(\prod_{p=1}^{3} \frac{1}{\sqrt{\ell_p}} \right) \left(\prod_{1 \le p < q \le 3} \frac{|\ell_p - \ell_q|}{\sqrt{\ell_p + \ell_q}} \right) \exp\left[-\beta \left(\frac{\hbar^2}{8 m_e} \sum_{p=1}^{3} \frac{1}{\ell_p} + \frac{A}{2} \sum_{p=1}^{3} \ell_p \right) \right]. \tag{5.2.9}$$

To characterize the resulting distribution we sample directly from the joint distribution of the eigenvalues $\boldsymbol{\ell} = (\ell_1, \ell_2, \ell_3)$ defined in Equation (5.2.9). From each set of sampled eigenvalues we calculate the widths

$$\sigma_p = \sqrt{\ell_p} \quad \text{for} \quad p = 1, 2, 3\,, \tag{5.2.10}$$

which provide a more natural physical interpretation. In order to characterize the statistics of these widths we consider the distribution of an individual width, denoted P_{σ}^{ani}, obtained by pooling all σ_i values across samples. Additionally, to measure the total wavepacket extent, we define the root-mean-squared (RMS) width as

$$\bar{\sigma} = \sqrt{\frac{1}{3} \langle \hat{W} \rangle} = \sqrt{\frac{1}{3} (\sigma_1^2 + \sigma_2^2 + \sigma_3^2)}, \tag{5.2.11}$$

where the first equality is the general definition in terms of the width-squared operator defined in Equation (5.1.5). Evaluating the state average for the specific case of anisotropic wavepackets yields the second equality. The marginal probability distribution function (PDF) of the RMS width $\bar{\sigma}$ is denoted $P_{\bar{\sigma}}^{\text{ani}}$. These two marginal distributions capture, respectively, the typical fluctuations of a single component and the collective behaviour of the total width.

5.2.2 Isotropic case

The equivalent Hamiltonian for an ideal gas of isotropic wavepackets is

$$\mathcal{H}^{\mathrm{WP}} = \sum_i \left(\mathcal{T}_i + \frac{3A}{2} a_i \right), \tag{5.2.12}$$

which includes the state average of the confining potential using the isotropic wavepacket form given in Equation (5.1.2). For isotropic wavepackets, the kinetic energy is

$$\mathcal{T}^{\mathrm{iso}} = \frac{\boldsymbol{p}^2}{2m_e} + \frac{6}{m_e}\pi^2 a + \frac{3\hbar^2}{8m_e a}, \tag{5.2.13}$$

where the particle index is suppressed. Following the same procedure as the previous subsection and integrating over all momentum-like degrees of freedom gives the following distribution function over a,

$$f_a^{\mathrm{iso}}(a) = \sqrt{\frac{3A\beta}{2\pi a}} \exp\left[-\beta \left(\frac{3\hbar^2}{8m_e a} + \frac{3}{2}Aa - \frac{3}{2}\hbar\sqrt{\frac{A}{m_e}} \right) \right]. \tag{5.2.14}$$

Here the normalization factor has been explicitly calculated. The width metric employed for the anisotropic case can also be applied to the isotropic case. Specifically, we define the isotropic width variable

$$\sigma = \sqrt{\frac{1}{3}\langle \hat{W} \rangle} = \sqrt{a}, \tag{5.2.15}$$

where the second equality is evaluated for the isotropic Gaussian, Equation (5.1.2), in contrast to the anisotropic wavefunction used to evaluate the state average appearing in the second equality of Equation (5.2.11). The width variable σ has the following marginal distribution function:

$$f_\sigma^{\mathrm{iso}}(\sigma) = 2\sigma f_a^{\mathrm{iso}}\left(\sigma^2\right), \tag{5.2.16}$$

which is the isotropic equivalent of the marginal probability of the averaged width $P_{\bar{\sigma}}^{\text{ani}}$. It is also possible to obtain a closed-form expression for the mean width of the distribution,

$$\begin{aligned}\langle\sigma\rangle^{\text{iso}} =& \int \sigma f_{\sigma}^{\text{iso}}(\sigma) d\sigma \\ =& \sqrt{\frac{3\hbar^2\beta}{2\pi m_e}} \exp\left[\frac{3}{2}\hbar\beta\sqrt{\frac{A}{m_e}}\right] K_1\left[\frac{3}{2}\hbar\beta\sqrt{\frac{A}{m_e}}\right]\end{aligned} \tag{5.2.17}$$

where $\langle\cdot\rangle^{\text{iso}}$ denotes the statistical average with respect to the isotropic width PDF and $K_\alpha[\cdot]$ denotes the modified Bessel function of the second kind of order α. Additionally, the maximum of the distribution, calculated with

$$\frac{\partial f_{\sigma}^{\text{iso}}}{\partial \sigma} = 0, \tag{5.2.18}$$

gives the isotropic modal width:

$$\text{mode}(\sigma) = \left(\frac{\hbar^2}{4m_e A}\right)^{1/4}. \tag{5.2.19}$$

An equivalent result was obtained in Section 4.3 by equating shape kinetic energy and confining potential terms. It may therefore be concluded that the confinement parameter σ_0 which was used to identify an approximate electronic lengthscale in the previous chapter is equivalent to the modal width of an ideal gas of isotropic wavepackets.

5.3 Comparison with molecular dynamics

We now compare the non-interacting theory developed in the previous section with fully interacting MD data for warm dense hydrogen. The full model being employed, including confining and Pauli potentials, corresponds to the fully-ionised model specified in the previous chapter. The long-range Coulombic interactions are computed in reciprocal space according to the Ewald treatment in Reference [46]. A timestep of 5×10^{-5} fs and a real-space cutoff for Pauli interactions of $12\,a_0$ ensure stable energy conservation. Results are presented for a

Wigner–Seitz radius of $r_s = 2$ and a degeneracy parameter of $\theta = k_B T/E_F = 1$, where E_F is the Fermi energy. Width distribution data are time-averaged over snapshots that encompass a 25 fs period.

5.3.1 Markov chain Monte Carlo

To compute the width distributions for the non-interacting statistical theory of anisotropic wavepackets, we sample $\boldsymbol{\ell} = (\ell_1, \ell_2, \ell_3)$ from Eq. (5.2.9) using a Markov chain Monte Carlo (MCMC) sampling routine. Specifically, to generate samples from the target density, we employ the *random-walk Metropolis* algorithm [152–154]. At each step the algorithm proposes a move in parameter space and then accepts or rejects it according to the Metropolis rule. Concretely, starting from an initial state $\boldsymbol{\ell}^{(0)}$, the algorithm iterates the following steps:

1. Propose a new point $\boldsymbol{\ell}^{\text{prop}} = \boldsymbol{\ell}^{(t)} + \boldsymbol{\eta}$, where $\boldsymbol{\eta} \sim \mathcal{N}(\mathbf{0},\, \sigma^2 I)$.

2. Compute the log of the unnormalised target density at the proposal and the current state, and form the acceptance probability

$$\alpha = \min\Big\{1,\, \exp\Big[\log f_{\boldsymbol{\ell}}^{\text{ani}}(\boldsymbol{\ell}^{\text{prop}}) - \log f_{\boldsymbol{\ell}}^{\text{ani}}(\boldsymbol{\ell}^{(t)})\Big]\Big\}.$$

3. With probability α, accept the proposal and set $\boldsymbol{\ell}^{(t+1)} = \boldsymbol{\ell}^{\text{prop}}$; otherwise, keep the current state $\boldsymbol{\ell}^{(t+1)} = \boldsymbol{\ell}^{(t)}$.

Evaluating the density in log space prevents numerical underflow and converts products into sums, which is more numerically stable.

The Gaussian proposal width σ is varied to yield a reasonable acceptance rate of around 0.3. Each run consists of 2×10^6 iterations, with the first 10^5 discarded as burn-in and every 20th sample retained (thinning) for analysis. The retained states are transformed to widths $\sigma_i = \sqrt{\ell_i}$, from which we construct the single-particle distribution P_σ^{ani} and the averaged distribution $P_{\bar{\sigma}}^{\text{ani}}$. Performing multiple independent runs confirmed consistent acceptance rates and stable estimates of the width PDFs.

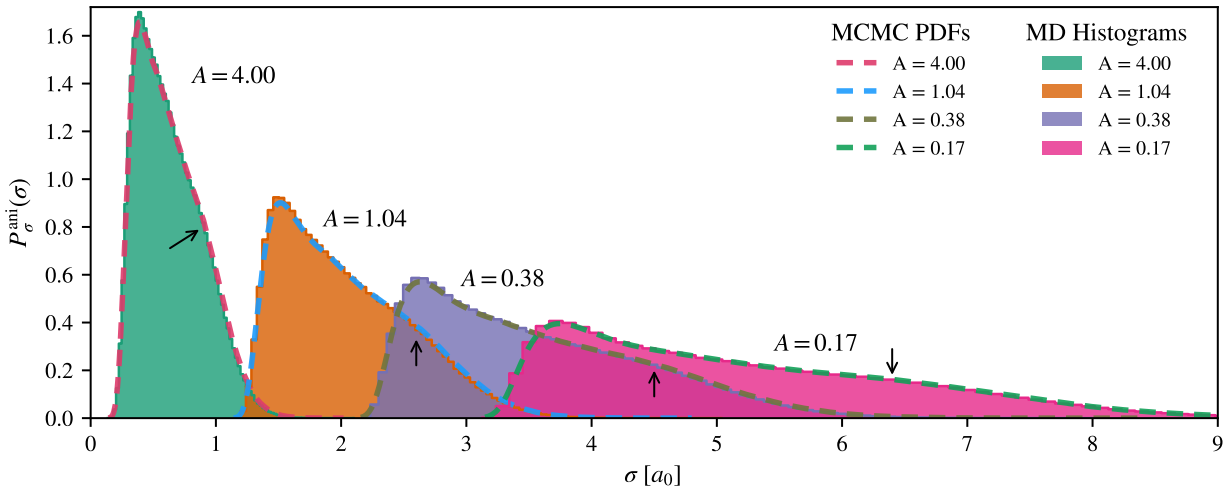

Figure 5.1: Marginal width distribution functions for an anisotropic wavepacket plasma at $r_s = 2$ and $\theta = 1$ for different confining potentials. Excluding the $A = 4.00\,\mathrm{Ha/a_0^2}$ case, each curve is shifted by $1\,a_0$ relative to the curve to its left for clarity. The histograms correspond to molecular dynamics (MD) results in the microcanonical ensemble, while the dashed lines correspond to Markov chain Monte Carlo (MCMC) sampling of Eq. (5.2.9). Arrows indicate the shoulder feature discussed in the main text. The simulations are performed within a cubic box of side length $L = 52.5\,a_0$. Hartree atomic units are used in the legend.

5.3.2 Model comparison

Figure 5.1 shows the sampled distributions compared to the interacting MD simulations specified in the previous subsection for different values of the confining strength A. The agreement between the classical statistical theory and width distributions obtained from interacting simulations is remarkable. Additionally, a shoulder feature is observed in the tail of each distribution, as indicated by the arrows in Figure 5.1. This feature arises from the eigenvalue difference term, $\prod_{1\leq p<q\leq 3}|\ell_q - \ell_p|$, present in the marginal distribution over eigenvalues, which appears in the second product of Equation (5.2.9). This *eigenvalue repulsion* suppresses configurations with a similar spatial extent in each diagonalized spatial dimension, because fewer distinct covariance matrices Σ correspond to such points. This term directly originates from the rotational degrees of freedom in the model, which provide additional relaxation pathways. The equivalence between the width distribution from the statistical theory and from the interacting system provides direct evidence that the effective interactions of the model are mediated by the classical statistics of the wavepacket Hamiltonian $\mathcal{H}^{\mathrm{WP}}$.

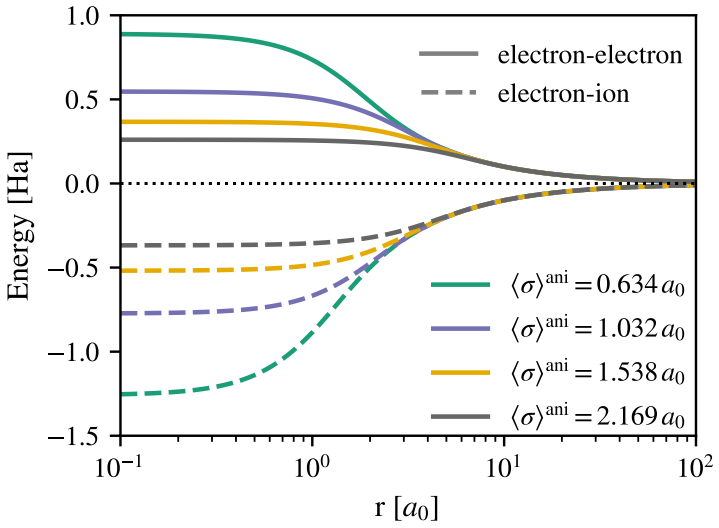

Figure 5.2: Effective interparticle Coulomb interactions based on the mean width of the width distributions plotted in Figure 5.1.

To demonstrate this point, we plot effective interparticle interactions in Figure 5.2. These interactions are computed from the Coulomb interactions of an isotropic Gaussian with a width given by the mean of the corresponding distributions in Figure 5.1. For narrow wavepackets, the interparticle Coulomb interaction is stronger at small separations because the charge distribution is more localised. For larger separations relative to the wavepacket width, the pair potentials asymptote to the Coulomb potential. At this condition, full ionisation is expected, and the effect of interactions has little impact on the width PDFs. A comparison between the isotropic and anisotropic restricted wavefunctions is presented in Figure 5.3. Panel (a) shows the isotropic distribution $f_\sigma(\sigma)$ computed with both MD and MCMC techniques, alongside the PDF for the average width of an anisotropic wavepacket $P_{\bar{\sigma}}^{\mathrm{ani}}$. For an equivalent confining potential, the average extent of the anisotropic wavepacket is significantly larger. Panel (b) depicts the corresponding marginal distribution over individual width variables, which exhibits a prominent tail extending beyond $6\,a_0$ and a shoulder feature. Figure 5.3 also demonstrates that the width of each anisotropic wavepacket is underestimated by the mode of the isotropic distribution. While emphasising the role of the underlying classical statistics, this comparison elucidates the difference in the two restricted wavefunctions. The isotropic wavefunctions

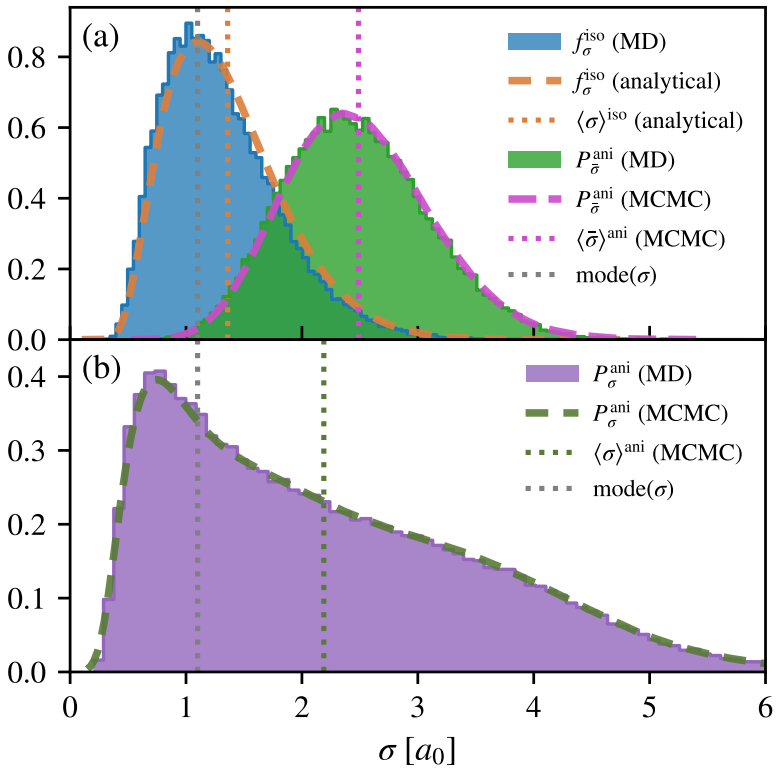

Figure 5.3: Comparison between isotropic and anisotropic width distribution functions at $r_s = 2, \theta = 1$ for a confining potential of $A = 0.17\,\text{Ha}/\text{a}_0^2$. (a) Average width distribution functions for the isotropic and anisotropic models. (b) Distribution of individual width variables in the anisotropic model. The grey dashed line indicates the modal width of the isotropic model given by Equation (5.2.19). The mean values of each distribution are also plotted, with the isotropic case given by Equation (5.2.17), and the anisotropic case calculated numerically.

are considerably more localised for a given confining potential. This is likely explained by additional rotational degrees of freedom present in the anisotropic wavepacket ansatz, which provide additional relaxation pathways in the dynamics and manifest as eigenvalue repulsion. The stronger localisation in the isotropic ansatz for a given confining strength means it will have stronger electron-electron and electron-ion interactions, explaining weaker correlations observed for the anisotropic ansatz in a previous comparison [46], albeit for a different form of the confining potential.

5.4 Chapter Summary

WPMD-based simulations can capture the concurrent time evolution of thousands of coupled ions and electrons. However, applications in plasma physics require the use of a confining potential to appropriately constrain the electron widths. In this chapter, a method by which the effect of the confining potential may be predicted *a priori* for both isotropic and anisotropic variants of WPMD has been introduced. From a practical perspective, this may allow confinement strength heuristics, such as those discussed in Refs. [135, 136], to be developed and then applied, without the need to explicitly scan this parameter using MD simulations to find a suitable choice, as was required in Chapter 4. Additionally, the distribution of electronic widths has been investigated within a classical statistical theory. The comparison of two wavepacket models reveals that, even under equivalent confining potentials, they exhibit different mean widths and therefore different effective Coulomb interactions. This finding accounts for the structural differences previously reported between these models in the warm dense matter regime [46]. The results presented here could also be extended to the case of a global external confining potential and therefore used to predict its impact on the equilibrium density profile [137].

From a theoretical perspective, we have demonstrated that the distribution of variables in wavepacket models is closely connected to the statistical properties of the underlying classical Hamiltonian $\mathcal{H}^{\mathrm{WP}}$. For the model to yield correct effective pairwise interactions—which are

known from quantum statistical considerations to be Coulomb-like at large separations and finite at small separations in weakly-coupled, fully-ionised plasmas [89]—it should relax to a non-divergent width distribution. As $A \to 0$ in either the anisotropic or isotropic case, the average width diverges and the distribution functions themselves, Eqs. (5.2.9) and (5.2.14), become unnormalizable. This observation establishes the confining potential as an essential ingredient for enforcing the correct behaviour in weakly-coupled regimes. Similar models, such as those used for nuclear collisions, often address this feature by fixing the wavepacket width directly [145].

In fully-ionised warm dense systems, as studied here, a significant fraction of the electrons are expected to be in spatially-extended states. However, a fully delocalised Gaussian wavepacket will effectively cease to interact with the system and has no mechanism to relocalise. Therefore, by regulating the model through the choice of an appropriate confining potential, physically meaningful results can be obtained [36, 48, 137].

Chapter 6

Conclusion

6.1 Summary

This thesis has investigated the structure and ionisation behaviour of dense, partially-ionised hydrogen using scalable molecular dynamics (MD) frameworks formulated within the chemical picture. The central objective has been the development and assessment of dynamic electron models capable of describing warm dense matter (WDM) across regimes where both Coulomb coupling and quantum effects are important, while remaining computationally tractable for large-scale simulations.

Chapter 2 established the theoretical and numerical foundation for the work. The principles of classical molecular dynamics were reviewed, with particular emphasis on thermodynamic integration as a tool for computing free energies from simulation data. A detailed derivation of electrostatic interactions under periodic boundary conditions was presented, culminating in a systematic derivation and practical formulation of the Ewald potential for Coulomb systems. One- and two-component plasma models were then discussed, alongside quantum statistical potentials and wave packet molecular dynamics (WPMD). This chapter provided the conceptual and technical introduction to MD techniques for the study of WDM.

In Chapter 3, the Coulomb one-component plasma (OCP) framework was extended to include bound electrons within the chemical picture. A free-energy minimisation procedure, incorporating thermodynamic integration, was developed to determine the ionisation state self-consistently. This enabled quantitative exploration of ionisation potential depression and pressure ionisation within OCP-inspired models. The results demonstrated how interaction effects modify the equilibrium ionisation relative to ideal and reference systems, and highlighted the sensitivity of ionisation behaviour to the chosen interaction model. The framework established here provides a systematic and transferable route to computing ionisation equilibria within molecular dynamics models applicable to dense plasmas.

Chapter 4 introduced an explicit bound-state extension of an existing WPMD model,

enabling a combined dynamic treatment of free electrons and a physically motivated, adiabatic treatment of bound electrons. By combining the bound-WPMD model with the free-energy minimisation approach developed in Chapter 3, the ionisation state was determined self-consistently within a fully dynamical electron model. Application to dense, partially-ionised hydrogen allowed structural properties, in this case radial distribution functions, to be compared directly with available path integral Monte Carlo reference data. A key outcome was that incorporating bound electrons reduces the sensitivity of structural predictions to the confining potential at partially-ionised conditions and improves agreement with reference data when physically motivated constraints are imposed on free-electron spatial extent. This chapter also represents the first explicit treatment of ionisation equilibria using direct free-energy minimisation within a wavepacket-based dynamic electron MD framework.

Chapter 5 addressed more fundamental aspects of WPMD by developing a classical statistical theory for the distribution of electronic width variables. Analytical predictions for isotropic and anisotropic Gaussian wavepacket ansätze were derived and compared with interacting MD data. Good agreement confirmed that the equilibrium width distribution is governed by the underlying classical Hamiltonian structure. Crucially, it was shown that a confining potential is essential to ensure a normalisable width distribution and to recover physically correct effective Coulomb interactions in weakly-coupled regimes. The comparison between isotropic and anisotropic variants clarified how differences in localisation lead to distinct effective interactions and, consequently, different structural correlations. Since the confining potential regulates the effective electron–ion interactions entering the free energy, it ultimately influences the self-consistent ionisation state obtained within the chemical-picture framework. This analysis provides both practical guidance for selecting confinement parameters and deeper theoretical insight into the limitations and capabilities of wavepacket-based plasma models.

Taken together, the work presented in this thesis establishes a coherent framework for modelling partially-ionised warm dense hydrogen using scalable molecular dynamics techniques. By combining free-energy-based ionisation calculations with explicit dynamic electron treatments,

it provides a diverse set of computational approaches that bridge the gap between simplified plasma models and first-principles approaches. The results demonstrate that, with appropriate physical constraints and self-consistent ionisation treatment, wavepacket-based MD methods can reproduce key structural features of dense hydrogen while remaining computationally efficient. This provides a promising foundation for future extensions to more complex materials, transport properties, and multiscale modelling applications in high-energy-density physics.

6.2 Future work

The models developed in this thesis provide a scalable and physically transparent framework for studying partially-ionised warm dense hydrogen. The application of these models is first considered in the context of the multiscale ICF simulations introduced in Chapter 1. Additionally, several natural model extensions and refinements can be identified which would further enhance both their predictive capability and their range of applicability. These are split into two subsequent sections that correspond to future developments based on one-component and two-component models.

6.2.1 Application to multiscale modelling

The methods developed in this thesis could provide atomistically informed material-property data for radiation-hydrodynamics simulations of inertial-confinement-fusion implosions. In particular, equilibrium ionisation states could be calculated over a grid of density and temperature conditions using free-energy minimisation. The resulting data could then be tabulated or parameterised for use within a hydrodynamics code, replacing or calibrating simplified ionisation prescriptions while retaining the effects of strong coupling and bound-state interactions. For hydrogen, the mean ionisation determines the neutral and ion fractions completely; extensions to higher-Z materials or mixtures would require calculation of a full charge-state distribution.

Transport properties could be obtained within the same microscopic framework. After

determining the equilibrium ionisation state, trajectories generated at that state could be used to calculate transport coefficients from time-correlation functions. One-component models would be most directly applicable to ionic diffusion and viscosity, whereas bound-WPMD could in principle provide both ionic and electronic transport properties, together with electron–ion coupling. Additionally, studying the sensitivity of these properties to ionisation at fixed density and temperature would allow further development of reduced models.

Predictions from bound-WPMD would nevertheless remain sensitive to the confining potential. Since confinement regulates the electronic width distribution and hence the effective electron–electron and electron–ion interactions, it may influence the equilibrium ionisation, screening, conductivity and electron–ion relaxation. A useful future study would therefore calculate ionisation and transport over a physically plausible range of confinement parameters. The statistical width theory developed in Chapter 5 could reduce the numerical cost of this procedure, while comparison with first-principles or experimental data could be used to constrain the confinement model or quantify its associated uncertainty.

The principal computational advantage is that the atomistic calculations would be performed only when constructing the material-property tables. When compared with first-principles methods, the reduced computational expense of the models, as discussed in Sections 3.4.2 and 4.4.2, would allow feasible exploration over a larger range of conditions. The subsequent table interpolation within each hydrodynamic cell and timestep would be inexpensive. The favourable scaling of the molecular-dynamics models also permits larger systems and longer trajectories than are generally accessible to first-principles methods, which is particularly valuable for converging transport calculations. The main limitations are the restricted thermodynamic range studied, the simplified interaction models and the assumption of equilibrium ionisation, although nonequilibrium studies may also be investigated using these models. Care would also be required to maintain consistency between the ionisation, equation-of-state and transport data supplied to the hydrodynamic model.

6.2.2 One-component models

The contribution of Chapter 3 lies primarily in the development of the ionisation calculation framework based on free-energy minimisation. The specific models employed in that chapter were deliberately simplified and could be further refined. Possible extensions include the incorporation of electronic screening of both ions and bound states, as well as the explicit treatment of bound-state polarisation. Inspiration may be drawn from established chemical-picture methods for light elements [70, 95, 111, 112], which employed semi-analytical techniques to compute the free energy. Implementing similar approaches within a molecular dynamics framework would allow interparticle interactions to be treated explicitly and non-perturbatively through direct simulation.

Warm dense matter remains a particularly challenging regime to model, and modern equation-of-state tables typically rely on parameterisations of first-principles calculations in this domain [6]. In contrast, chemical-picture models continue to be employed at lower densities [155], where interaction effects can be treated as perturbative corrections to bound-state wavefunctions. The ionisation calculation framework developed in this thesis provides a systematic route for constructing and testing models across both weakly and strongly coupled regimes.

Future work could therefore focus on developing interaction models calibrated against benchmark first-principles calculations in the warm dense regime. Once validated, such models could be used to explore properties that remain uncertain or computationally inaccessible. A particularly relevant example is ion transport, since transport coefficients depend sensitively on the charge-state distribution [156]. If transport coefficient tables for WDM were to be constructed, MD-based chemical models of this type could provide a consistent connection between the low-density limit—where first-principles approaches may become computationally prohibitive—and the warm dense regime.

6.2.3 Wave packet molecular dynamics

The contributions of Chapters 4 and 5 centre on the study and development of wave packet molecular dynamics (WPMD).

The bound-WPMD model presented in Chapter 4 may be extended in several directions. One possible route is the inclusion of stochastic transitions between bound and free orbitals, allowing the wavefunction to explore multiple restricted-state manifolds. Such transitions may be motivated within the WPMD formalism itself [93, 145], or informed by plasma-physics considerations [99]. Introducing branching processes would enable dynamic ionisation and recombination beyond a strictly deterministic variational evolution, allowing the state to explore multiple submanifolds within the associated Hilbert space.

A second direction concerns the use of more elaborate wavefunctions through the introduction of additional chemical species or enriched basis sets. The Gaussian decomposition of the orbitals could be generalised to a complete basis including Cartesian Gaussian functions,

$$g_{n,m,l}(x,y,z) \sim x^n y^m z^l \exp\left[-\alpha r^2\right], \tag{6.2.1}$$

thereby permitting anisotropic electronic structure. Such extensions would allow, for example, a more realistic description of the formation of molecular ions (H_2^+) and molecules (H_2). The inclusion of time-dependent amplitudes could further enable the simulation of vibrational molecular dynamics within interacting WDM systems, as well as explicitly time-dependent ionisation and recombination processes.

The statistical analysis presented in Chapter 5 highlights more fundamental limitations of restricted wavepacket descriptions applied to many-body Coulomb systems. By reducing the electronic subsystem to a finite set of variational parameters and coupling it to classical ions, the long-time behaviour becomes governed by classical Hamiltonian statistics in the restricted phase space. Although the time-dependent variational principle yields short-time dynamics that approximate Schrödinger evolution, equilibrium properties are determined by the statistical mechanics of the classical Hamiltonian $\mathcal{H}^{\mathrm{WP}}$.

This limitation is reflected, for example, in the scaling of the electronic heat capacity with the number of variational degrees of freedom [46, 124, 157]. In a physically consistent model, one would instead expect Boltzmann weights over the adiabatic energy eigenstates of $\hat{H}_e(\{\boldsymbol{R}_I\})$, i.e. the emergence of proper quantum statistics. Within a restricted wave-packet description, this would require that long-time averages of projections onto the electronic energy eigenbasis reproduce the corresponding quantum distribution.

Two broad strategies have been explored in the literature to address these limitations. The first augments Hamiltonian wavepacket dynamics with stochastic transitions in phase space. Such transitions break the exact conservation laws of the classical Hamiltonian and modify the statistical exploration of phase space. This approach has proven successful in nuclear collision models, where stochastic branching and decoherence processes are introduced to overcome mean-field limitations of Hartree or Slater-determinant descriptions [93, 145, 158, 159]. Related ideas appear in non-adiabatic chemical dynamics, where surface-hopping schemes reproduce correct statistical behaviour in situations where Ehrenfest dynamics fails [160–162].

The second strategy involves modifying the dynamics through thermostatting procedures designed to enforce sampling of quantum statistical distributions. While quantum-consistent thermostats have been proposed in both low- [163] and high-temperature [164] regimes, existing implementations remain largely restricted to small systems or simplified models.

Developing dynamical schemes that reconcile restricted wavepacket dynamics with quantum statistical behaviour remains an open and challenging problem. Progress in this direction would substantially strengthen the theoretical foundations of WPMD for applications in warm dense matter.

References

[1] I. Langmuir, Oscillations in ionized gases, Proceedings of the National Academy of Sciences of the United States of America **14**, 627–637 (1928).

[2] J. Vorberger, F. Graziani, D. Riley, A. D. Baczewski, I. Baraffe, M. Bethkenhagen, S. Blouin, M. P. Böhme, M. Bonitz, M. Bussmann, A. Casner, W. Cayzac, P. Celliers, G. Chabrier, N. Chamel, D. Chapman, M. Chen, J. Clérouin, G. Collins, F. Coppari, T. Döppner, T. Dornheim, L. B. Fletcher, D. O. Gericke, S. Glenzer, A. F. Goncharov, G. Gregori, S. Hamel, S. B. Hansen, N. J. Hartley, S. Hu, O. A. Hurricane, V. V. Karasiev, J. J. Kas, B. Kettle, T. Kluge, M. D. Knudson, A. Kononov, Z. Konôpková, D. Kraus, A. Kritcher, S. Malko, G. Massacrier, B. Militzer, Z. A. Moldabekov, M. S. Murillo, B. Nagler, N. Nettelmann, P. Neumayer, B. K. Ofori-Okai, I. I. Oleynik, M. Preising, A. Pribram-Jones, T. Ramazanov, A. Ravasio, R. Redmer, B. Rethfeld, A. P. L. Robinson, G. Röpke, F. Soubiran, C. E. Starrett, G. Steinle-Neumann, P. A. Sterne, S. Tanaka, A. P. Thompson, S. B. Trickey, T. Vinci, S. M. Vinko, L. Wang, A. J. White, T. G. White, U. Zastrau, E. Zurek, and P. Tolias, Roadmap for warm dense matter physics, Plasma Physics and Controlled Fusion **68**, 073501 (2026).

[3] R. Betti and O. A. Hurricane, Inertial-confinement fusion with lasers, Nature Physics **12**, 435–448 (2016).

[4] H. Abu-Shawareb et al. (Indirect Drive ICF Collaboration), Lawson criterion for ignition exceeded in an inertial fusion experiment, Phys. Rev. Lett. **129**, 075001 (2022).

[5] O. A. Hurricane, P. K. Patel, R. Betti, D. H. Froula, S. P. Regan, S. A. Slutz, M. R. Gomez, and M. A. Sweeney, Physics principles of inertial confinement fusion and u.s. program overview, Rev. Mod. Phys. **95**, 025005 (2023).

[6] B. Militzer, F. González-Cataldo, S. Zhang, K. P. Driver, and F. Soubiran, First-principles equation of state database for warm dense matter computation, Phys. Rev. E **103**, 013203 (2021).

[7] S. X. Hu, B. Militzer, V. N. Goncharov, and S. Skupsky, First-principles equation-of-state table of deuterium for inertial confinement fusion applications, Phys. Rev. B **84**, 224109 (2011).

[8] B. M. Haines, Charged particle transport coefficient challenges in high energy density plasmas, Physics of Plasmas **31**, 050501 (2024).

[9] S. X. Hu, L. A. Collins, T. R. Boehly, Y. H. Ding, P. B. Radha, V. N. Goncharov, V. V. Karasiev, G. W. Collins, S. P. Regan, and E. M. Campbell, A review on ab initio studies of static, transport, and optical properties of polystyrene under extreme conditions for inertial confinement fusion applications, Physics of Plasmas **25**, 056306 (2018).

[10] T. Guillot, The interiors of giant planets: models and outstanding questions, Annual Review of Earth and Planetary Sciences **33**, 493–530 (2005).

[11] G. Chabrier, D. Saumon, and A. Y. Potekhin, Dense plasmas in astrophysics: from giant planets to neutron stars, Journal of Physics A: Mathematical and General **39**, 4411–4419 (2006).

[12] D. Saumon, S. Blouin, and P.-E. Tremblay, Current challenges in the physics of white dwarf stars, Physics Reports **988**, 1–63 (2022).

[13] P. Haensel, A. Y. Potekhin, and D. G. Yakovlev, eds., *Neutron stars 1: equation of state and structure*, Vol. 326, Astrophysics and Space Science Library (Springer, New York, NY, 2007).

[14] N. Nettelmann, B. Holst, A. Kietzmann, M. French, R. Redmer, and D. Blaschke, Ab initio equation of state data for hydrogen, helium, and water and the internal structure of jupiter, The Astrophysical Journal **683**, 1217–1228 (2008).

[15] L. G. Stanton and M. S. Murillo, Ionic transport in high-energy-density matter, Phys. Rev. E **93**, 043203 (2016).

[16] T. J. Callow, E. Kraisler, and A. Cangi, Improved calculations of mean ionization states with an average-atom model, Phys. Rev. Res. **5**, 013049 (2023).

[17] O. Ciricosta, S. M. Vinko, H.-K. Chung, B.-I. Cho, C. R. D. Brown, T. Burian, J. Chalupský, K. Engelhorn, R. W. Falcone, C. Graves, V. Hájková, A. Higginbotham, L. Juha, J. Krzywinski, H. J. Lee, M. Messerschmidt, C. D. Murphy, Y. Ping, D. S. Rackstraw, A. Scherz, W. Schlotter, S. Toleikis, J. J. Turner, L. Vysin, T. Wang, B. Wu, U. Zastrau, D. Zhu, R. W. Lee, P. Heimann, B. Nagler, and J. S. Wark, Direct measurements of the ionization potential depression in a dense plasma, Phys. Rev. Lett. **109**, 065002 (2012).

[18] S. G. Brush, H. L. Sahlin, and E. Teller, Monte carlo study of a one-component plasma. I, The Journal of Chemical Physics **45**, 2102–2118 (1966).

[19] M. Bonitz, *Quantum kinetic theory* (Springer International Publishing, 2015).

[20] T. Dornheim, S. Groth, and M. Bonitz, The uniform electron gas at warm dense matter conditions, Physics Reports **744**, 1–86 (2018).

[21] M. Bonitz, J. Vorberger, M. Bethkenhagen, M. P. Böhme, D. M. Ceperley, A. Filinov, T. Gawne, F. Graziani, G. Gregori, P. Hamann, S. B. Hansen, M. Holzmann, S. X. Hu, H. Kählert, V. V. Karasiev, U. Kleinschmidt, L. Kordts, C. Makait, B. Militzer, Z. A. Moldabekov, C. Pierleoni, M. Preising, K. Ramakrishna, R. Redmer, S. Schwalbe, P. Svensson, and T. Dornheim, Toward first principles-based simulations of dense hydrogen, Physics of Plasmas **31**, 110501 (2024).

[22] E. L. Pollock and J. P. Hansen, Statistical mechanics of dense ionized matter. ii. equilibrium properties and melting transition of the crystallized one-component plasma, Phys. Rev. A **8**, 3110–3122 (1973).

[23] R. Pathria and P. D. Beale, "8 - ideal fermi systems", in *Statistical mechanics*, edited by R. Pathria and P. D. Beale, 4th ed. (Academic Press, 2022), pp. 247–290.

[24] P. Svensson, Novel modelling techniques for charged many-body systems with quantum and relativistic effects, PhD thesis (Worcester College, University of Oxford, Oxford, 2024).

[25] B. Militzer and D. M. Ceperley, Path integral monte carlo calculation of the deuterium hugoniot, Phys. Rev. Lett. **85**, 1890–1893 (2000).

[26] B. Militzer, Path integral monte carlo simulations of hot dense hydrogen, PhD thesis (University of Illinois at Urbana-Champaign, 2000).

[27] J. P. Sauppe, Y. Lu, P. Tzeferacos, A. C. Reyes, S. Palaniyappan, K. A. Flippo, S. Li, and J. L. Kline, On the importance of three-dimensional modeling for high-energy-density physics experiments, Physics of Plasmas **30**, 062707 (2023).

[28] M. M. Marinak, G. D. Kerbel, N. A. Gentile, O. Jones, D. Munro, S. Pollaine, T. R. Dittrich, and S. W. Haan, Three-dimensional hydra simulations of national ignition facility targets, Physics of Plasmas **8**, 2275–2280 (2001).

[29] J. Gaffney, S. Hu, P. Arnault, A. Becker, L. Benedict, T. Boehly, P. Celliers, D. Ceperley, O. Čertík, J. Clérouin, G. Collins, L. Collins, J.-F. Danel, N. Desbiens, M. Dharma-wardana, Y. Ding, A. Fernandez-Pañella, M. Gregor, P. Grabowski, S. Hamel, S. Hansen, L. Harbour, X. He, D. Johnson, W. Kang, V. Karasiev, L. Kazandjian, M. Knudson, T. Ogitsu, C. Pierleoni, R. Piron, R. Redmer, G. Robert, D. Saumon, A. Shamp, T. Sjostrom, A. Smirnov, C. Starrett, P. Sterne, A. Wardlow, H. Whitley, B. Wilson, P. Zhang, and E. Zurek, A review of equation-of-state models for inertial confinement fusion materials, High Energy Density Physics **28**, 7–24 (2018).

[30] J. LeVan and S. D. Baalrud, Foundations of magnetohydrodynamics, Physics of Plasmas **32**, 070901 (2025).

[31] A. Ng, Outstanding questions in electron–ion energy relaxation, lattice stability, and dielectric function of warm dense matter, International Journal of Quantum Chemistry **112**, 150–160 (2012).

[32] J. Simoni and J. Daligault, First-principles determination of electron-ion couplings in the warm dense matter regime, Phys. Rev. Lett. **122**, 205001 (2019).

[33] M. Luo, C. Heaton, Y. Wang, D. Plummer, M. Fitzgerald, F. Miniati, S. M. Vinko, and G. Gregori, Time-embedded convolutional neural networks for modeling plasma heat transport, Phys. Rev. E **113**, 035303 (2026).

[34] J. P. Mithen, J. Daligault, and G. Gregori, Extent of validity of the hydrodynamic description of ions in dense plasmas, Phys. Rev. E **83**, 015401(R) (2011).

[35] G. Gregori, S. H. Glenzer, W. Rozmus, R. W. Lee, and O. L. Landen, Theoretical model of x-ray scattering as a dense matter probe, Phys. Rev. E **67**, 026412 (2003).

[36] P. Svensson, Y. Aziz, T. Dornheim, S. Azadi, P. Hollebon, A. Skelt, S. M. Vinko, and G. Gregori, Modeling of warm dense hydrogen via explicit real-time electron dynamics: dynamic structure factors, Phys. Rev. E **110**, 055205 (2024).

[37] D. Marx and J. Hutter, *Ab initio molecular dynamics: basic theory and advanced methods* (Cambridge University Press, 2009).

[38] N. D. Mermin, Thermal properties of the inhomogeneous electron gas, Phys. Rev. **137**, A1441–A1443 (1965).

[39] E. Runge and E. K. U. Gross, Density-functional theory for time-dependent systems, Phys. Rev. Lett. **52**, 997–1000 (1984).

[40] A. D. Baczewski, L. Shulenburger, M. P. Desjarlais, S. B. Hansen, and R. J. Magyar, X-ray thomson scattering in warm dense matter without the chihara decomposition, Phys. Rev. Lett. **116**, 115004 (2016).

[41] L. J. Stanek, A. Kononov, S. B. Hansen, B. M. Haines, S. X. Hu, P. F. Knapp, M. S. Murillo, L. G. Stanton, H. D. Whitley, S. D. Baalrud, L. J. Babati, A. D. Baczewski, M. Bethkenhagen, A. Blanchet, R. C. Clay III, K. R. Cochrane, L. A. Collins, A. Dumi, G. Faussurier, M. French, Z. A. Johnson, V. V. Karasiev, S. Kumar, M. K. Lentz, C. A. Melton, K. A. Nichols, G. M. Petrov, V. Recoules, R. Redmer, G. Röpke, M. Schörner, N. R. Shaffer, V. Sharma, L. G. Silvestri, F. Soubiran, P. Suryanarayana, M. Tacu, J. P. Townsend, and A. J. White, Review of the second charged-particle transport coefficient code comparison workshop, Physics of Plasmas **31**, 052104 (2024).

[42] M. French, G. Röpke, M. Schörner, M. Bethkenhagen, M. P. Desjarlais, and R. Redmer, Electronic transport coefficients from density functional theory across the plasma plane, Phys. Rev. E **105**, 065204 (2022).

[43] P. Mabey, S. Richardson, T. G. White, L. B. Fletcher, S. H. Glenzer, N. J. Hartley, J. Vorberger, D. O. Gericke, and G. Gregori, A strong diffusive ion mode in dense ionized matter predicted by langevin dynamics, Nature Communications **8**, 14125 (2017).

[44] P. Svensson, P. Hollebon, D. Plummer, S. M. Vinko, and G. Gregori, Modeling of warm dense hydrogen via explicit real-time electron dynamics: electron transport properties, Phys. Rev. E **111**, 045208 (2025).

[45] D. Plummer, P. Svensson, D. O. Gericke, P. Hollebon, S. M. Vinko, and G. Gregori, Ionization calculations using classical molecular dynamics, Phys. Rev. E **111**, 015204 (2025).

[46] P. Svensson, T. Campbell, F. Graziani, Z. Moldabekov, N. Lyu, V. S. Batista, S. Richardson, S. M. Vinko, and G. Gregori, Development of a new quantum trajectory molecular dynamics framework, Philosophical Transactions of the Royal Society A: Mathematical, Physical and Engineering Sciences **381**, 20220325 (2023).

[47] T. Dornheim, S. Schwalbe, M. P. Böhme, Z. A. Moldabekov, J. Vorberger, and P. Tolias, Ab initio path integral monte carlo simulations of warm dense two-component systems without fixed nodes: structural properties, The Journal of Chemical Physics **160**, 164111 (2024).

[48] D. Plummer, P. Svensson, W. Jasniak, P. Hollebon, S. M. Vinko, and G. Gregori, Modeling partially ionized dense plasma using wavepacket molecular dynamics, Phys. Rev. E **113**, 045206 (2026).

[49] D. Plummer, P. Svensson, W. Jasniak, P. Hollebon, S. M. Vinko, and G. Gregori, Statistical theory of electronic degrees of freedom in wave packet molecular dynamics, Phys. Rev. E **114**, 015219 (2026).

[50] D. Frenkel and B. Smit, *Understanding molecular simulation*, 2nd ed. (Academic Press, San Diego, 2002).

[51] M. P. Allen and D. J. Tildesley, *Computer simulation of liquids*, 2nd ed. (Oxford University Press, Oxford, 2017).

[52] J.-P. Hansen and I. R. McDonald, *Theory of simple liquids*, 4th ed. (Academic Press, Oxford, 2013).

[53] D. C. Rapaport, *The art of molecular dynamics simulation*, 2nd ed. (Cambridge University Press, 2004).

[54] S. Nose, A molecular dynamics method for simulations in the canonical ensemble, Molecular Physics **52**, 255–268 (1984).

[55] W. G. Hoover, Canonical dynamics: equilibrium phase-space distributions, Physical Review A **31**, 1695–1697 (1985).

[56] H. C. Andersen, Molecular dynamics simulations at constant pressure and/or temperature, Journal of Chemical Physics **72**, 2384–2393 (1980).

[57] M. Parrinello and A. Rahman, Polymorphic transitions in single crystals: a new molecular dynamics method, Physical Review Letters **45**, 1196–1199 (1981).

[58] T. C. Beutler, A. E. Mark, R. C. van Schaik, P. R. Gerber, and W. F. van Gunsteren, Avoiding singularities and numerical instabilities in free energy calculations based on molecular simulations, Chemical Physics Letters **222**, 529–539 (1994).

[59] A. P. Thompson, H. M. Aktulga, R. Berger, D. S. Bolintineanu, W. M. Brown, P. S. Crozier, P. J. in 't Veld, A. Kohlmeyer, S. G. Moore, T. D. Nguyen, R. Shan, M. J. Stevens, J. Tranchida, C. Trott, and S. J. Plimpton, LAMMPS - a flexible simulation tool for particle-based materials modeling at the atomic, meso, and continuum scales, Comp. Phys. Comm. **271**, 108171 (2022).

[60] J. M. Caillol, Numerical simulations of Coulomb systems: A comparison between hyperspherical and periodic boundary conditions, The Journal of Chemical Physics **111**, 6528–6537 (1999).

[61] W. L. Slattery, G. D. Doolen, and H. E. DeWitt, Improved equation of state for the classical one-component plasma, Phys. Rev. A **21**, 2087–2095 (1980).

[62] G. Hummer, L. R. Pratt, and A. E. García, Molecular theories and simulation of ions and polar molecules in water, The Journal of Physical Chemistry A **102**, 7885–7895 (1998).

[63] F. Figueirido, G. S. Del Buono, and R. M. Levy, On finite-size effects in computer simulations using the ewald potential, The Journal of Chemical Physics **103**, 6133–6142 (1995).

[64] D. Hummer and D. Mihalas, The equation of state for stellar envelopes. I - an occupation probability formalism for the truncation of internal partition functions, The Astrophysical Journal **331**, 794–814 (1988).

[65] J. S. Hub, B. L. de Groot, H. Grubmüller, and G. Groenhof, Quantifying artifacts in ewald simulations of inhomogeneous systems with a net charge, Journal of Chemical Theory and Computation **10**, 381–390 (2014).

[66] M. Deserno and C. Holm, How to mesh up ewald sums. i. a theoretical and numerical comparison of various particle mesh routines, The Journal of Chemical Physics **109**, 7678–7693 (1998).

[67] LAMMPS Documentation, LAMMPS Developer Documentation: Parallel Communication (2025).

[68] Z. A. Moldabekov, S. Groth, T. Dornheim, H. Kählert, M. Bonitz, and T. S. Ramazanov, Structural characteristics of strongly coupled ions in a dense quantum plasma, Phys. Rev. E **98**, 023207 (2018).

[69] L. G. Stanton and M. S. Murillo, Unified description of linear screening in dense plasmas, Phys. Rev. E **91**, 033104 (2015).

[70] D. Saumon and G. Chabrier, Fluid hydrogen at high density: pressure ionization, Physical Review A **46**, 2084–2100 (1992).

[71] N. W. Ashcroft and D. Stroud, "Theory of the thermodynamics of simple liquid metals", in *Solid state physics*, Vol. 33, edited by H. Ehrenreich, F. Seitz, and D. Turnbull, Solid State Physics: Advances in Research and Applications (Academic Press, New York, 1978), pp. 1–81.

[72] S. D. Baalrud and J. Daligault, Effective potential theory for transport coefficients across coupling regimes, Phys. Rev. Lett. **110**, 235001 (2013).

[73] J. Clérouin, P. Arnault, C. Ticknor, J. D. Kress, and L. A. Collins, Unified concept of effective one component plasma for hot dense plasmas, Phys. Rev. Lett. **116**, 115003 (2016).

[74] A. Y. Potekhin and G. Chabrier, Equation of state of fully ionized electron-ion plasmas. II. extension to relativistic densities and to the solid phase, Phys. Rev. E **62**, 8554–8563 (2000).

[75] J. P. Hansen, Statistical mechanics of dense ionized matter. I. equilibrium properties of the classical one-component plasma, Phys. Rev. A **8**, 3096–3109 (1973).

[76] J. M. Caillol, Thermodynamic limit of the excess internal energy of the fluid phase of a one-component plasma: a monte carlo study, Journal of Chemical Physics **111**, 6538–6547 (1999).

[77] J.-M. Caillol and D. Gilles, An accurate equation of state for the one-component plasma in the low coupling regime, Journal of Physics A: Mathematical and Theoretical **43**, 105501 (2010).

[78] B. Scheiner and S. D. Baalrud, Testing thermal conductivity models with equilibrium molecular dynamics simulations of the one-component plasma, Phys. Rev. E **100**, 043206 (2019).

[79] J. Daligault, K. Ø. Rasmussen, and S. D. Baalrud, Determination of the shear viscosity of the one-component plasma, Phys. Rev. E **90**, 033105 (2014).

[80] J. Daligault, Liquid-state properties of a one-component plasma, Phys. Rev. Lett. **96**, 065003 (2006).

[81] W. Hubbard and W. Slattery, Statistical mechanics of light elements at high pressure. i. theory and results for metallic hydrogen with simple screening, The Astrophysical Journal **168**, 131–139 (1971).

[82] S. Hamaguchi and R. T. Farouki, Thermodynamics of strongly-coupled Yukawa systems near the one-component-plasma limit. I. Derivation of the excess energy, The Journal of Chemical Physics **101**, 9876–9884 (1994).

[83] J. M. Caillol and D. Gilles, Monte carlo simulations of the yukawa one-component plasma, Journal of Statistical Physics **100**, 933–947 (2000).

[84] K. Wünsch, J. Vorberger, and D. O. Gericke, Ion structure in warm dense matter: benchmarking solutions of hypernetted-chain equations by first-principle simulations, Phys. Rev. E **79**, 010201(R) (2009).

[85] M. S. Murillo, Viscosity estimates of liquid metals and warm dense matter using the yukawa reference system, High Energy Density Physics **4**, 49–57 (2008).

[86] Z. A. Moldabekov, H. Kählert, T. Dornheim, S. Groth, M. Bonitz, and T. S. Ramazanov, Dynamical structure factor of strongly coupled ions in a dense quantum plasma, Phys. Rev. E **99**, 053203 (2019).

[87] R. T. Farouki and S. Hamaguchi, Thermodynamics of strongly-coupled Yukawa systems near the one-component-plasma limit. II. Molecular dynamics simulations, The Journal of Chemical Physics **101**, 9885–9893 (1994).

[88] M. A. Gigosos, D. González-Herrero, N. Lara, R. Florido, A. Calisti, S. Ferri, and B. Talin, Classical molecular dynamics simulations of hydrogen plasmas and development of an analytical statistical model for computational validity assessment, Phys. Rev. E **98**, 033307 (2018).

[89] A. V. Filinov, V. O. Golubnychiy, M. Bonitz, W. Ebeling, and J. W. Dufty, Temperature-dependent quantum pair potentials and their application to dense partially ionized hydrogen plasmas, Phys. Rev. E **70**, 046411 (2004).

[90] G. S. Demyanov and P. R. Levashov, Molecular dynamics of nondegenerate hydrogen plasma using improved kelbg pseudopotential with electron thermal de broglie wavelength correction, Physics of Plasmas **32**, 123901 (2025).

[91] J. N. Glosli, F. R. Graziani, R. M. More, M. S. Murillo, F. H. Streitz, M. P. Surh, L. X. Benedict, S. Hau-Riege, A. B. Langdon, and R. A. London, Molecular dynamics simulations of temperature equilibration in dense hydrogen, Phys. Rev. E **78**, 025401 (2008).

[92] V. Golubnychiy, M. Bonitz, D. Kremp, and M. Schlanges, Plasmon dispersion of a weakly degenerate nonideal one-component plasma, Contributions to Plasma Physics **42**, 37–41 (2002).

[93] H. Feldmeier and J. Schnack, Molecular dynamics for fermions, Rev. Mod. Phys. **72**, 655–688 (2000).

[94] W. Ebeling, V. E. Fortov, and V. Filinov, *Quantum statistics of dense gases and nonideal plasmas* (Springer International Publishing, 2017).

[95] C. Winisdoerffer and G. Chabrier, Free-energy model for fluid helium at high density, Phys. Rev. E **71**, 026402 (2005).

[96] A. V. Filinov and M. Bonitz, Equation of state of partially ionized hydrogen and deuterium plasma revisited, Physical Review E **108**, 055212 (2023).

[97] D. Saumon and G. Chabrier, Fluid hydrogen at high density: pressure dissociation, Phys. Rev. A **44**, 5122–5141 (1991).

[98] L. D. Landau and E. M. Lifshitz, *Statistical physics*, 3rd ed., Vol. 5, Course of Theoretical Physics (Butterworth-Heinemann, 1980).

[99] W. Ebeling and B. Militzer, Quantum molecular dynamics of partially ionized plasmas, Physics Letters A **226**, 298–304 (1997).

[100] A. S. Onegin, G. S. Demyanov, and P. R. Levashov, Pressure of coulomb systems with volume-dependent long-range potentials, Journal of Physics A: Mathematical and Theoretical **57**, 205002 (2024).

[101] L. M. Fraser, W. M. C. Foulkes, G. Rajagopal, R. J. Needs, S. D. Kenny, and A. J. Williamson, Finite-size effects and coulomb interactions in quantum monte carlo calculations for homogeneous systems with periodic boundary conditions, Phys. Rev. B **53**, 1814–1832 (1996).

[102] S. Blouin and J. Daligault, Direct evaluation of the phase diagrams of dense multicomponent plasmas by integration of the clapeyron equations, Phys. Rev. E **103**, 043204 (2021).

[103] W. Ebeling, H. Hache, and M. Spahn, Thermodynamics of ionization and dissociation in hydrogen plasmas including fluctuations and magnetic fields, Eur. Phys. J. D **23**, 265–272 (2003).

[104] J. Vorberger and D. Gericke, Effective ion–ion potentials in warm dense matter, High Energy Density Physics **9**, 178–186 (2013).

[105] S. Kumar, A. J. Poser, M. Schöttler, U. Kleinschmidt, W. Dietrich, J. Wicht, M. French, and R. Redmer, Ionization and transport in partially ionized multicomponent plasmas: application to atmospheres of hot jupiters, Phys. Rev. E **103**, 063203 (2021).

[106] G. Ecker and W. Kröll, Lowering of the Ionization Energy for a Plasma in Thermodynamic Equilibrium, The Physics of Fluids **6**, 62–69 (1963).

[107] H. R. Griem, High-density corrections in plasma spectroscopy, Phys. Rev. **128**, 997–1003 (1962).

[108] A. de Ruiter, D. Petrov, and C. Oostenbrink, Optimization of alchemical pathways using extended thermodynamic integration, Journal of Chemical Theory and Computation **17**, 56–65 (2021).

[109] C. Ma, Q. Xu, Z. Zhang, K. Wang, Y. Sun, W. Mi, Z. A. Moldabekov, T. Dornheim, J. Vorberger, S. Schwalbe, and X. Shao, Unlocking the power of orbital-free density functional theory to explore the electronic structure under extreme conditions, Matter and Radiation at Extremes **11**, 057205 (2026).

[110] P. Svensson, Private communication (2026).

[111] H. Juranek and R. Redmer, Self-consistent fluid variational theory for pressure dissociation in dense hydrogen, The Journal of Chemical Physics **112**, 3780–3786 (2000).

[112] H. Juranek, R. Redmer, and Y. Rosenfeld, Fluid variational theory for pressure dissociation in dense hydrogen: multicomponent reference system and nonadditivity effects, The Journal of Chemical Physics **117**, 1768–1774 (2002).

[113] G. Zimmerman and R. More, Pressure ionization in laser-fusion target simulation, Journal of Quantitative Spectroscopy and Radiative Transfer **23**, 517–522 (1980).

[114] A. Y. Potekhin, Ionization equilibrium of hot hydrogen plasma, Physics of Plasmas **3**, 4156–4165 (1996).

[115] D. Klakow, C. Toepffer, and P.-G. Reinhard, Hydrogen under extreme conditions, Physics Letters A **192**, 55–59 (1994).

[116] M. Baus and J.-P. Hansen, Statistical mechanics of simple coulomb systems, Physics Reports **59**, 1–94 (1980).

[117] S. A. Khrapak and A. G. Khrapak, Simple thermodynamics of strongly coupled one-component-plasma in two and three dimensions, Physics of Plasmas **21**, 104505 (2014).

[118] N. F. Carnahan and K. E. Starling, Equation of State for Nonattracting Rigid Spheres, The Journal of Chemical Physics **51**, 635–636 (1969).

[119] Z. A. Moldabekov, T. Dornheim, and M. Bonitz, Screening of a test charge in a free-electron gas at warm dense matter and dense non-ideal plasma conditions, Contributions to Plasma Physics **62**, e202000176 (2022).

[120] T. Gawne, T. Campbell, A. Forte, P. Hollebon, G. Perez-Callejo, O. S. Humphries, O. Karnbach, M. F. Kasim, T. R. Preston, H. J. Lee, A. Miscampbell, Q. Y. van den Berg, B. Nagler, S. Ren, R. B. Royle, J. S. Wark, and S. M. Vinko, Investigating mechanisms of state localization in highly ionized dense plasmas, Phys. Rev. E **108**, 035210 (2023).

[121] T. Gawne, S. M. Vinko, and J. S. Wark, Quantifying ionization in hot dense plasmas, Physical Review E **109**, 023201 (2024).

[122] M. Bethkenhagen, B. B. L. Witte, M. Schörner, G. Röpke, T. Döppner, D. Kraus, S. H. Glenzer, P. A. Sterne, and R. Redmer, Carbon ionization at gigabar pressures: an ab initio perspective on astrophysical high-density plasmas, Phys. Rev. Res. **2**, 023260 (2020).

[123] J. Clérouin, A. Blanchet, C. Blancard, G. Faussurier, F. Soubiran, and M. Bethkenhagen, Equivalence between pressure- and structure-defined ionization in hot dense carbon, Phys. Rev. E **106**, 045204 (2022).

[124] Q. Ma, J. Dai, D. Kang, M. S. Murillo, Y. Hou, Z. Zhao, and J. Yuan, Extremely low electron-ion temperature relaxation rates in warm dense hydrogen: interplay between quantum electrons and coupled ions, Phys. Rev. Lett. **122**, 015001 (2019).

[125] D. Klakow, C. Toepffer, and P.-G. Reinhard, Semiclassical molecular dynamics for strongly coupled Coulomb systems, The Journal of Chemical Physics **101**, 10766–10774 (1994).

[126] A. Kononov, C.-W. Lee, T. P. dos Santos, B. Robinson, Y. Yao, Y. Yao, X. Andrade, A. D. Baczewski, E. Constantinescu, A. A. Correa, Y. Kanai, N. Modine, and A. Schleife, Electron dynamics in extended systems within real-time time-dependent density-functional theory, MRS Communications **12**, 1002–1014 (2022).

[127] B. Jakob, P.-G. Reinhard, C. Toepffer, and G. Zwicknagel, Wave packet simulation of dense hydrogen, Phys. Rev. E **76**, 036406 (2007).

[128] P. E. Grabowski, "A review of wave packet molecular dynamics", in Frontiers and challenges in warm dense matter, edited by F. Graziani, M. P. Desjarlais, R. Redmer, and S. B. Trickey (2014), pp. 265–282.

[129] J. T. Su and W. A. Goddard, Excited electron dynamics modeling of warm dense matter, Phys. Rev. Lett. **99**, 185003 (2007).

[130] W. A. Angermeier and T. G. White, An investigation into the approximations used in wave packet molecular dynamics for the study of warm dense matter, Plasma **4**, 294–308 (2021).

[131] J. Ono and K. Ando, Semiquantal molecular dynamics simulations of hydrogen-bond dynamics in liquid water using multi-dimensional gaussian wave packets, The Journal of Chemical Physics **137**, 174503 (2012).

[132] H. V. Henderson and S. R. Searle, On deriving the inverse of a sum of matrices, SIAM Review **23**, 53–60 (1981).

[133] R. Ditchfield, W. J. Hehre, and J. A. Pople, Self-consistent molecular orbital methods. vi. energy optimized gaussian atomic orbitals, The Journal of Chemical Physics **52**, 5001–5007 (1970).

[134] D. A. McQuarrie, *Quantum chemistry*, 2nd ed. (University Science, Sausalito, Calif, 2007).

[135] W. Ebeling, A. Filinov, M. Bonitz, V. Filinov, and T. Pohl, The method of effective potentials in the quantum-statistical theory of plasmas, Journal of Physics A: Mathematical and General **39**, 4309–4317 (2006).

[136] M. Knaup, P.-G. Reinhard, and C. Toepffer, Wave packet molecular dynamics simulations of hydrogen near the transition to a metallic fluid, Contributions to Plasma Physics **39**, 57–60 (1999).

[137] Y. Lavrinenko, P. R. Levashov, D. V. Minakov, I. V. Morozov, and I. A. Valuev, Equilibrium properties of warm dense deuterium calculated by the wave packet molecular dynamics and density functional theory method, Phys. Rev. E **104**, 045304 (2021).

[138] H. M. Bellenbaum, M. P. Böhme, M. Bonitz, T. Döppner, L. B. Fletcher, T. Gawne, D. Kraus, Z. A. Moldabekov, S. Schwalbe, J. Vorberger, and T. Dornheim, Estimating ionization states and continuum lowering from ab initio path integral monte carlo simulations for warm dense hydrogen, Phys. Rev. Res. **7**, 033016 (2025).

[139] M. Bonitz and L. Kordts, Ionization potential depression and fermi barrier in warm dense matter: a first-principles approach, Contributions to Plasma Physics **65**, e70001 (2025).

[140] T. Dornheim, T. Döppner, P. Tolias, M. P. Böhme, L. B. Fletcher, T. Gawne, F. R. Graziani, D. Kraus, M. J. MacDonald, Z. A. Moldabekov, S. Schwalbe, D. O. Gericke, and J. Vorberger, Unraveling electronic correlations in warm dense quantum plasmas, Nature Communications **16**, 5103 (2025).

[141] R. A. Davis, W. A. Angermeier, R. K. T. Hermsmeier, and T. G. White, Ion modes in dense ionized plasmas through nonadiabatic molecular dynamics, Phys. Rev. Res. **2**, 043139 (2020).

[142] H. Xiao, A. Jaramillo-Botero, P. L. Theofanis, and W. A. Goddard, Non-adiabatic dynamics modeling framework for materials in extreme conditions, Mechanics of Materials **90**, 243–252 (2015).

[143] T. Campbell, P. Svensson, B. Larder, D. Plummer, S. M. Vinko, and G. Gregori, Molecular dynamics framework coupled with smoothed particle hydrodynamics for quantum plasma simulations, Phys. Rev. Res. **7**, 023286 (2025).

[144] S. Nagel, R. Redmer, G. Röpke, M. Knaup, and C. Toepffer, Proton-proton pair distribution in dense fluid hydrogen, Phys. Rev. E **57**, 5572–5577 (1998).

[145] A. Ono and H. Horiuchi, Antisymmetrized molecular dynamics for heavy ion collisions, Progress in Particle and Nuclear Physics **53**, 501–581 (2004).

[146] I. V. Morozov and I. A. Valuev, Localization constraints in gaussian wave packet molecular dynamics of nonideal plasmas, Journal of Physics A: Mathematical and Theoretical **42**, 214044 (2009).

[147] Y. Yao, Q. Zeng, K. Chen, D. Kang, Y. Hou, Q. Ma, and J. Dai, Reduced ionic diffusion by the dynamic electron-ion collisions in warm dense hydrogen, Physics of Plasmas **28**, 012704 (2021).

[148] Y. S. Lavrinenko, I. Morozov, and I. A. Valuev, Reflecting boundary conditions for classical and quantum molecular dynamics simulations of nonideal plasmas, Contributions to Plasma Physics **56**, 448–458 (2016).

[149] Y. S. Lavrinenko, I. V. Morozov, and I. A. Valuev, Wave packet molecular dynamics–density functional theory method for non-ideal plasma and warm dense matter simulations, Contributions to Plasma Physics **59**, e201800179 (2019).

[150] Y. S. Lavrinenko, I. V. Morozov, and I. A. Valuev, High performance wave packet molecular dynamics with density functional exchange-correlation term for non-ideal plasma simulations, Journal of Physics: Conference Series **1787**, 012043 (2021).

[151] M. L. Mehta, *Random matrices*, 3rd ed. (Elsevier, Amsterdam, 2004).

[152] N. Metropolis, A. Rosenbluth, M. Rosenbluth, A. Teller, and E. Teller, Equation of state calculations by fast computing machines, J. Chem. Phys. **21**, 1087–1092 (1953).

[153] W. Hastings, Monte carlo sampling methods using markov chains and their applications, Biometrika **57**, 97–109 (1970).

[154] C. Robert and G. Casella, *Monte carlo statistical methods*, 2nd ed. (Springer, 2004).

[155] G. Chabrier, S. Mazevet, and F. Soubiran, A new equation of state for dense hydrogen–helium mixtures, The Astrophysical Journal **872**, 51 (2019).

[156] Y. Fu, Y. Hou, D. Kang, C. Gao, F. Jin, and J. Yuan, Multi-charge-state molecular dynamics and self-diffusion coefficient in the warm dense matter regime, Physics of Plasmas **25**, 012701 (2018).

[157] W. A. Angermeier, B. S. Scheiner, N. R. Shaffer, and T. G. White, Disentangling the effects of non-adiabatic interactions upon ion self-diffusion within warm dense hydrogen, Philosophical Transactions of the Royal Society A: Mathematical, Physical and Engineering Sciences **381**, 20230034 (2023).

[158] A. Ono and H. Horiuchi, Antisymmetrized molecular dynamics of wave packets with stochastic incorporation of the vlasov equation, Phys. Rev. C **53**, 2958–2972 (1996).

[159] T. Furuta and A. Ono, Nuclear liquid-gas phase transition studied with antisymmetrized molecular dynamics, Phys. Rev. C **74**, 014612 (2006).

[160] P. V. Parandekar and J. C. Tully, Mixed quantum-classical equilibrium, The Journal of Chemical Physics **122**, 094102 (2005).

[161] P. V. Parandekar and J. C. Tully, Detailed balance in ehrenfest mixed quantum-classical dynamics, Journal of Chemical Theory and Computation **2**, 229–235 (2006).

[162] J. C. Tully, Mixed quantum–classical dynamics, Faraday Discuss. **110**, 407–419 (1998).

[163] D. J. Coughtrie and D. P. Tew, The nosé–hoover looped chain thermostat for low temperature thawed gaussian wave-packet dynamics, The Journal of Chemical Physics **140**, 194106 (2014).

[164] D. J. Coughtrie and D. P. Tew, A gaussian wave packet phase-space representation of quantum canonical statistics, The Journal of Chemical Physics **143**, 044102 (2015).